Master's thesis

NTNU
Norwegian University of Science and Technology
Faculty of Engineering
Department of Geoscience and Petroleum

Kristoffer Aurstad Dolvik

Numerical modelling of crack initiation and propagation in rocks using the XFEM

Master's thesis in Geology
Supervisor: Alexandre Lavrov
May 2022

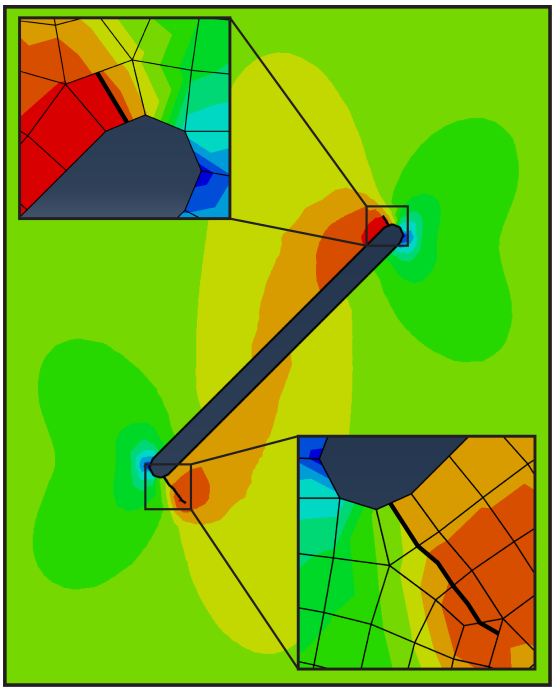

NTNU
Norwegian University of
Science and Technology

Kristoffer Aurstad Dolvik

Numerical modelling of crack initiation and propagation in rocks using the XFEM

Master's thesis in Geology
Supervisor: Alexandre Lavrov
May 2022

Norwegian University of Science and Technology
Faculty of Engineering
Department of Geoscience and Petroleum

NTNU

Kunnskap for en bedre verden

Abstract

This study focuses on the numerical simulation of crack growth in a rock-like material exposed to uniaxial compression using the extended finite element method (XFEM). Two-dimensional specimens that contain a single open pre-existing flaw with different inclination angles are used in the simulations, which are carried out using the Abaqus/CAE software. The simulations are based on two methods - the cohesive zone method (CZM) and linear elastic fracture mechanics (LEFM) - and their ability to simulate wing and anti-wing cracks are monitored and compared. The Maximum principal stress criterion (Maxps-criterion) that is available in Abaqus is used to govern the initiation of new cracks without the use of pre-defined cracks. In addition, results obtained from the simulations are compared to laboratory experiments done on similar specimens by Zhang et al. (2021). The simulations show that both the CZM and LEFM method can simulate initiation and propagation of wing and anti-wing cracks, and that the crack initiation stresses follow the same trends that are observed in experiments, i.e., the initiation stresses increase as the pre-existing flaw inclination angle increases. The wing crack initiation stresses in the simulations however, are much lower than the experimental results by Zhang et al. (2021), while the anti-wing crack initiation stresses in the simulations are more agreeable with the experimental results. The wing crack initiation angles also follow the same trend as the analytical solution and what is observed in experiments, i.e., the wing crack initiation angle decreases as the pre-existing flaw inclination angle increases. Further, relative displacements across the wing and anti-wing cracks indicate that they are dominantly Mode 1 fractures, in combination with some small shearing (the shearing decreases as the inclination angle increases). The stress analysis also indicates high stress concentrations along the long sides of the pre-existing flaw after initiation of the anti-wing cracks, suggesting that cracks may initiate in these areas, which is also observed in some experiments.

Sammendrag

Denne masteroppgaven fokuserer på numerisk modellering av sprekkevekst i et bergartslignende materiale under enaksielt trykk ved å bruke den utvidete endelige element metoden (XFEM). Todimensjonale prøvestykker som inneholder en eksisterende åpen sprekk/defekt med varierende helningsvinkel er brukt i simuleringene, som er utført med programmet Abaqus/CAE. Simuleringene er basert på to metoder – kohesiv sone-metoden (CZM) og lineær elastisk bruddmekanikk (LEFM) – og deres evne til å simulere vinge- og antivingesprekker blir sammenliknet. I Abaqus blir «største hovedspenning»-kriteriet (Maxps-kriteriet) brukt for å styre sprekkeinitiering av nye sprekker, uten å bruke allerede definerte sprekker i modellen. I tillegg blir resultater fra simuleringene sammenliknet med eksperiment som er utført av Zhang et al. (2021). Simuleringene viser at både CZM- og LEFM-metoden klarer å simulere sprekkeinitiering og sprekkevekst av både vinge- og antivingesprekker, og at initieringsspenningene til begge sprekketypene følger de samme trendene som er observert i eksperiment, altså at initieringsspenningen øker med økende helningsvinkel til den eksisterende sprekken. Initieringsspenningene til vingesprekkene i simuleringene er derimot mye lavere enn det som er observert i eksperimentene til Zhang et al. (2021), mens initieringsspenningene til antivingesprekkene i simuleringene stemmer bedre overens med resultatene fra eksperimentene. Initieringsvinkelene til vingesprekkene følger også samme trend som den analytiske løsningen og det som er observert i eksperiment, altså at initieringsvinkelen minker når helningsvinkelen til den allerede eksisterende sprekken øker. Videre indikerer forskyvningsmålinger over vinge- og antivingesprekkene at de er hovedsakelig Mode I brudd kombinert med små skjærbevegelser (skjærforskyvningen over vingesprekkene minker når helningsvinkelen til den åpne sprekken øker). Spenningsanalysen av modellene indikerer også at høye spenningskonsentrasjoner oppstår langs de lange sidene av den eksisterende sprekken etter initiering av antivingesprekkene, og dermed muligheten for nye sprekker å initiere i disse områdene, noe som er observert i noen eksperiment.

Acknowledgement

This master's thesis will finish 5 years of studying Geology and Engineering geology at the Norwegian University of Science and Technology (NTNU). The thesis was written during the autumn of 2021 and spring of 2022 under the Department of Geoscience and Petroleum.

After many practical courses regarding Engineering geology and Construction engineering, I wanted to challenge a more theoretical approach to rock mechanics. During a numerical analysis course lectured by my supervisor, Prof. Alexandre Lavrov, the subject of crack propagation appeared and caught my attention. Further, Prof. Alexandre Lavrov facilitated a special course for me, focusing on fracture mechanics, the finite element method (FEM) and the extended finite element method (XFEM). This laid the foundation of this thesis, and we developed a research objective focusing on the simulation of crack initiation and propagation using the XFEM. Thank you for your solid advice, guidance, and feedback throughout the entirety of the writing of this thesis, Alexandre.

I would also like to thank those who have supported me through this rock adventure, and the amazing classmates I've been lucky to get to know. Lastly, I am grateful for motivational contributions from Ivar C. J., Lasse M. W. and D. M. Carter Jr.

Trondheim, May 2022

Kristoffer Aurstad Dolvik

Contents

Figures

Tables

Nomenclature

Abbreviations

1D	One-dimensional
2D	Two-dimensional
3D	Three-dimensional
CZM	Cohesive zone method
D	Damage variable
ERR	Energy release rate
FE/FEM	Finite element/Finite element method
FPZ	Fracture process zone
LEFM	Linear elastic fracture mechanics
LSM	Level set method
Maxps	Maximum principal stress
MS	Maximum tensile stress
SIF	Stress intensity factor
XFEM	Extended finite element method

Symbols (Fracture mechanics)

$2a$	Crack/flaw length
α	Flaw inclination angle
dW	Incremental release of energy
dW_s	Incremental increase of surface energy
E	Young's modulus
G	Energy release rate
G_I	Mode I Energy release rate
G_{II}	Mode II Energy release rate
G_{III}	Mode III Energy release rate
G_C	Critical energy release rate
G_{IC}	Critical Mode I Energy release rate
G_{IIC}	Critical Mode II Energy release rate
K	Stress intensity factor
K_I	Mode I Stress intensity factor

K_{II}	Mode II Stress intensity factor
K_{III}	Mode III Stress intensity factor
K_{IC}	Critical Mode I Stress intensity factor
K_{IIC}	Critical Mode II Stress intensity factor
K_{IIIC}	Critical Mode III Stress intensity factor
k	Plane stress/strain factor
μ	Shear modulus
σ	Stress
σ_0	Remote stress
$\sigma_{\theta\theta max}$	Maximum circumferential stress
τ_0	Remote shear stress
θ_0	Crack initiation angle
ν	Poisson's ratio
W	Total energy released

Symbols (XFEM)

a	Heaviside function additional degree of freedom
$b1$-$b4$	Asymptotic crack tip function additional degrees of freedom
β	Angle associated with rotation of coordinate system
$\mathbf{b}$	Body force per unit volume
$\mathbf{C}$	Elastic matrix
∇_s	Symmetric part of the gradient operator
Ω	Domain
$\boldsymbol{\varepsilon}$	Strain vector
$\mathbf{f}$	Global vector of external force
$\mathbf{f}^e$	Elemental vector of external force
F_α	Asymptotic crack tip function (for α = 1,2,3,4)
H	Heaviside function
$\mathbf{K}$	Global stiffness matrix
$\mathbf{K}_{ij}^e$	Elemental stiffness matrix
$\mathbf{n}$	Unit normal vector
N_i	Bilinear shape function
$\boldsymbol{\sigma}$	Cauchy stress tensor
Γ	Boundary
Γ_c	Discontinuity/traction-free component of the boundary
Γ_u	Displacement components of the boundary
Γ_t	Traction component of the boundary
$\bar{\mathbf{t}}$	External traction vector
$\mathbf{u}$	Displacement vector
$\mathbf{u}^h$	Vector with degrees of freedom (XFEM)
$\mathbf{u}^{FE}$	Vector with only standard degrees of freedom (FEM)
$\mathbf{u}^{enriched}$	Vector with only enriched degrees of freedom
$\mathcal{U}$	The space of admissible displacement fields
$\mathcal{U}_0$	The test function space
$\mathcal{V}$	The space that allows for discontinuous functions across the crack line

1 Introduction

1.1 Background and research task

A rock mass consists of several joints that are distributed either sporadically or in systematical sets. These joints are commonly made by geological processes, and they contribute to make the rock mass discontinues, as opposed to an entirely intact rock specimen. In engineering geological operations, it is important to understand how such a discontinuous rock mass behaves, and how any changes in the stress field may affect the joints. In addition to geological processes, engineering operations like tunneling and mining may create new fractures, i.e., cracks, typically in the vicinity of tunnel or cavern openings and in pillars, see Figure 1. It is also in such engineering operations important to understand how these joints and cracks may develop and grow, and how the stability of the surrounding rock mass is affected.

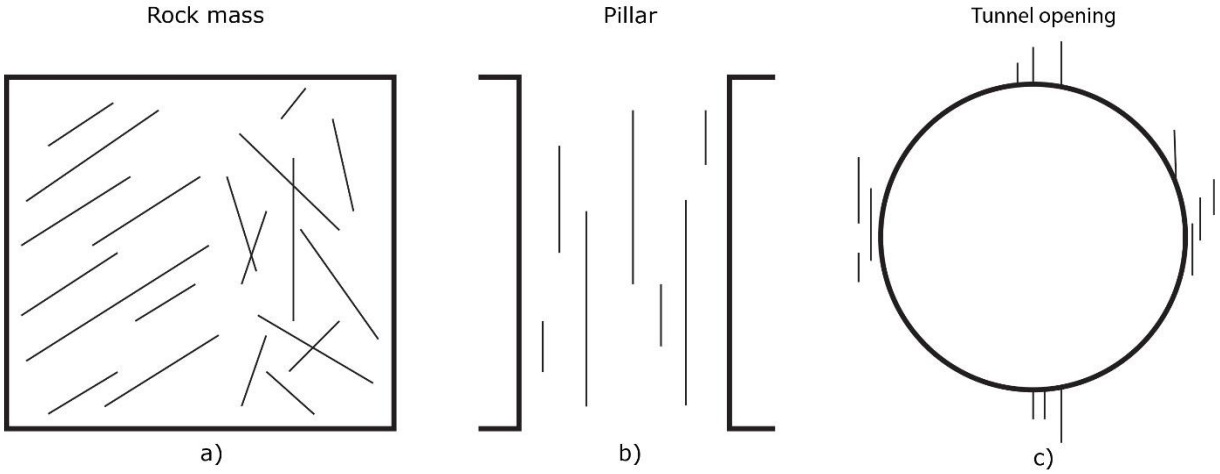

Figure 1 Typical occurrences of fractures: Joints in a rock mass (systematically and sporadically), axial cracks in pillars and cracks around tunnel openings.

The breaking of atomic bonds is generally what causes fracture in solid materials, and the applied stress needed to break these bonds is one way to quantify the theoretical strength of a solid. To describe the initiation and propagation mechanism of cracks in brittle materials such as rocks, the concept of fracture mechanics is often used (Sun and Jin, 2012b). A crack will according to linear elastic fracture mechanics (LEFM) initiate and propagate when the critical fracture toughness of a material is exceeded. The critical fracture toughness of a material is commonly exceeded in the vicinity of flaw tips in already existing flaws – like the ends of joints and cracks in rocks. This is due to stress concentrations around these flaw tips that quickly become magnitudes higher than the material strength (Sun and Jin, 2012b). It is important to note that minute pre-existing flaws, e.g., mineral grain boundaries and micropores, can initiate microcracks which eventually propagate and develop into macrocracks causing fracture at stress levels 10 to 100 times lower than the theoretical strength (Sun and Jin, 2012b). It is well known that fractures that are observed in intact rock often is the consequence of the coalescence of these microcracks (Kranz (1979), Eberhardt et al. (1999), Hoek and Martin (2014)). The understanding of fracture mechanics is therefore key to be able to describe the initiation,

propagation, and eventual coalescence of cracks, and thereby the stability and strength of rock.

Many experimental studies have been carried out on rock and rock like materials under uniaxial compression that contain single or multiple macro flaws (Bobet and Einstein (1998), Wong and Einstein (2009), Lee and Jeon (2011), Yang et al. (2013), Zhou et al. (2019), Zhang et al. (2021), Liu et al. (2021)). The cracks observed in these types of experiments were typically described as primary (tensile nature) and secondary (shear nature) cracks, and to initiate from the tips of the pre-existing flaws. Generally, the crack types may be classified into nine different categories based on experimental observations, see Figure 2. In this study, the type I and II cracks from Figure 2 will be replaced by the term "wing crack", while the type III crack will be replaced by the term "anti-wing crack". It is also observed from these experiments that cracks of tensile nature, like type I-V, propagate in the direction perpendicular to the local maximum principal stress.

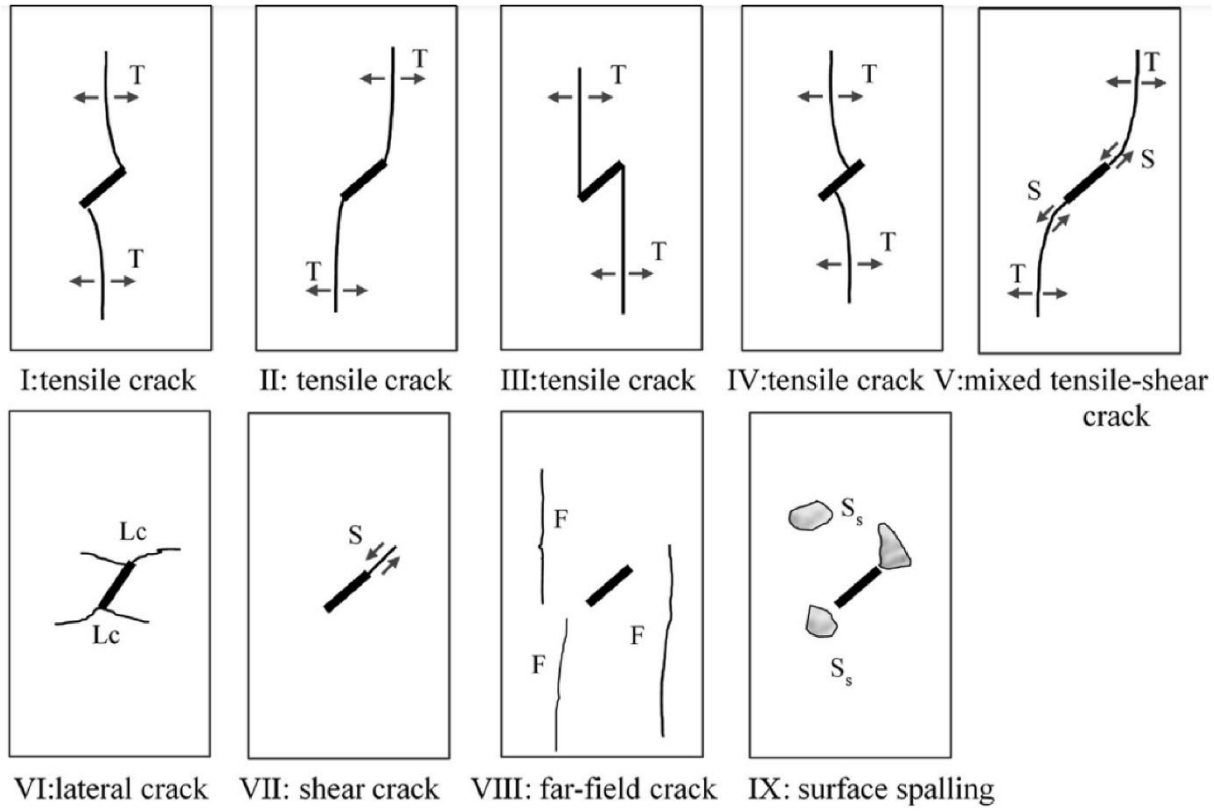

Figure 2 Different categories of cracks initiating from pre-existing flaws under compression. Type I and II are typical "wing cracks", while Type III is a typical "anti-wing crack". From Zhang et al. (2021).

In addition to experimental and analytical studies to understand the behaviors of cracks in different materials, numerical modelling has emerged as a powerful tool to analyze fracture problems. Different numerical models have been used to solve such problems, like the finite element method (FEM) (Reyes and Einstein (1991), Xu and Yuan (2011)), the discrete element method (DEM) (Lee and Jeon (2011), Sharafisafa and Nazem (2014)), the hybrid finite-discrete element method (FDEM) (Mahabadi et al. (2012), Lisjak et al. (2014)), the displacement discontinuity method (DDM) (Vásárhelyi and Bobet, 2000), the

numerical manifold method (NMM) (Wu and Wong, 2012) and the extended finite element method (XFEM) (Sharafisafa and Nazem (2014), Wang (2015), Wang et al. (2020), Xie et al. (2016), Haeri et al. (2020), Sivakumar and Maji (2021)). Especially the XFEM was found to be advantageous, as it opposed to the FEM can keep track of the crack path without the need of updating the finite element mesh, i.e., remeshing. In combination with a cohesive zone model (CZM), XFEM can be used to simulate cracks that follows fracture mechanics theory, as it introduces element degradation ahead of the crack tip which can replicate a small plastic zone, commonly referred to as a fracture process zone (FPZ) (Dugdale, 1960).

The CZM based XFEM is available in the finite element software Abaqus and seems to be frequently used by researchers within rock mechanics. However, Abaqus also offers LEFM based XFEM, which is not as widely used. The LEFM based XFEM does not consider element degradation ahead of the crack tip, but rather calculates the energy release rates at the vicinity of the crack tip, and thereby do not replicate the FPZ. In brittle materials such as rock, the FPZ may be assumed to be relatively small and therefore comply with LEFM (Sun and Jin, 2012c). The CZM based XFEM method has been successfully used to simulate wing crack growth, and to reasonably match wing crack initiation stresses for different pre-existing flaw inclination angles. However, the growth of anti-wing cracks seems to be less documented in the XFEM literature.

In this study both CZM and LEFM based XFEM in Abaqus will be used to simulate crack initiation and propagation in a linearly elastic specimen containing a single pre-existing open flaw. The simulations will use the "maximum principal stress"-criterion that is available in Abaqus, which allows cracks to initiate solely based on a stress criterion, and therefore do not require pre-defined cracks. Further, the differences between the two methods will be presented, as well as compared to experiments done on similar specimens. The initiation and propagation of anti-wing cracks are also interesting to analyze, as they frequently appear in experiments, and are important cracks in the later stages of a uniaxial compression test of these types of specimens. The validation of the LEFM based XFEM is also considered to be important for further development of fracture simulations, especially for the use in rock mechanics.

1.2 Report structure

The next parts of this thesis are organized as follows:

- **Chapter 2** presents an introduction to the general theory this thesis is based on, i.e., fracture mechanics, XFEM and how XFEM is used in Abaqus/CAE.
- **Chapter 3** describes the model set-up and the material properties implemented in the numerical models.
- **Chapter 4** presents the results of the numerical simulations and some comparisons to experimental results.
- **Chapter 5** discusses the results.
- **Chapter 6** gives a conclusion of the main findings and results.
- **Chapter 7** suggests further work.

2 Theory

2.1 Fracture mechanics

Generally, fractures may be defined by the breaking of interatomic bonds, and could therefore be theoretically calculated based on the strength of these bonds. However, the fracture values observed in the laboratory and the field show that fracture occur at much lower stresses than the theoretical strength. This was explained by Griffith (1920) to be because of several minute flaws in solids caused stress concentrations that exceeded the theoretical strength, even though the applied stress was low. These minute flaws were typically due to defects in materials, as well as grain boundaries in metals and rock-like materials. The work done by Griffith (1920) was motivated by Inglis (1913) who had studied the stresses around an elliptical hole in an infinitely large plate. Inglis (1913) discovered that when the short axis of an ellipse got close to zero, the stress would go to infinite at the ends of the long axis. Griffith (1920) therefore took an energy-based approach to study the stresses under such conditions. Further, Irwin (1948) and (1957) and Orowan (1948) developed Griffith's energy approach to account for plastic deformations, and Irwin also introduced three fracture modes, as well as the stress intensity factors. In the following, a theoretical basis to fracture mechanics will be given, and for more information about the subject, the reader is referred to Sun and Jin (2012a)-(2012e).

2.1.1 Stresses around an elliptical hole

By looking at an elliptical hole in an infinite large plate, Inglis (1913) was able to describe the stress distribution around an ellipse. Inglis found that the maximum stress occurs at the ends of the major axis for a case such as the one in Figure 3. His work gave the first quantitative evidence of local stress concentrations. The equation describing the stress at the end of the major axis in Figure 3 is as follows

$$\sigma_{yy} = \sigma_0 \left(1 + \frac{2a}{b}\right) \tag{1}$$

were σ_0 is the remote stress applied, and a and b are the lengths describing the ellipse. For a circular hole $(a = b)$, the stress concentration at the ends becomes $3\sigma_0$, while in the case of $b \rightarrow 0$ the stress concentration would increase towards infinite. This problem of a so called "line crack" would give the unreasonable result that any applied load would make this type of "crack" grow if a stress-based failure criterion was used. To overcome this problem of unstable crack growth, Griffith (1920) took an energy-based approach to describe the fracture mechanism.

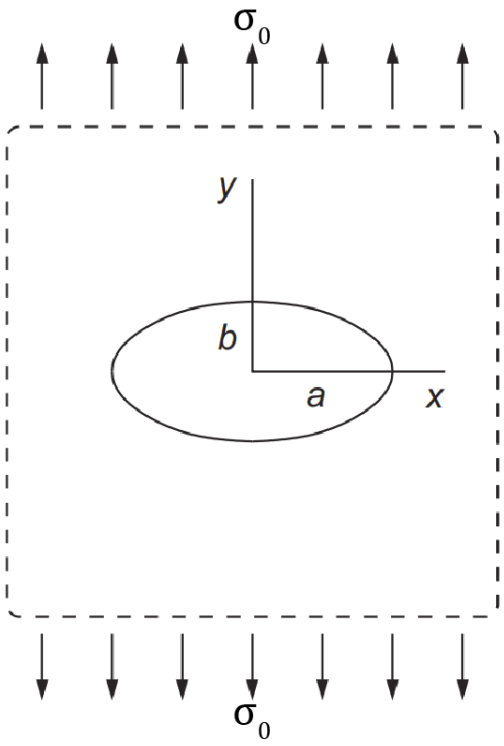

Figure 3 Elliptical hole in a plate under tension. Modified from Sun and Jin (2012b).

2.1.2 Griffith's theory of fracture

The energy-based approach taken by Griffith (1920) took a starting point in energy balance, and he used the solution of Inglis (1913) to calculate the potential energies in a body before and after crack extension. This made Griffith reason that an unstable crack propagation in a system, must lead to a decrease in the strain energy of the system (Sun and Jin, 2012b). In other words, for a crack to propagate, the incremental energy released, dW, due to a crack extension, da, must be greater than or equal to the incremental increase in surface energy, dW_s. The increase in surface energy occurs due to the newly developed crack surfaces. The critical point leading to crack propagation may therefore be written as follows

$$dW \geq dW_s \tag{2}$$

The surface energy for a crack containing two crack tips and having the length $2a$, is

$$W_s = 2(2a\gamma_s) = 4a\gamma_s \tag{3}$$

where γ_s is the surface energy density, and two surfaces per crack has been accounted for.

Further, Griffith (1921) used Inglis (1913) solution to obtain the total energy released, W, and expressed it as follows

$$W = \frac{\pi a^2 \sigma^2 (1 - \nu^2)}{E} \qquad for\ plane\ strain \tag{4}$$

and

$$W = \frac{\pi a^2 \sigma^2}{E} \qquad for\ plane\ stress \tag{5}$$

By substituting Eqs. 2 and 3 into Eq. 4 or 5, the critical stress, σ_{cr}, under which a crack will propagate is obtained:

$$\sigma_{cr} = \sqrt{\frac{2E\gamma_s}{\pi(1 - \nu^2)a}} \qquad for\ plane\ strain \tag{6}$$

and

$$\sigma_{cr} = \sqrt{\frac{2E\gamma_s}{\pi a}} \qquad for\ plane\ stress \tag{7}$$

These critical stress values are much smaller compared to theoretical critical stress values that are based solemnly on the breaking of atomic bonds. Therefore, explaining qualitatively how minute flaws leading to local stress concentrations reduce the strength of materials. Further, the energy released dW for a crack extension da can be expressed in the terms of the "strain energy release rate per crack tip", G:

$$dW = 2Gda \tag{8}$$

Thus,

$$G = \frac{dW}{2da} = \frac{\pi a \sigma^2 (1 - \nu^2)}{E} \qquad for\ plane\ strain \tag{9}$$

and

$$G = \frac{dW}{2da} = \frac{\pi a \sigma^2}{E} \qquad for\ plane\ stress \tag{10}$$

The critical value of G leading to crack propagation then becomes

$$G \geq 2\gamma_s \tag{11}$$

When G in Eq. 11 equals $2\gamma_s$ it is denoted G_C and is called the "fracture toughness". This is the Griffith criterion of fracture, and it holds for brittle fracture – and in this case for a line crack under tension. Since most materials are not perfectly brittle, the G_C value measured in experiments is often greater than $2\gamma_s$ due to plastic deformation close to the crack tip. Irwin (1948) and Orowan (1948) modified this criterion to account for plastic deformation. However, they also reasoned that Eqs. 9 and 10 would give reasonable results when the plastic zone that occurs around the crack tip is relatively small compared to the crack length and thickness of the specimen.

2.1.3 Fracture modes and stress intensity factor

To approximate the near crack-tip stress field, Irwin (1957) developed the stress intensity factor (SIF). The stress intensity factor, K, describes the intensity of the stress field at the vicinity of a crack tip, and is based on the exact solution presented by Westergaard (1939). Irwin (1957) pointed out three modes of fracture, namely *Opening mode* (Mode I), *Sliding mode* (Mode II) *and Tearing mode* (Mode III), see Figure 4. Each of these modes has an associated SIF, i.e., K_I, K_{II} and K_{III}. As for the critical energy release rate, G_C, a crack will initiate when its respective SIF reaches a critical value, K_{IC}, K_{IIC} or K_{IIIC}, also called the fracture toughness of the material.

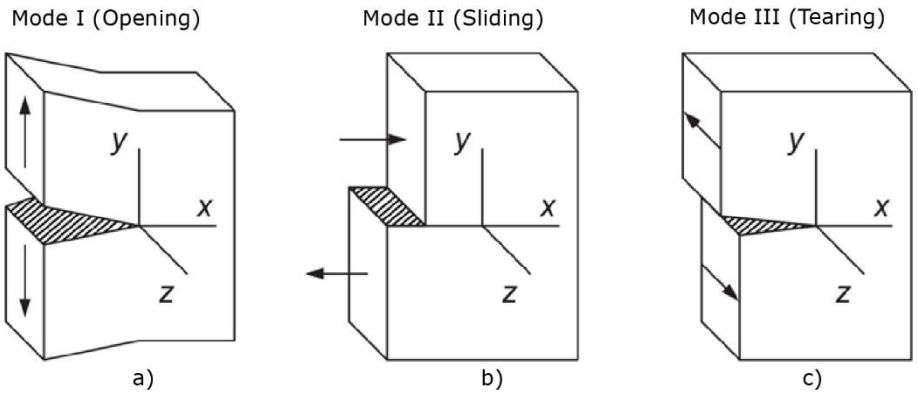

Figure 4 Different modes of fracture. The arrows indicate the displacement direction. ***a)*** *Mode I (Opening).* ***b)*** *Mode II (Sliding).* ***c)*** *Mode III (Tearing). From Sun and Jin (2012c).*

For a cracked body such as the one in Figure 4a), undergoing Mode I deformations, the stress field near the cack tip may be written in the terms of the Mode I stress intensity factor, K_I, as follows

$$\sigma_{xx} = \frac{K_I}{\sqrt{2\pi r}} cos\frac{1}{2}\theta\left(1 - sin\frac{1}{2}\theta sin\frac{3}{2}\theta\right) \tag{12}$$

$$\sigma_{yy} = \frac{K_I}{\sqrt{2\pi r}} cos\frac{1}{2}\theta\left(1 + sin\frac{1}{2}\theta sin\frac{3}{2}\theta\right) \tag{13}$$

$$\sigma_{xy} = \frac{K_I}{\sqrt{2\pi r}} sin\frac{1}{2}\theta\left(1 + sin\frac{1}{2}\theta sin\frac{3}{2}\theta\right) \tag{14}$$

where r is the radial distance from the crack tip, θ is the angle of the r-vector to the initial crack direction, see Figure 5, and K_I is defined as

$$K_I = \sigma_0\sqrt{\pi a} \tag{15}$$

where σ_0 is the remote stress applied in the y-direction, and a is the half length of the crack.

In the same manner, for a crack as the one in Figure 4b), the stress field near the crack tip may be written in the terms of the Mode II stress intensity factor, K_{II}, as follows

$$\sigma_{xx} = -\frac{K_{II}}{\sqrt{2\pi r}} sin\frac{1}{2}\theta(2 + cos\frac{1}{2}\theta cos\frac{3}{2}\theta) \tag{16}$$

$$\sigma_{yy} = \frac{K_{II}}{\sqrt{2\pi r}} sin\frac{1}{2}\theta cos\frac{1}{2}\theta cos\frac{3}{2}\theta \tag{17}$$

$$\sigma_{xy} = \frac{K_{II}}{\sqrt{2\pi r}} cos\frac{1}{2}\theta\left(1 - sin\frac{1}{2}\theta sin\frac{3}{2}\theta\right) \tag{18}$$

where K_{II} is defined as

$$K_{II} = \tau_0\sqrt{\pi a} \tag{19}$$

and τ_0 is the remote shear stress applied in the *x*-direction.

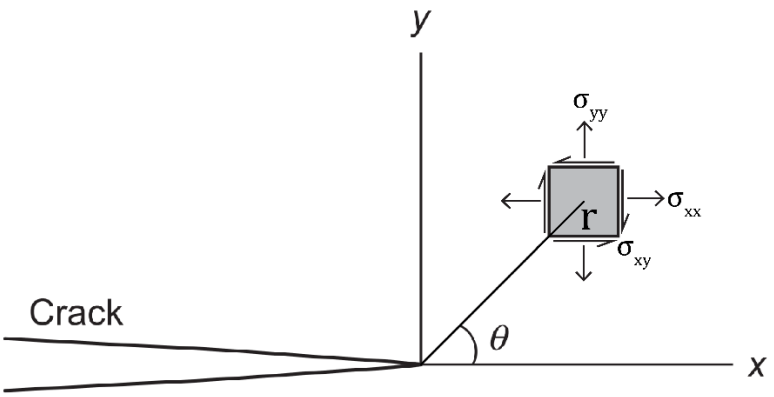

Figure 5 Elastic stress field around a crack tip. Modified from Sun and Jin (2012c).

Irwin (1957) found that the relationship between the energy release rate, G, and the stress intensity factor, K, could be expressed as follows

$$G_I = K_I^2 \frac{(1-\nu^2)}{E} \qquad For\ plane\ strain \tag{20}$$

$$G_I = \frac{K_I^2}{E} \qquad For\ plane\ stress \tag{21}$$

$$G_{II} = K_{II}^2 \frac{(k+1)}{8\mu} \tag{22}$$

where k = 3-4ν for plane strain, k = (3- ν)/(1+ ν) for plane stress and μ is the shear modulus.

Further, under Mode I conditions, it is well known that the crack propagation direction follows the original direction of the crack, while under Mode II conditions the propagation direction often deflects from the original direction of the crack (Sun and Jin, 2012e).

2.1.4 Open flaw under compression

When assessing specimens containing pre-existing and well-defined cracks, typically artificially cracks made in a laboratory, these cracks will in the following sections be termed flaws. An open flaw under uniaxial compression is like a flaw under tension, since the upper and lower surfaces of the flaw have no forces working on them – the boundary conditions of the flaws are the same (Lin et al., 2019). It may therefore be assumed that the stress field near the crack tip of an open flaw under compression is the same as the near crack

tip stress field of a flaw under tension. To express the near crack tip stress field of an open flaw under uniaxial compression, like the one in Figure 6a) (where both Mode I and Mode II deformations occur), Eqs. 12-14 and 16-18 may be combined as follows (Sun and Jin, 2012e, Lin et al., 2019)

$$\sigma_{xx} = \frac{K_I}{\sqrt{2\pi r}} cos\frac{1}{2}\theta\left(1 - sin\frac{1}{2}\theta sin\frac{3}{2}\theta\right) - \frac{K_{II}}{\sqrt{2\pi r}} sin\frac{1}{2}\theta\left(2 + cos\frac{1}{2}\theta cos\frac{3}{2}\theta\right) \tag{23}$$

$$\sigma_{yy} = \frac{K_I}{\sqrt{2\pi r}} cos\frac{1}{2}\theta\left(1 + sin\frac{1}{2}\theta sin\frac{3}{2}\theta\right) + \frac{K_{II}}{\sqrt{2\pi r}} sin\frac{1}{2}\theta cos\frac{1}{2}\theta cos\frac{3}{2}\theta \tag{24}$$

$$\sigma_{xy} = \frac{K_I}{\sqrt{2\pi r}} sin\frac{1}{2}\theta cos\frac{1}{2}\theta cos\frac{3}{2}\theta + \frac{K_{II}}{\sqrt{2\pi r}} cos\frac{1}{2}\theta\left(1 - sin\frac{1}{2}\theta sin\frac{3}{2}\theta\right) \tag{25}$$

where K_I and K_{II} are defined as

$$K_I = \frac{\sigma}{2}(1 + cos2\alpha)\sqrt{\pi a} \tag{26}$$

$$K_{II} = \frac{\sigma}{2} sin2\alpha\sqrt{\pi a} \tag{27}$$

and α is the inclination angle of the flaw with respect to the normal of the uniaxial stress direction, see Figure 6a).

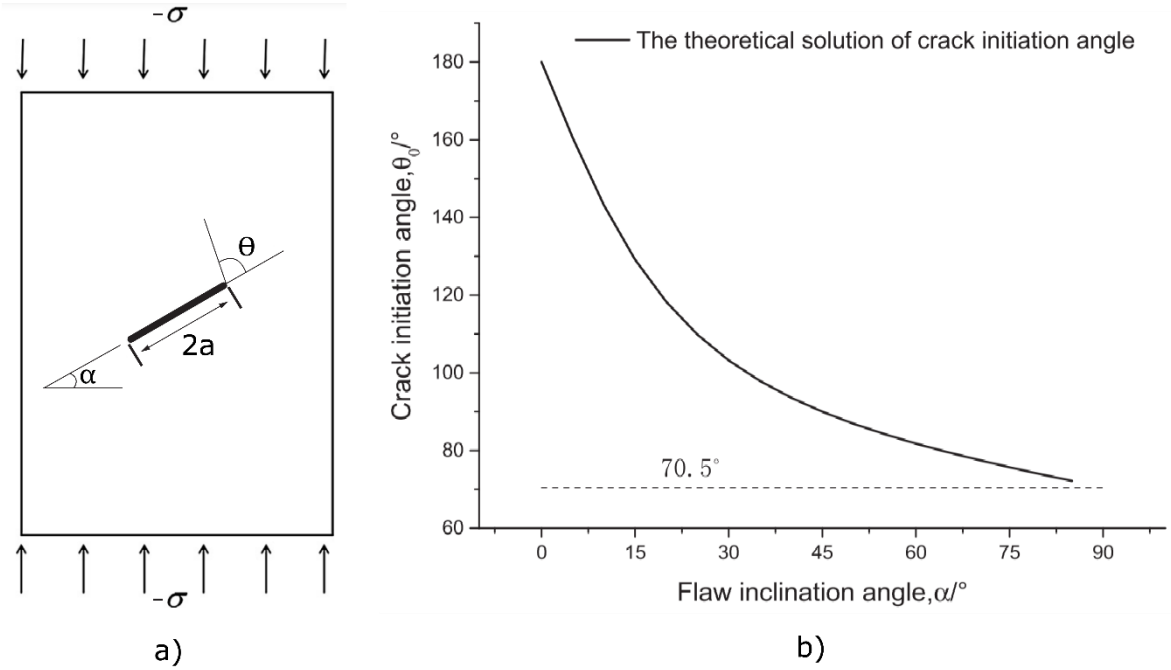

Figure 6 ***a)*** *Specimen containing a pre-existing open flaw under uniaxial compression.* ***b)*** *Theoretical crack initiation angle for different pre-existing open flaw inclination angles. Modified from Lin et al. (2019).*

To cope with cracks subjected to both Mode I and Mode II deformations, i.e., mixed mode fractures, Erdogan and Sih (1963) proposed a criterion based on the maximum tensile stress at the vicinity of the crack tip (MS-criterion). This criterion assumes that (1) the crack propagates in the direction perpendicular to the maximum circumferential stress, $\sigma_{\theta\theta max}$, and (2) the fracture happens when $\sigma_{\theta\theta}$ reaches the stress value that leads to Mode I fracture (Sun and Jin, 2012e). The near crack tip stress field can be expressed in the polar coordinates (r, θ), see Figure 7, and the stresses are as follows

$$\sigma_{rr} = \frac{K_I}{\sqrt{2\pi r}}\left(\frac{5}{4}cos\frac{1}{2}\theta - \frac{1}{4}\theta cos\frac{3}{2}\theta\right) + \frac{K_{II}}{\sqrt{2\pi r}}\left(-\frac{5}{4}sin\frac{1}{2}\theta + \frac{3}{4}sin\frac{3}{2}\theta\right) \tag{28}$$

$$\sigma_{\theta\theta} = \frac{1}{\sqrt{2\pi r}}cos\frac{1}{2}\theta\left(K_I cos^2\frac{1}{2}\theta - \frac{3}{2}K_{II}sin\theta\right) \tag{29}$$

$$\sigma_{r\theta} = \frac{1}{\sqrt{2\pi r}}cos\frac{1}{2}\theta\left(\frac{1}{2}K_I sin\theta + \frac{1}{2}K_{II}(3cos\theta - 1)\right) \tag{30}$$

where K_I and K_{II} are defined as in Eqs. 26 and 27, respectively.

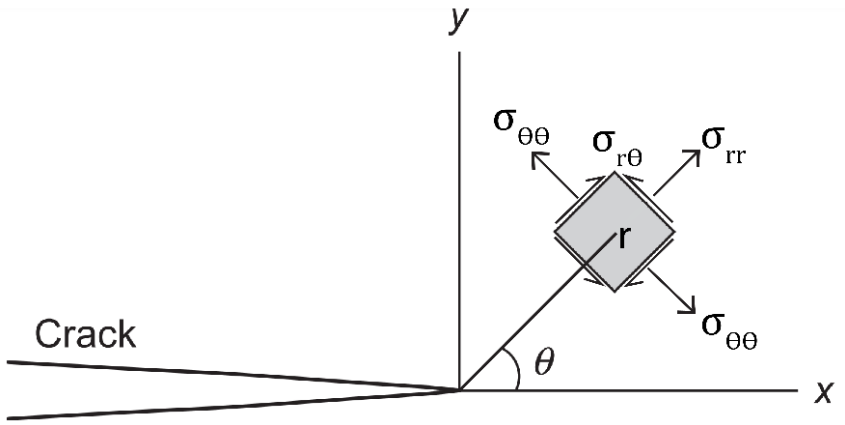

Figure 7 Elastic stress field around a crack tip (polar coordinates). Modified from Sun and Jin (2012e).

Further, Erdogan and Sih (1963) used their findings to express the theoretical crack propagation direction according to their MS-criterion. For an inclined pre-existing flaw under uniaxial compression, the propagation direction, i.e., the crack initiation angle, θ_0, can be expressed in terms of the inclination angle, α, as follows (Lin et al., 2019)

$$\theta_0 = 2arctan\frac{1+\sqrt{1+8\left(\frac{sin2\alpha}{1+cos2\alpha}\right)^2}}{4\left(\frac{sin2\alpha}{1+cos2\alpha}\right)} \tag{31}$$

In Eq. 31, σ has already been replaced by -σ to account for compressional stress. The graph of the crack initiation angle, θ_0, with respect to the flaw inclination angle, α, is shown in Figure 6b).

2.2 Introduction to XFEM

The XFEM approach is based on the traditional FEM and was first introduced by Belytschko and Black (1999). Their method made it possible to describe arbitrary cracks in a way that was almost independent of the mesh, by using a discontinuous enrichment function. Later, Moës et al. (1999) improved the method to be completely independent of the mesh, and only now the method got the name "XFEM". Moës et al. (1999) implemented a discontinuous jump function as well as a near crack tip asymptotic function through a partition of unity, which allows local enrichment functions to be easily incorporated into the FE approximation (Melenk and Babuška, 1996). These local enrichment functions allow for the calculation of additional degrees of freedom, which in the case of fracture mechanics is the discontinuous jump in displacement across a crack, and the near-tip asymptotic stress field around the crack tip. The enrichment functions give XFEM advantages compared to the traditional FEM in modelling crack initiation and propagation, because it allows for crack geometries that are not aligned with element edges, as well as that no remeshing is necessary (Moës et al., 1999).

Since the enrichments are introduced at a local level, only nodes directly affected by a discontinuity are enriched, saving computational cost/time. Figure 8 shows how a domain, Ω, containing a discontinuity, Γ_c, may be represented by two different approaches. In Figure 8b, the FE mesh is adapted to the crack, while Figure 8c displays the XFEM approach consisting of a mesh with locally enriched nodes around Γ_c (circles in the figure).

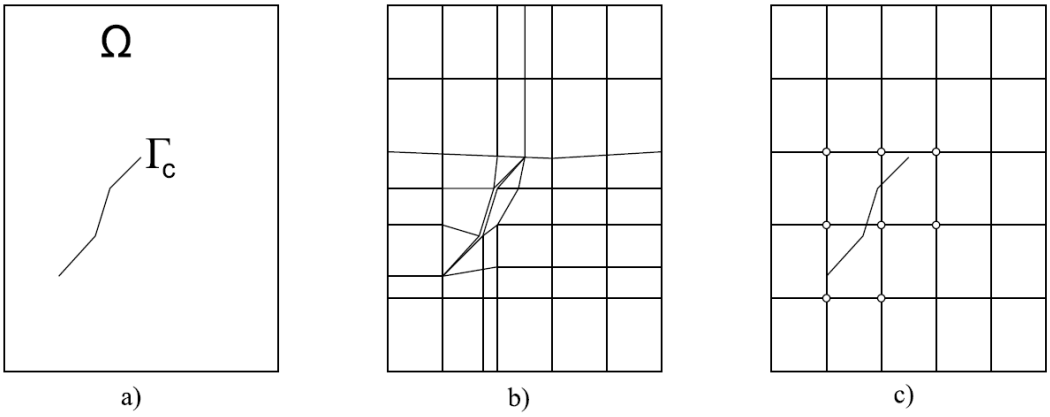

Figure 8 ***a)*** *A domain Ω containing a discontinuity Γ_c.* ***b)*** *The same domain and discontinuity in an adapted mesh.* ***c)*** *The same domain and discontinuity in an independent mesh. From Gjernes and Klokk (2012).*

In a simple manner, the XFEM approximation function for displacement, $\mathbf{u}^h$, can be written as follows

$$\mathbf{u}^h = \mathbf{u}^{FE} + \mathbf{u}^{enriched} \tag{32}$$

which contains contributions from both the traditional FE approximation, $\mathbf{u}^{FE}$, and the newly introduced enrichment functions that describe the additional degrees of freedom, $\mathbf{u}^{enriched}$, at the affected nodes.

The following sections explaining the general theory behind XFEM is based on Belytschko et al. (1994), Belytschko and Black (1999), Moës et al. (1999) and Sharafisafa and Nazem (2014).

2.2.1 Governing equations

The equilibrium equations and boundary conditions may be defined by considering a domain, Ω, which is bounded by Γ. The boundary Γ is divided into the three sets Γ_u, Γ_t and Γ_c which consists of displacement, traction, and traction-free components, respectively, see Figure 9. The boundary may be expressed such that $\Gamma = \Gamma_u \cup \Gamma_t \cup \Gamma_c$, and Γ_c may further be divided into Γ_{c^+} and Γ_{c^-} to represent each side of the crack surface/line (3D or 2D). The strong form of the equilibrium equation and the boundary conditions are

$$\boldsymbol{\nabla}\cdot\boldsymbol{\sigma} + \mathbf{b} = 0 \quad \text{in } \Omega \tag{33a}$$

$$\boldsymbol{\sigma}\cdot\mathbf{n} = \bar{\mathbf{t}} \quad \text{on } \Gamma_t \tag{33b}$$

$$\boldsymbol{\sigma}\cdot\mathbf{n} = 0 \quad \text{on } \Gamma_{c^+} \tag{33c}$$

$$\boldsymbol{\sigma}\cdot\mathbf{n} = 0 \quad \text{on } \Gamma_{c^-} \tag{33d}$$

where $\boldsymbol{\sigma}$ is the Cauchy stress tensor, $\mathbf{b}$ is the body force per unit volume, $\bar{\mathbf{t}}$ is the external traction vector and $\mathbf{n}$ is the unit normal vector.

When small displacements are considered the relationship between the strains, $\boldsymbol{\varepsilon}$, and the displacements, $\mathbf{u}$, may be expressed as follows

$$\boldsymbol{\varepsilon} = \boldsymbol{\varepsilon}(\mathbf{u}) = \boldsymbol{\nabla}_s\mathbf{u} \tag{34}$$

Where $\boldsymbol{\nabla}_s$ is the symmetric part of the gradient operator and also the boundary conditions below hold:

$$\mathbf{u} = \bar{\mathbf{u}} \quad \text{on } \Gamma_u \tag{35}$$

Further, for an elastic material the constitutive relation is given by Hooke's law:

$$\boldsymbol{\sigma} = \mathbf{C}:\boldsymbol{\varepsilon} \tag{36}$$

where $\mathbf{C}$ is the elastic matrix containing material properties like Young's modulus, Poisson's ratio and the shear modulus.

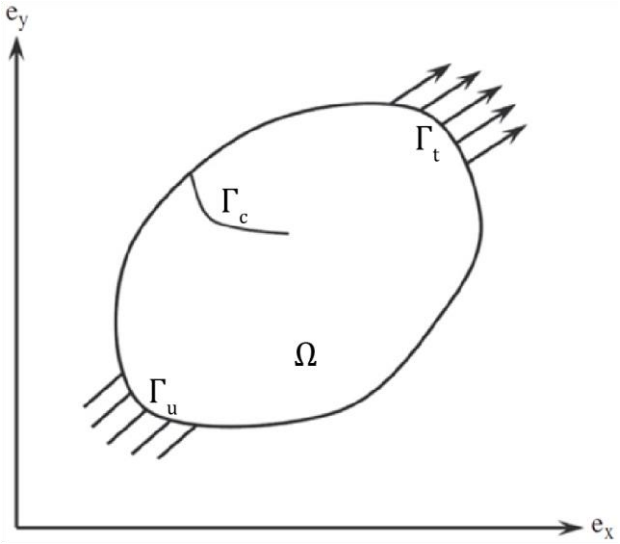

Figure 9 A domain Ω and its boundary $\Gamma = \Gamma_u \cup \Gamma_t \cup \Gamma_c$. From Sharafisafa and Nazem (2014).

2.2.2 Weak formulation

As for the traditional FE method the weak form of the differential equations is essential to solve the problem at hand. It has been shown by Belytschko and Black (1999) that the weak form of the equilibrium equation is equivalent to the strong form of the problem. It includes the traction free conditions on the two crack faces, and as for the traditional weak form from the FE formulation it can easily be extended to non-linear problems.

The strong form of the equilibrium equation (Eq. 33a) can be written on the following weak form:

$$\int_\Omega \boldsymbol{\sigma}:\boldsymbol{\varepsilon}(\mathbf{v})d\Omega = \int_\Omega \mathbf{b}\cdot\mathbf{v}d\Omega + \int_{\Gamma_t} \bar{\mathbf{t}}\cdot\mathbf{v}d\Gamma \quad \forall\mathbf{v} \in \mathcal{U}_0 \tag{37}$$

where

$$\mathcal{U} = \{\mathbf{v} \in \mathcal{V} : \mathbf{v} = \bar{\mathbf{u}} \text{ on } \Gamma_u \ \mathbf{v} \text{ discontinuous on } \Gamma_c\} \tag{38}$$

and

$$\mathcal{U}_0 = \{\mathbf{v} \in \mathcal{V} : \mathbf{v} = 0 \text{ on } \Gamma_u \ \mathbf{v} \text{ discontinuous on } \Gamma_c\} \tag{39}$$

In the above equations $\mathcal{U}$ is the space of admissible displacement fields, $\mathcal{U}_0$ is the test function space and the space $\mathcal{V}$ is related to the regularity of the solution and allows for discontinuous functions across the crack line (Moës et al., 1999).

By using the constitutive relation from Eq. 36 in the weak form in Eq. 37, the problem boils down to finding $\mathbf{u} \in \mathcal{U}$ such that (Moës et al., 1999)

$$\int_{\Omega} \boldsymbol{\varepsilon}(\mathbf{u}):\mathbf{C}:\boldsymbol{\varepsilon}(\mathbf{v})d\Omega = \int_{\Omega} \mathbf{b}\cdot\mathbf{v}d\Omega + \int_{\Gamma_t} \bar{\mathbf{t}}\cdot\mathbf{v}d\Gamma \quad \forall\mathbf{v} \in \mathcal{U}_0 \tag{40}$$

The weak form above can further be expressed as a discrete system of equilibrium equations like in the traditional FE formulation:

$$\mathbf{K}\mathbf{u}^{\mathrm{h}}=\mathbf{f} \tag{41}$$

where $\mathbf{u}^{\mathrm{h}}$ represents both the standard degrees of freedom ($\mathbf{u}^{\mathrm{FE}}$) and the new degrees of freedom associated with a discontinuity ($\mathbf{u}^{\mathrm{Enriched}}$), later referred to as enriched degrees of freedom. For a strong discontinuity such as a crack, two enrichment functions are used to describe the crack. These are a discontinuous jump function, usually the Heaviside function, H, and the asymptotic crack tip function, F. It is important to note that H is associated with only one additional degree of freedom (*a*), while *F* consists of four different functions and is therefore also associated with four additional degrees of freedom (*b1*, *b2*, *b3* and *b4*). It is also important to note that any enrichment functions may be used, depending on the problem and what degrees of freedom that are involved. In the following theory H and F are used to easier connect the XFEM theory to fracture analysis. Both functions are described in more detail in section 2.2.3. $\mathbf{u}^{\mathrm{h}}$ is defined as follows

$$\mathbf{u}^{\mathrm{h}}=\{\mathbf{u} \quad a \quad b1 \quad b2 \quad b3 \quad b4\}^{\mathrm{T}} \tag{42}$$

Furthermore, **K** is the global stiffness matrix and **f** is the global vector of external force. As for traditional FEM, both **K** and **f** are computed at element level and later assembled into their global counterparts. The superscript "e" will in the following refer to elemental counterparts. The elemental contributions from **K** and **f** are as follows

$$\mathbf{K}_{ij}^{\mathrm{e}} = \begin{bmatrix} \mathbf{K}_{ij}^{uu} & \mathbf{K}_{ij}^{ua} & \mathbf{K}_{ij}^{ub} \\ \mathbf{K}_{ij}^{au} & \mathbf{K}_{ij}^{aa} & \mathbf{K}_{ij}^{ab} \\ \mathbf{K}_{ij}^{bu} & \mathbf{K}_{ij}^{ba} & \mathbf{K}_{ij}^{bb} \end{bmatrix} \tag{43}$$

$$\mathbf{f}^{\mathrm{e}} = \left\{\mathbf{f}_i^{u} \quad \mathbf{f}_i^{a} \quad \mathbf{f}_i^{b1} \quad \mathbf{f}_i^{b2} \quad \mathbf{f}_i^{b3} \quad \mathbf{f}_i^{b4}\right\}^{\mathrm{T}} \tag{44}$$

where $\mathbf{K}_{ij}^{uu}$ represent the standard degrees of freedom, $\mathbf{K}_{ij}^{ua}$, $\mathbf{K}_{ij}^{ub}$, $\mathbf{K}_{ij}^{au}$, $\mathbf{K}_{ij}^{bu}$ represent the overlapping between standard and enriched degrees of freedom, while $\mathbf{K}_{ij}^{aa}$, $\mathbf{K}_{ij}^{ab}$, $\mathbf{K}_{ij}^{ba}$ and $\mathbf{K}_{ij}^{bb}$ represent only the enriched degrees of freedom. The sub-matrices from Eqs. 43 and 44 are defined as follows

$$\mathbf{K}_{ij}^{rq}=\int_{\Omega^e}(\mathbf{B}_i^r)^{\mathrm{T}}\,\mathbf{C}\mathbf{B}_j^q\,d\Omega \qquad (r,\,q=u,a,b) \tag{45}$$

$$\mathbf{f}_i^u=\int_{\Gamma_t}N_i\bar{\mathbf{t}}\,d\Gamma+\int_{\Omega^e}N_i\mathbf{b}\,d\Omega \tag{46}$$

$$\mathbf{f}_i^a=\int_{\Gamma_t}N_i(H(\mathbf{x})-H(\mathbf{x}_i))\bar{\mathbf{t}}\,d\Gamma+\int_{\Omega^e}N_i(H(\mathbf{x})-H(\mathbf{x}_i))\mathbf{b}\,d\Omega \tag{47}$$

$$\mathbf{f}_i^{b\alpha}=\int_{\Gamma_t}N_i(F_\alpha(\mathbf{x})-F_\alpha(\mathbf{x}_i))\bar{\mathbf{t}}\,d\Gamma+\int_{\Omega^e}N_i\big(F_\alpha(\mathbf{x})-F_\alpha(\mathbf{x}_i)\big)\mathbf{b}\,d\Omega \qquad \text{where } \alpha=1,2,3,4 \tag{48}$$

where **C** is the elastic matrix, N_i is the finite element shape function at node i, and the **B**-matrices are defined as follows in two dimensions

$$\mathbf{B}_i^u=\begin{bmatrix}N_{i,x} & 0\\ 0 & N_{i,y}\\ N_{i,y} & N_{i,x}\end{bmatrix} \tag{49}$$

$$\mathbf{B}_i^a=\begin{bmatrix}(N_i(H(\boldsymbol{x})-H(\boldsymbol{x}_i)))_{,x} & 0\\ 0 & (N_i(H(\boldsymbol{x})-H(\boldsymbol{x}_i)))_{,y}\\ (N_i(H(\boldsymbol{x})-H(\boldsymbol{x}_i)))_{,y} & (N_i(H(\boldsymbol{x})-H(\boldsymbol{x}_i)))_{,x}\end{bmatrix} \tag{50}$$

$$\mathbf{B}_i^b=\begin{bmatrix}\mathbf{B}_i^{b1} & \mathbf{B}_i^{b2} & \mathbf{B}_i^{b3} & \mathbf{B}_i^{b4}\end{bmatrix} \tag{51}$$

$$\mathbf{B}_i^{b\alpha}=\begin{bmatrix}(N_i(F_\alpha(\boldsymbol{x})-F_\alpha(\boldsymbol{x}_i)))_{,x} & 0\\ 0 & (N_i(F_\alpha(\boldsymbol{x})-F_\alpha(\boldsymbol{x}_i)))_{,y}\\ (N_i(F_\alpha(\boldsymbol{x})-F_\alpha(\boldsymbol{x}_i)))_{,y} & (N_i(F_\alpha(\boldsymbol{x})-F_\alpha(\boldsymbol{x}_i)))_{,x}\end{bmatrix} \qquad \text{where } \alpha=1,2,3,4 \tag{52}$$

where the comma convention is associated with partial derivation. Note that **b** in Eq. 33a, 37 and 40 is the body force per unit volume, while b is the associated new degrees of freedom (*b1*, *b2*, *b3* and *b4*).

2.2.3 Enrichment functions

The jump function that is usually used is as mentioned the Heaviside function, H(x). The Heaviside function may be defined to either have the value 1 or -1, depending on which side of the crack the nodes at interest are located. The function can be defined as follows

$$H(x) = \begin{cases} 1 & \text{if } (x\text{-}x^*)\cdot n \geq 0 \\ -1 & \text{otherwise} \end{cases} \tag{53}$$

with x being an integration point on the domain and x^* is the closest point on the crack to x. Further, the local crack coordinate system is constructed at x^* such that s and n are the respective tangential and normal vectors to the crack, see Figure 10. Further the sign of the Heaviside function will be the sign of the scalar product $(x\text{-}x^*)^*n$.

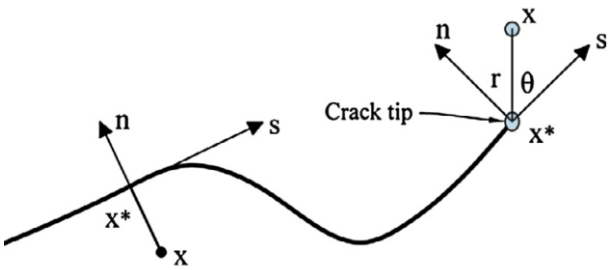

Figure 10 Local normal and tangential coordinates for a crack, with x being the closest point to x on the crack, and (r, θ) defining the polar coordinates of x relative to x*. From Sharafisafa and Nazem (2014).*

The asymptotic crack tip functions, F_α, are defined by using the local polar coordinates r and θ at the crack tip, see Figure 10. As mentioned, one additional degree of freedom will be associated with each of the functions constituting F_α. This may seem like a computational burden, but on the other hand maximum two elements in a 2D model can contain a crack tip, as will be shown in the following sections. The asymptotic crack tip functions, F_α, are defined as follows

$$F_\alpha(r,\theta) = \begin{bmatrix} \sqrt{r}sin\left(\frac{\theta}{2}\right) & \alpha = 1 \\ \sqrt{r}cos\left(\frac{\theta}{2}\right) & \alpha = 2 \\ \sqrt{r}sin\left(\frac{\theta}{2}\right)sin(\theta) & \alpha = 3 \\ \sqrt{r}cos\left(\frac{\theta}{2}\right)sin(\theta) & \alpha = 4 \end{bmatrix} \tag{54}$$

where $\sqrt{r}$ applies for LEFM analysis (Kumar et al., 2013).

2.2.4 XFEM approximation function

A simple 1D rod may be used to illustrate how the XFEM approximation function can be written when a discontinuity is introduced to one of the elements, see Figure 11. The rod consists of three elements and four nodes that are numbered from left to right. The traditional FE approximation function for the displacements without the discontinuity can be written as follows for the 1D rod

$$u^{FE} = u_1 N_1 + u_2 N_2 + u_3 N_3 + u_4 N_4 \tag{55}$$

where u_i is the nodal displacements and N_i is the bilinear shape function at node i.

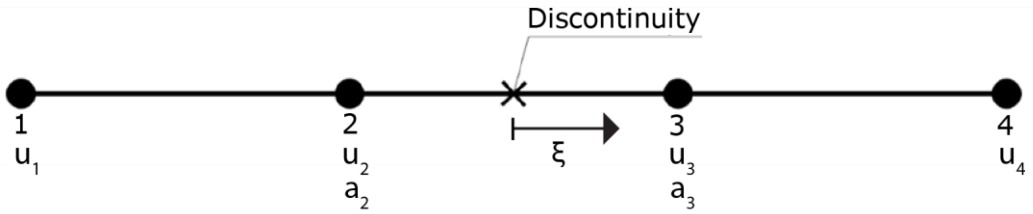

Figure 11 The 1D rod with a discontinuity between node 2 and 3. The degrees of freedom associated with each node is written by the node number, and ξ is aligned with the x-direction. Modified from Gjernes and Klokk (2012).

To be able to describe the influence of the discontinuity the Heaviside enrichment function is used. The Heaviside function, $H(x)$ can generally be defined as in Eq. 53, but will in this simple 1D problem be defined as follows

$$H(x) = \begin{cases} 1 & \text{if } \xi(x) \leq 0 \\ -1 & \text{if } \xi(x) > 0 \end{cases} \tag{56}$$

The complete XFEM approximation function for the 1D rod may now be expressed using the Heaviside function and the new degree of freedom, which is the jumps in displacement, a_n (n = 2,3):

$$u^h = u^{FE} + u^{enriched} = u_1 N_1 + u_2 N_2 + u_3 N_3 + u_4 N_4 + a_2 N_2 H(x) + a_3 N_3 H(x) \tag{57}$$

In this example, the nodes which element is cut by the discontinuity is enriched with the Heaviside function, in this case node 2 and 3. The bilinear shape functions for node 2 and 3 and how the discontinuous Heaviside function influence them are shown in Figure 12.

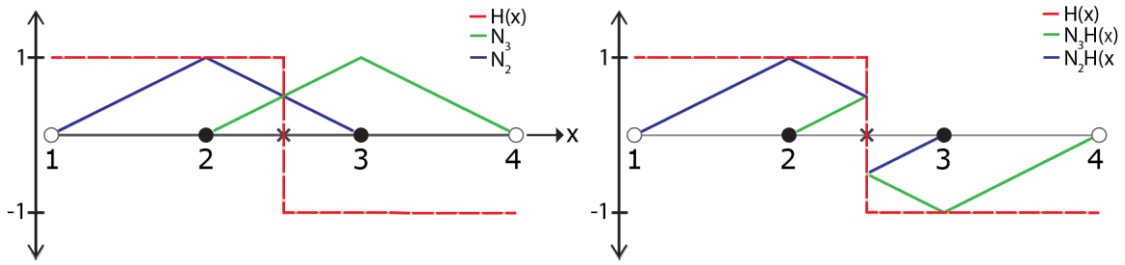

Figure 12 The bilinear shape functions (N_i) associated with the 1D rod in Figure 11. Before (left) and after (right) multiplication with the Heaviside function, H(x). Modified from Gjernes and Klokk (2012).

In a general way, and using a rectangular mesh containing a crack such as the one in Figure 13a) and b), it can be shown how XFEM can describe 2D problems. As for the 1D rod the traditional FE approximation function for the mesh in Figure 13a) and b) can be written on the following form when no discontinuity is present:

$$\mathbf{u}^{\mathrm{FE}} = \sum_{i \in I} \mathbf{u}_i N_i \tag{58}$$

with I being the set of all the nodes in Figure 13. For the case with no discontinuity, all the nodes in the figure will be like the blue circular ones and will only contain the standard degrees of freedom.

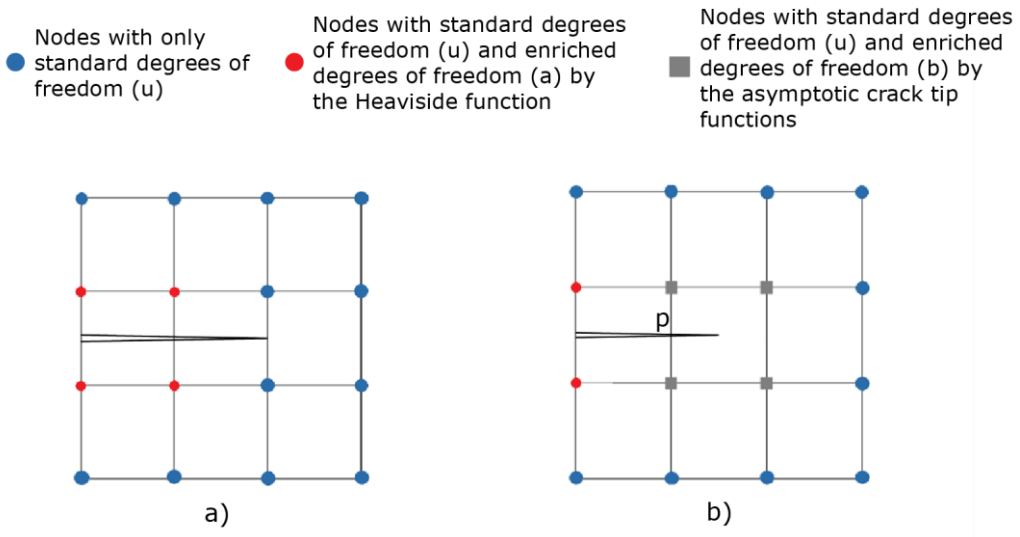

Figure 13 2D finite element mesh containing a crack, and the respective degrees of freedom. ***a)*** *2D mesh containing an edge crack with the crack tip coinciding with an element edge.* ***b)*** *2D mesh containing an edge crack with the crack tip located in the middle of an element. Modified from Moës et al. (1999).*

To appropriately describe the discontinuity in Figure 13a), the nodes which support is completely cut are enriched with the Heaviside function, like for the 1D example. The XFEM approximation becomes the following

$$\mathbf{u}^{\mathrm{h}} = \sum_{i \in I} \mathbf{u}_i N_i + \sum_{j \in J} \mathbf{a}_j N_j H(x) \tag{58}$$

where J is the set containing only the red circled nodes in Figure 13a), and the Heaviside function is defined as in Eq. 53.

Eq. 58 will appropriately describe the type of edge crack illustrated in Figure 13a), but for the case in Figure 13b) the equation will not be sufficient since the crack tip does not coincide with an element edge. The Heaviside enrichment will only model the crack up until point *p* in Figure 13b) and it is in such cases the asymptotic crack tip functions are introduced. The asymptotic crack tip functions will enrich the nodes in the element containing the crack tip, i.e., the square grey nodes in Figure 13b). The XFEM approximation function for such an edge crack problem becomes as follows

$$\mathbf{u}^{\mathrm{h}} = \sum_{i \in I} \mathbf{u}_i N_i + \sum_{j \in J} \mathbf{a}_j N_j H(\boldsymbol{x}) + \sum_{k \in K} N_k \left(\sum_{\alpha=1}^{4} \mathbf{b}_k^{\alpha} F_{\alpha}(\boldsymbol{x}) \right) \tag{59}$$

were K is the set of grey square nodes.

Lastly, the XFEM approximation function may be generalized for an arbitrary crack like the one in Figure 14. The approximation incorporates both crack tips of a crack, and not only the case of an edge crack, and it may be expressed as follows

$$\mathbf{u}^{\mathrm{h}} = \sum_{i \in I} \mathbf{u}_i N_i + \sum_{j \in J} \mathbf{a}_j N_j H(\boldsymbol{x}) + \sum_{k \in K_1} N_k \left(\sum_{\alpha=1}^{4} \mathbf{b}_k^{\alpha 1} F_{\alpha}^{1}(\boldsymbol{x}) \right) + \sum_{k \in K_2} N_k \left(\sum_{\alpha=1}^{4} \mathbf{b}_k^{\alpha 2} F_{\alpha}^{2}(\boldsymbol{x}) \right) \tag{60}$$

where K_1 and K_2 are the sets of grey square nodes belonging to the first and second crack tip, respectively. The sets J, K_1 and K_2 are discussed and defined in more detail in Moës et al. (1999).

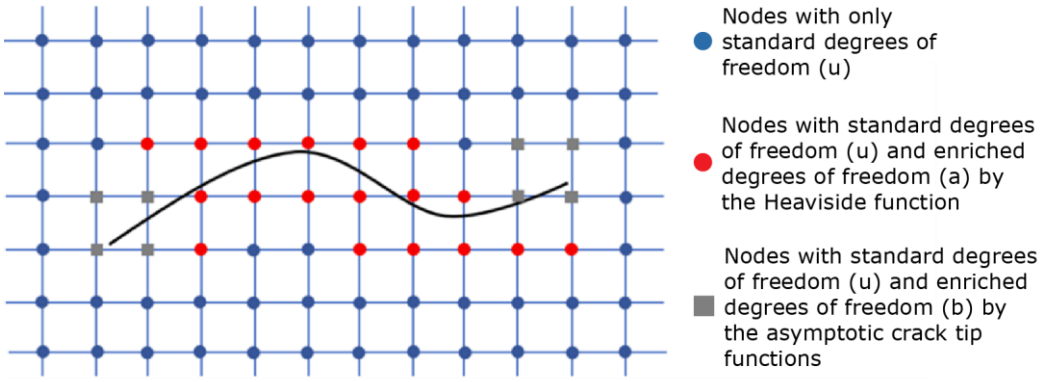

Figure 14 2D Finite element mesh with an arbitrary crack, and the respective nodal degrees of freedom. Modified from Gairola and Ren (2021).

2.3 XFEM in Abaqus

When XFEM is implemented into software, different methods may be used to exploit the XFEM benefits. Abaqus uses the level set method (LSM) to describe discontinuous geometry. Abaqus also uses phantom nodes, a cohesive zone model (CZM) following traction-separation behavior and a Virtual Crack Closure Technique (VCCT) to describe crack initiation and propagation. Generally, there are two approaches to use when simulating cracks using XFEM in Abaqus, namely either CZM or LEFM based XFEM. This section will put forward how XFEM works when modelling crack growth in Abaqus, and how the CZM and LEFM based methods work.

2.3.1 Level sets for a crack

The level set method was first introduced by Osher and Sethian (1988) and was originally a tool to track the evolution of moving boundaries. It was later implemented to XFEM by Stolarska et al. (2001) to solve crack problems. The LSM mainly solved the difficulty in XFEM of keeping track of the evolution of discontinuities, since these are not defined by the FE mesh. Generally, LSM decides whether an element should be crack tip or crack surface enriched.

The evolution of discontinuities such as cracks are in LSM defined using two orthogonal level set functions. The psi (Φ) level set is used to keep track of the crack surface, while the phi (ψ) level set function is used to keep track of the crack tip. This makes it possible to describe the crack using nodal data. Multiple phi level set functions must be used if multiple crack tips are present, one for each crack tip. The two level set functions are defined as follows

$$\begin{aligned} &\Phi(x) < 0 \quad below\ crack\ path && \psi(x) < 0 \quad behind\ crack\ tip \\ &\Phi(x) > 0 \quad above\ the\ crack\ path && \psi(x) > 0 \quad in\ front\ of\ the\ crack\ tip \\ &\Phi(x) = 0 \quad at\ the\ crack\ path && \psi(x) = 0 \quad at\ the\ crack\ tip \end{aligned} \tag{60}$$

Figure 15 illustrates how the nodal data is assigned and how the crack tip is defined at the point where both level sets, Φ and ψ, equal zero.

Node	Φ	Ψ
1	+0.25	−1.5
2	+0.25	−1.0
3	−0.25	−1.5
4	−0.25	−1.0

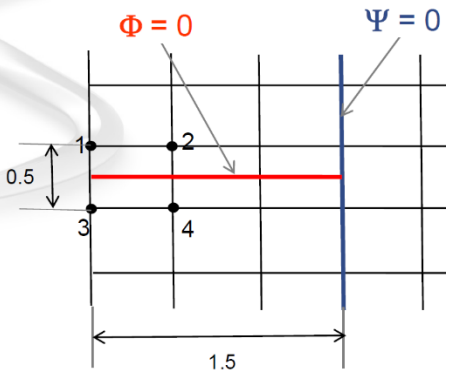

Figure 15 Principle of the Psi (Φ) and Phi (ψ) level set functions, with the crack tip being defined as where both the functions have the value 0. From Du (2016).

The criterion used to decide if an element is enriched with the Heaviside function, or the asymptotic crack tip function, is given as follows

$$\Phi(x) = 0 \quad and \quad \psi(x) < 0 \quad => H(x)\ enriched \tag{61}$$

$$\Phi(x) = 0 \quad and \quad \psi(x) = 0 \quad => F_{\alpha}(x)\ enriched \tag{62}$$

In Abaqus these functions are represented in the output as PSILSM (Φ – Level set method) and PHILSM (ψ – Level set method).

2.3.2 Phantom nodes

To compute propagating cracks Abaqus uses phantom nodes as a method to partition elements and thereby represent the discontinuity. The phantom nodes are superimposed on the original real nodes, and when an element is intact (no discontinuity has cut it), each phantom node is completely constrained to its corresponding real node. As an element is cut by a discontinuity, either a cohesive law or the strain energy release rate describes the magnitude of separation between the real nodes and the phantom nodes. When the separation between them have increased enough so that the cohesive strength is exceeded or the critical strain energy release rate is reached, the nodes start to move independently. The original element is now split into two elements which is described by both real and phantom nodes. The phantom nodes will behave as real nodes and contain information about the displacement field (Systèmes, 2009). The principle of the phantom node method is illustrated in Figure 16.

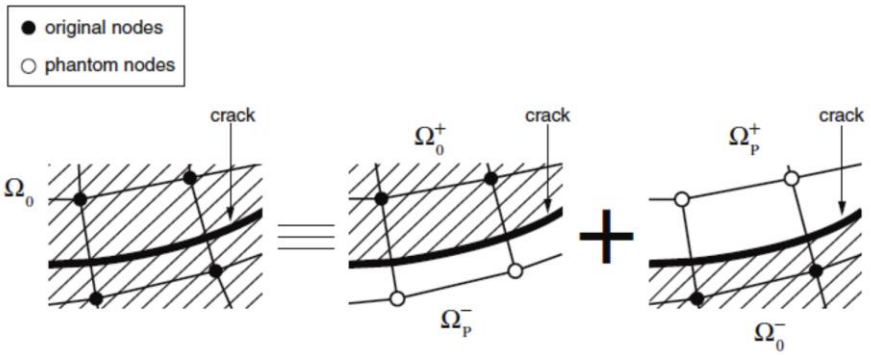

Figure 16 The principle of the phantom node method, where Ω_0 is the real domain, Ω_p is the phantom domain and the superscripts + and – indicate which side of the crack the domains represent. From Systèmes (2009).

2.3.3 Enrichment functions in Abaqus (stationary vs. propagating cracks)

It is important to note that Abaqus differentiate between modelling either stationary or growing (propagating) cracks. When modelling stationary cracks, both enrichment functions, $H(x)$ and $F(x)$, are used, but when modelling growing cracks, only the Heaviside function is used. Generally, this means that for modelling of stationary cracks the crack tip can be located anywhere within an element, but only static analysis will be possible. Modelling of propagating cracks demand complete splitting of an element using phantom nodes, and therefore the crack tip will always be located at an element edge. So, for propagating cracks in Abaqus the crack tip will always be located somewhat like the crack tip in Figure 13a), and the affected nodes are only enriched with the Heaviside function. Note that a crack may split an element in two in any way possible, and Figure 13a) illustrates only one way of splitting an element in two.

2.3.4 Crack initiation with Maximum Principal Stress (Maxps)

The damage initiation criterion for a crack, i.e., crack initiation criteria, is in this study chosen to be the maximum principal stress criterion (Maxps-criterion). This is a built-in crack initiation criterion in Abaqus which initiates a crack when an element is subjected to a user defined stress value. The maximum principal stress criterion can be represented as

$$f = \frac{\langle \sigma_{max} \rangle}{\sigma_{max}^{o}} \tag{63}$$

where σ_{max}^{o} represents the user defined maximum allowable principal stress and $\langle \sigma_{max} \rangle$ is the maximum computed stress in an element in Abaqus. The Macauley brackets are used to define $\langle \sigma_{max} \rangle$ as 0 if $\langle \sigma_{max} \rangle < 0$ and $\langle \sigma_{max} \rangle$ as σ_{max} if $\sigma_{max} \geq 0$. This is to signify that pure compressional stress (which is defined as negative stress in Abaqus) does not initiate

damage. Damage (i.e., cracks) will initiate when f in Eq. 63 reaches a value of 1 (Systèmes, 2009).

Further it can be defined where in an element the principal stress should be calculated from. The following options are available for local calculations of the stress and strain fields ahead of the crack tip: the centroid of an element, the position of the crack tip, or a combination of these two, see Figure 17.

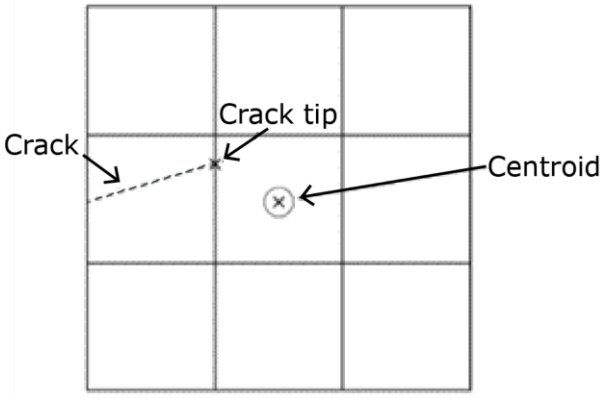

Figure 17 2D finite element mesh containing a crack, and two of the options of where the stress may be calculated from, i.e., at the crack tip or at the centroid of an element. Modified from Systèmes (2009).

The crack propagation direction is in this criterion set to be perpendicular to the maximum principal stress direction, which consequently is in the direction where the shear stress equals zero. In Abaqus there is also an option of nonlocal averaging of the stress and strain field to improve the accuracy of crack propagation directions, see Figure 18. The default radius used for non-local averaging is three times the typical element characteristic length in the enriched region (Systèmes, 2009).

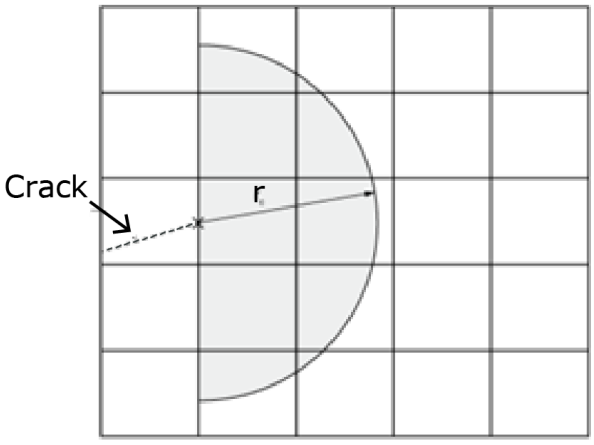

Figure 18 Non-local averaging from the crack tip using the radial distance r. Modified from Systèmes (2009).

2.3.5 Crack propagation with Cohesive Zone Method

The damage evolution in an element is described by introducing a damage variable, *D*, which initially has the value 0 when the damage initiation criterion is first met. Upon further loading, *D* will monotonically increase from 0 towards 1. This damage evolution law will describe the rate at which the cohesive stiffness is degraded in an element, and in this way simulate the fracture process zone (FPZ) which is an area of plastic deformations ahead of the crack tip, see Figure 19. The damage evolution law is described by a traction separation law, see Figure 20. The area under the Traction-Separation curve is the fracture energy, G_C, which is the input criterion used to govern the degradation of the cohesive tractions across a crack in an element when using CZM based XFEM. When the area under this curve reaches G_C, the element becomes completely separated by the crack. Both linear and nonlinear traction separation responses are available in Abaqus. In addition, mixed mode G_C-values may be calculated from BK-, Power- or Reeder-law, see section 2.3.6.

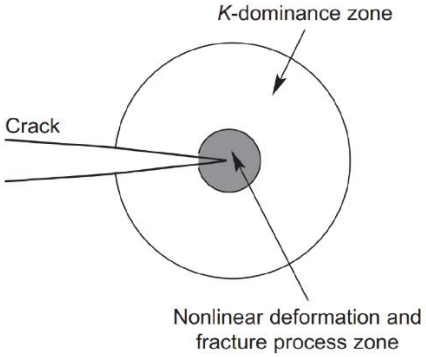

Figure 19 The zone in front of a crack tip that may be expressed using the fracture toughness, K (K-doinance zone) and the plastic zone at the vicinity of the crack tip called the "fracture process zone". From Sun and Jin (2012c).

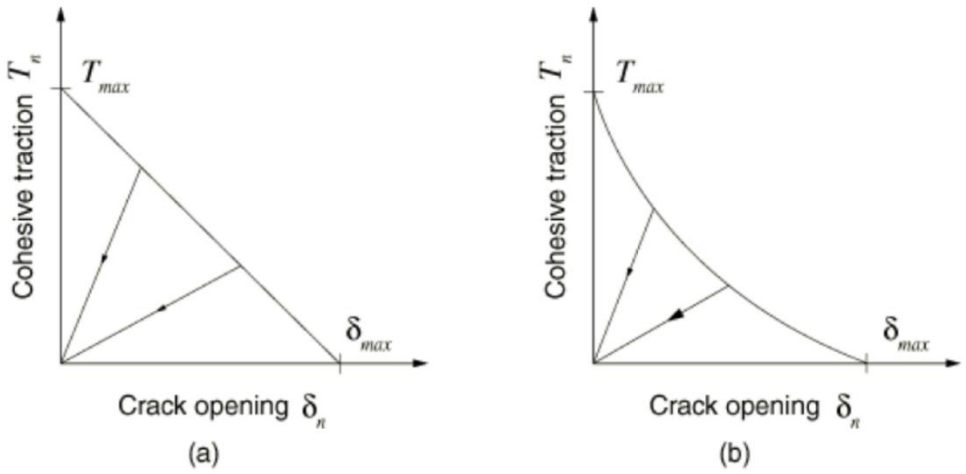

*Figure 20 Linear (**a**) and non-linear (**b**) damage evolution, following traction-separation law. From Systèmes (2009).*

It is important to note that in this CZM based XFEM method in Abaqus, it is the Maxps-criterion that governs the initiation of the damage evolution described above, for every time the crack propagates through an element. In other words, every crack propagation in the CZM based XFEM is dependent on both the Maxps-criterion and the damage evolution from the traction separation law.

2.3.6 Crack propagation with Linear Elastic Fracture Mechanics

In the LEFM based XFEM method in Abaqus, crack propagation is governed by the strain energy release rate, also denoted G. The strain energy release rate is calculated at the crack tip based on the modified Virtual Crack Closure Technique (VCCT) and propagation of a crack will occur when G reaches the critical energy release rate, G_C, which is based on criterions set by the user. This criterion will in the following be referred to as the ERR-criterion. The general idea of the VCCT method is described in more detail by Krueger (2002). To allow for mixed mode behavior, Abaqus have the options of using either BK-, Power- or Reeder-law. The Power-law is described by Wu and Reuter (1965) by the following formulae

$$\frac{G}{G_C} = \left(\frac{G_I}{G_{IC}}\right)^{a_m} + \left(\frac{G_{II}}{G_{IIC}}\right)^{a_n} + \left(\frac{G_{III}}{G_{IIIC}}\right)^{a_o} \tag{64}$$

where G_I, G_{IC}, G_{II}, G_{IIC}, G_{III}, G_{IIIC} are the respective Mode I, Mode II and Mode III strain energy release rates and critical strain energy release rates, respectively, while a_m, a_n and a_o are the weighted exponents to each of the three contributions. In Eq. 64, G_{IC}, G_{IIC}, G_{IIIC} are criterions set by the user based on material properties.

Since this approach is based on LEFM it requires a pre-existing crack before it becomes active. In Abaqus, the Maxps-criterion may be used to initiate new cracks, before the LEFM method becomes active and governs the propagation of the newly developed crack. Further, the crack propagation direction may be chosen to be either normal or parallel to the local 1-direction in Abaqus, or it may be governed by the MS-criterion (section 2.1.4).

2.3.7 Rotation of coordinate system

In Abaqus, the horizontal (U1) and vertical (U2) displacements are easily available as outputs. To find the relative displacements across a crack that is at an angle to the U1 and U2 directions, a rotation of the coordinate system is necessary. Considering the two nodes P and P' that makes a line that is approximately normal to the crack, and measuring the angle β, see Figure 21, the following relation may be used to calculate the relative normal and shear displacements across a crack

$$\begin{bmatrix} U_{Normal} \\ U_{Shear} \end{bmatrix} = \begin{bmatrix} U1 * \cos\beta + U2 * sin\beta \\ -U1 * sin\beta + U2 * cos\beta \end{bmatrix} \tag{65}$$

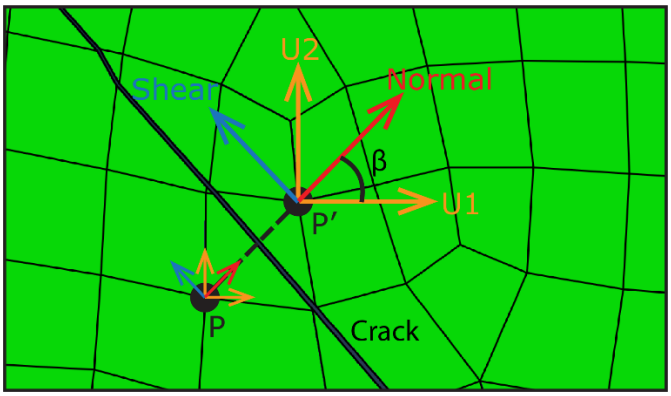

Figure 21 Nodes P and P' defining the Normal and Shear coordinate system relative to the global coordinate system in Abaqus. U1 is in the x-direction, and U2 is in the y-direction.

3 Model set-up and material properties

3.1 Geometry, crack domains and element mesh

The analysis in this study was carried out using a two-dimensional plane strain XFEM model in Abaqus. The model consisted of rectangular specimens (60x120mm) containing a single pre-existing open flaw with the length and width of 15 and 1 mm, respectively, and rounded flaw tips. The specimens were subjected to uniaxial compression by restraining the bottom in the y-direction while the top part was displaced downwards at a constant velocity of -0.00029 mm/s, for a total of 1200 s. In addition, the bottom is restricted from rotation and the bottom right corner is restricted in the x-direction.

In total six models were used, with the difference being the inclination angle, α, of the pre-existing open flaw - 30, 45 and 60 degrees – and that the models were simulated using both CZM and LEFM based XFEM. Pre-defined crack domains are necessary to select the nodes to be enriched with additional degrees of freedom. These crack domains are chosen based on experimental studies, and on where cracks are expected to grow. In this type of model, it is expected that wing and anti-wing cracks may initiate and propagate in proximity of the pre-existing flaw tips. The geometry of the specimen together with the crack domains are shown in Figure 22, while the boundary conditions are shown in Figure 23. The geometry of the specimens are like the specimens used in laboratory testing by Zhang et al. (2021).

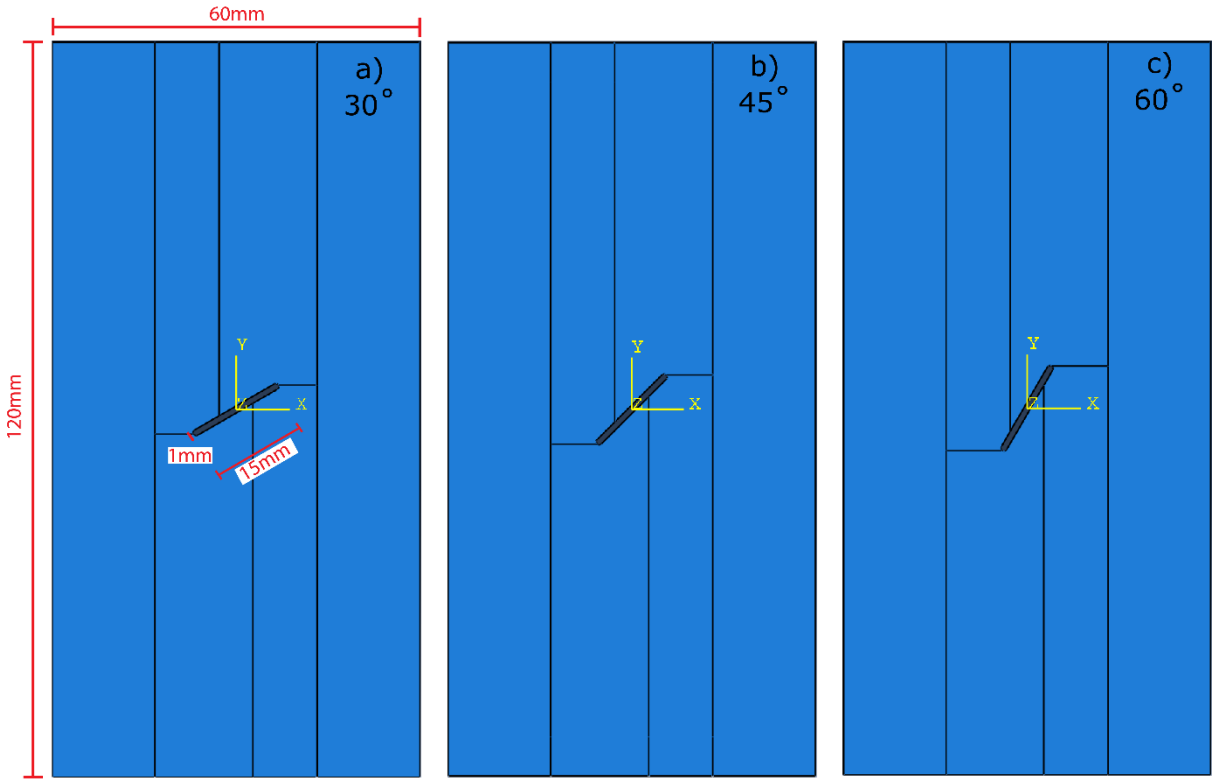

Figure 22 Geometry and crack domains in both the CZM and LEFM models. Each models has 4 crack domains around the pre-existing flaw. ***a)*** *30-degree inclination angle.* ***b)*** *45-degree inclination angle.* ***c)*** *60-degree inclination angle.*

The mesh consists of 4-node bilinear plane strain quadrilateral elements (CPE4R), solved with reduced integration. To capture crack initiation and propagation the crack domains consist of a relatively fine mesh of 0.5 mm elements, while the rest of the specimen is made up of elements ranging from 0.5-3 mm, see Figure 23. The 30-, 45- and 60-degree models consist of 20940, 20761 and 21087 elements, respectively.

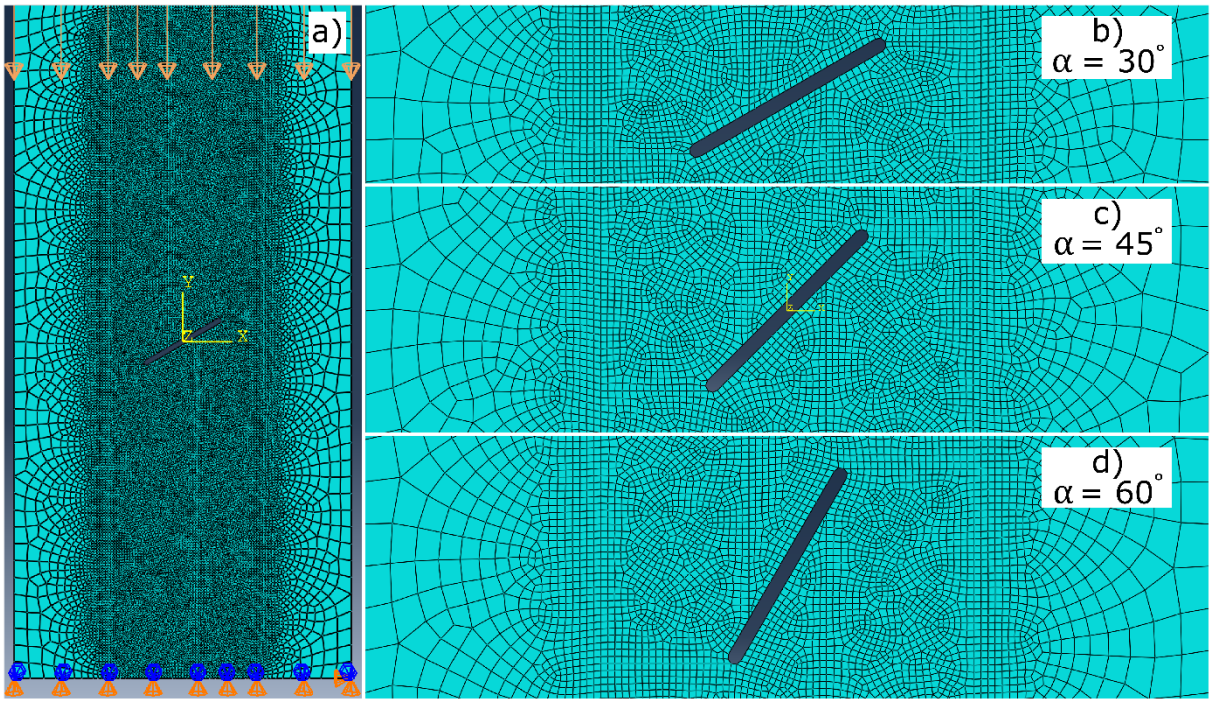

Figure 23 The element mesh and boundary conditions used in the models. ***a)*** *The complete mesh together with the boundary conditions.* ***b)*** *Close up of the mesh around the 30-degree flaw, later referred to as the "30-degree model".* ***c)*** *Close up of the mesh around the 45-degree flaw, later referred to as the "45-degree model".* ***d)*** *Close up of the mesh around the 60-degree flaw, later referred to as the "60-degree" model.*

3.2 Material properties and input parameters

The material used in the models is assigned with a Young's modulus of 62 GPa and a Poisson's ratio of 0.22, while the material density is set to $2.7*10^{-9}$ tonne/mm^3. These elastic material properties are the same as the ones used in laboratory tests by Zhang et al. (2021). The tensile strength of the granite used by Zhang et al. (2021) ranged between 15.8 and 17.4 MPa. Based on these tensile strength values, the Maxps-criterion was set to 20 MPa. The reason for this is to account for some shear strength, as the Maxps-criterion is a combination of both Mode I and Mode II failure modes. Further, the critical fracture energy/energy release rate values, G_{IC} and G_{IIC}, are set to 0.001 and 0.1 N/mm, respectively. From laboratory tests carried out by Lei et al. (2017), the measured values of G_{IC} and G_{IIC} were 0.074 and 0.088 N/mm, respectively. However, these values lead to poor crack growth in some of the initial simulations, and the G_{IC}-value used in the models

was therefore reduced and the G_{IIC}-value used was increased, as tensile cracks were expected to dominate. The Power law is used to calculate the combined critical value, G_c, in both the CZM and LEFM models. Lastly, to facilitate convergence resulting from the presence of discontinuities that makes the structural response nonlinear, a viscosity parameter of $1*10^{-5}$ was used (Du, 2016, Sivakumar and Maji, 2021). All the material properties adopted to the numerical model, as well as the displacement velocity, is listed in Table 1. The crack initiation and propagation criterions used are listed in Table 2.

Table 1 Material properties and input parameters.

Material properties/ input parameters	**Values**
Young modulus, E (GPa)	62
Poisson's ratio, v	0.22
Maxps (MPa)	20
G_{IC} (Mode I) (N/mm)	0.001
a_m	1
G_{IIC} (Mode II) (N/mm)	0.1
a_n	1
Viscosity	$1*10^{-5}$
Velocity (mm/s)	-0.00029
Time period (s)	1200

Table 2 Crack initiation and propagation criteria. The Maxps- and MS-criteria are both governed by the local maximum tensile stress.

Criterion	**CZM**	**LEFM**
Crack initiation	Maxps	Maxps
Crack propagation	Maxps	ERR
Propagation direction	Perpendicular to Maxps-direction	Perpendicular to MS-direction
Damage evolution	Traction-separation law (linear)	-

Other measures to facilitate convergence as cracks propagate was to set the minimum increment size to $1*10^{-20}$, which is a relatively small increment size, while the maximum number of increments was set to 100000. In the General Solution Control Editor "discontinuous analysis" was chosen, and the maximum number of iteration attempts was set to 20. To keep track of crack initiation and propagation, the field outputs PHILSM, PSILSM, STATUSXFEM and ENRRTXFEM were used. The ENRRTXFEM output must be written manually in the Abaqus Keywords.

4 Results

4.1 Stress and crack analysis

To investigate how the stress field in the specimen is affected by the pre-existing open flaw when a compressional load is applied, a stress analysis is carried out, as well as an analysis of the initiation and propagation of wing and anti-wing cracks. Firstly the 45-degree models are analyzed, followed by an analysis of all the inclination angles, i.e., 30-, 45- and 60-degree.

4.1.1 Single 45-degree open flaw analysis

When a compressional load is applied to the specimen in Figure 22b), it is observed that both wing cracks and anti-wing cracks are initiated in both the CZM and the LEFM model. In both models the anti-wing cracks propagate through the whole specimen, while only in the CZM model the wing cracks propagate fully through the specimen, see Figure 24.

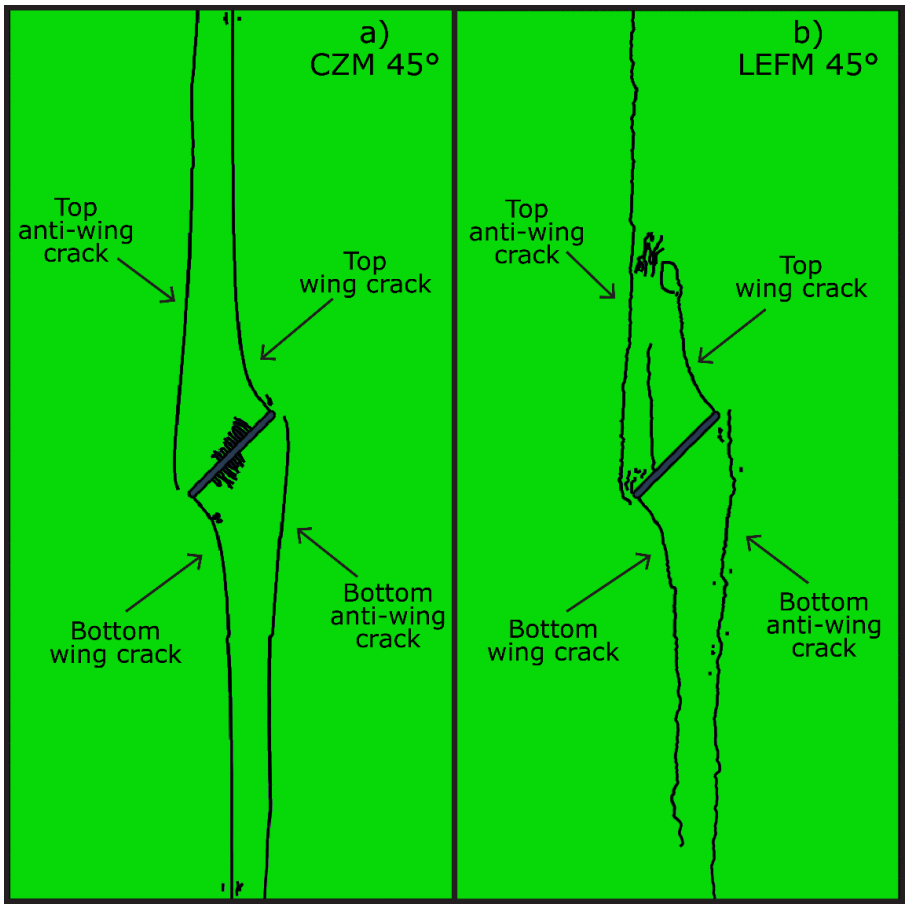

Figure 24 CZM and LEFM models after 178 and 172 *MPa axial stress, respectively. Full size of the models.* ***a)*** *45-degree CZM model.* ***b)*** *45-degree LEFM model.*

When load is first applied to the specimen, stress concentrations are observed around the pre-existing open flaw. After an axial load of 10 MPa, the compressional stress at the outside of the flaw tips reaches a value of -50.4 MPa, while the tensile stress on the inside of the flaw tips reaches a value of 15.6 MPa, see Figure 25. The stress field is affected by the pre-existing flaw already at relatively small loads, and especially the tensile stress concentrations are critical since the tensile strength of many rocks often range between 5 and 20 MPa (Perras and Diederichs, 2014).

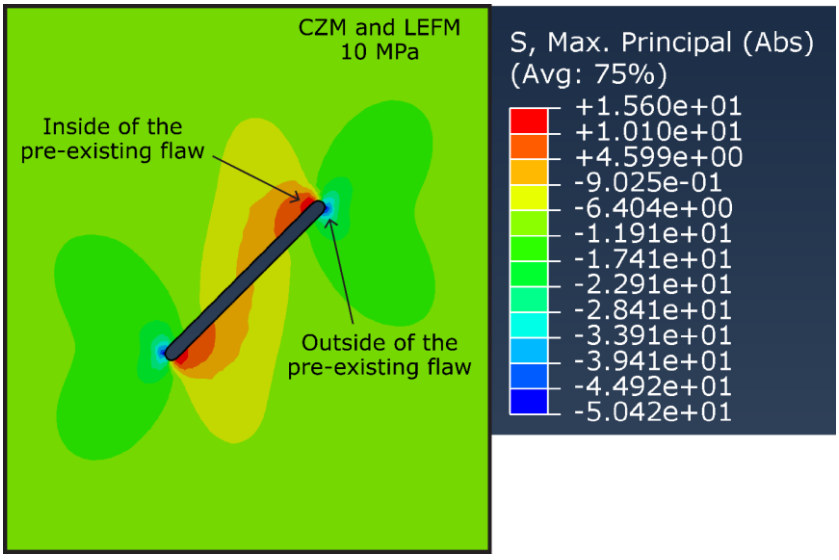

Figure 25 Stress field around the pre-existing 45-degree open flaw when the applied axial load is 10 MPa. The values are the same for the CZM- and LEFM-model. "S, Max. Principal (Abs)" displays the absolute greatest stress values [MPa]. Load is applied in the U2 (vertical) direction and tensile stress is defined as positive values.

Upon further loading, the concentration of tensile stress seen on the inside of the flaw tip in Figure 25 continues to increase. The crack initiation criterion of 20 MPa is eventually reached, resulting in the initiation of wing cracks in both the CZM and the LEFM model. For the CZM-model, both the wing cracks initiate when the applied load is 13.2 MPa in the elements located at the inside of the pre-existing flaw tips, see Figure 26a). The wing crack initiate when the applied load is 12.9 MPa for the LEFM model, in the same locations and elements as for the CZM model, see Figure 26b). In the LEFM model, the bottom wing crack is observed to propagate through four elements (including the element that the crack initiated in) before the top wing crack initiates, but this is not the case in the CZM model.

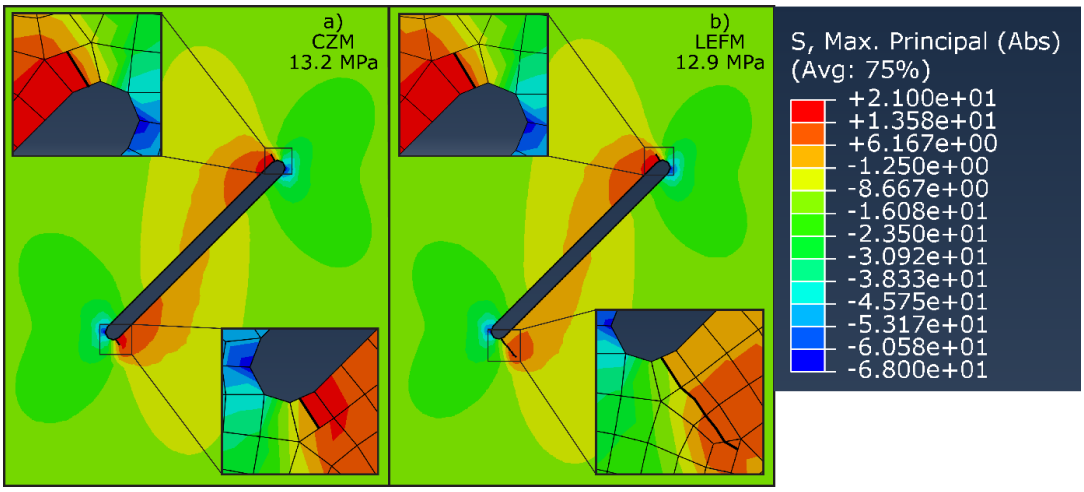

*Figure 26 Crack initiation of wing cracks in both models. In the LEFM-model the bottom wing crack initiate and propagate a small distance before the top wing crack initiates. The first element that the crack initiates in is in both **a)** and **b)** governed by the Maxps-criterion, after which the ERR-criterion governs the rest of the propagation in **b)**. "S, Max. Principal (Abs)" displays the absolute greatest stress values [MPa]*

As the load is increased, the wing cracks propagate in approximately the same direction as the initial crack initiation direction, until it curves towards a vertical propagation direction for both models. For the CZM model, the wing cracks propagate steadily in the initial initiation direction until a load of 30 MPa has been applied, and the cracks have reached a length of approximately 5 mm. After this point, both the wing cracks are observed to curve and eventually align with the vertical direction, i.e., the direction of the applied load. The wing cracks in the CZM model continue to propagate steadily, with propagations in the load increments which satisfy the crack initiation criterion of 20 MPa. The development of the top wing crack in the CZM model, from its initiation until it reaches a sub-vertical direction, is shown in Figure 27a)-d). The wing crack in the CZM model continues to propagate up until 139 MPa of applied load is reached, and at this point the anti-wing cracks initiate, see Figure 28b). At this applied load both the anti-wing and wing cracks propagate fully through the specimen, as can be seen in Figure 24a).

For the LEFM-model, the top wing crack propagates in the initial initiation direction until an applied load of about 22 MPa is reached, and the crack has grown to a length of approximately 5 mm. Further, the wing crack curves towards a more vertical direction and eventually aligns with the direction of the applied load. The wing cracks are observed to propagate for every load increment that satisfies a strain energy release rate of 0.001 N/mm in the element in front of the crack tip, and this happens progressively as the applied load increases. The development of the top wing crack in the LEFM model is shown in Figure 27e)-h). Both the wing cracks in the LEFM model continue to propagate until an applied load of 141 MPa has been reached, and at this point both the anti-wing cracks initiate, see Figure 28e). The growth of the top wing crack is observed to get somewhat suppressed as the top anti-wing crack begins to propagate, and this wing-crack reaches its maximum length of about 20 mm when the applied load is 160 MPa. The bottom wing crack does not experience the same suppression and continues to propagate until the maximum loading of 172 MPa has been reached. The bottom wing crack has at this point propagated almost fully through the specimen. It is when the applied load is 141 and 160 MPa that the bottom wing crack propagates the longest distances. The difference between

the full development of the top and bottom wing cracks in the LEFM model can be seen in Figure 24b).

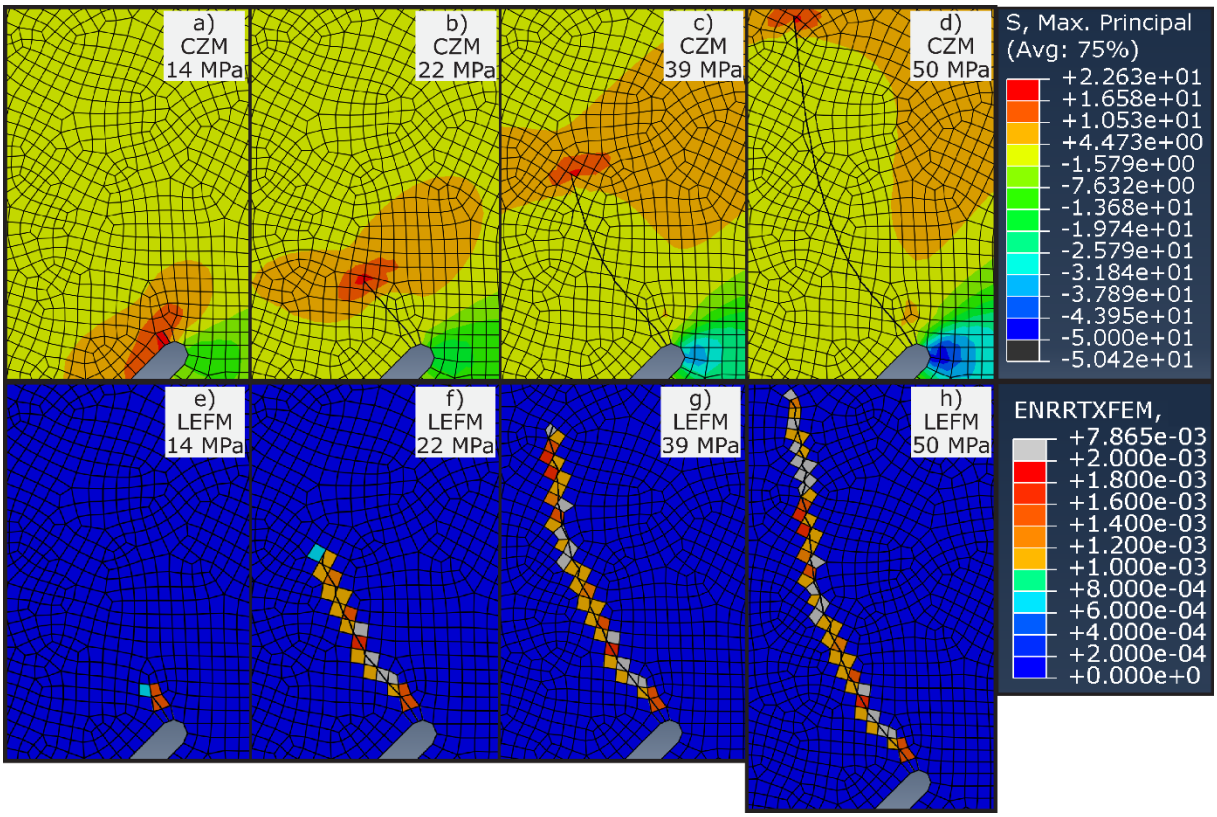

*Figure 27 Close up of the top pre-existing flaw tip where the top wing crack initiates and propagates through the finite elements. For **a)**, **b)**, **c)** and **d)** this is at the load increment before the element at the crack tip reaches 20 MPa (Maxps-criterion). For **e)**, **f)**, **g)** and **h)** this is at the load increment before the energy release rate in the element in front of the crack tip reaches 0.001 N/mm (ERR-criterion). "S, Max. Principal" displays the maximum principal stress [MPa], and "ENRRTXFEM" displays the energy release rate [N/mm].*

As the wing cracks propagate, tensile stress concentrations are observed to the let of the top wing crack and to the right of the bottom wing crack, in both the models, see Figure 28a) and d). The stress concentrations are symmetrical across the pre-existing flaw. The stress concentrations in these areas are first observed to be a part of the stress field around the wing crack tips before they become individual stress concentration areas. For the CZM-model, when the applied load has reached 98 MPa, the stress concentrations in these areas are about 13 MPa and they are oriented sub-horizontally, which is the case in Figure 28a). Upon further loading, the stress concentrations reach the crack initiation criterion of 20 MPa, and anti-wing cracks are initiated in the elements first reaching this assigned value, see Figure 28b). The applied load is 139 MPa when this happens in the CZM model. The anti-wing cracks initiate in a sub-vertical direction, which coincides with the sub-horizontally oriented tensile stresses in the areas, and they further propagate from both their crack tips. The anti-wing cracks propagate in their initial sub-vertical orientation before they adjust to a more vertical direction. The crack tips closest to the pre-existing flaw curve very slightly towards their respective pre-existing flaw tips in the CZM model,

see Figure 28c) and Figure 24a). However, they never coalesce with the pre-existing flaw. Both the anti-wing cracks initiate and propagate fully through the specimen at the 139 MPa loading step. Both the wing cracks also continue their propagation fully through the specimen at this stage. The complete development of the wing and anti-wing cracks in the 45-degree CZM model can be seen in Figure 24a).

When the applied load reaches 98 MPa in the LEFM-model, the tensile stress concentrations are about 13 MPa in the described areas, see Figure 28d), and they are also oriented sub-horizontally. As more load is applied, the anti-wing cracks initiate at an applied load of 141 MPa, and the initiation direction is sub-vertical. The anti-wing cracks then propagate according to the energy release rate values in the elements in front of the crack tips, see Figure 28e). The top anti-wing crack propagates almost fully through the specimen at the 141 MPa loading stage, but stops about 1 cm from the top of the specimen. When the applied load reaches 160 MPa, the top anti-wing crack continues its propagation fully through the specimen together with the bottom anti-wing crack, which propagates fully and almost exclusively through the specimen at this loading stage. Both the anti-wing cracks are observed to not curve towards the pre-existing flaw tips, but rather continue in their sub-vertical propagation direction, and they are thereby surpassing the pre-existing flaw tips, which can be seen in Figure 24b). The crack tip closest to the pre-existing flaw in the top anti-wing crack does however curve slightly after it has surpassed the flaw. The crack tips propagating towards the end of the specimen are observed to align with the vertical loading direction, see their complete development in Figure 24b). The stress-strain curves for the 45-degree CZM and LEFM models are shown in Figures 29 and 30, respectively (these figures are also presented in the Appendix).

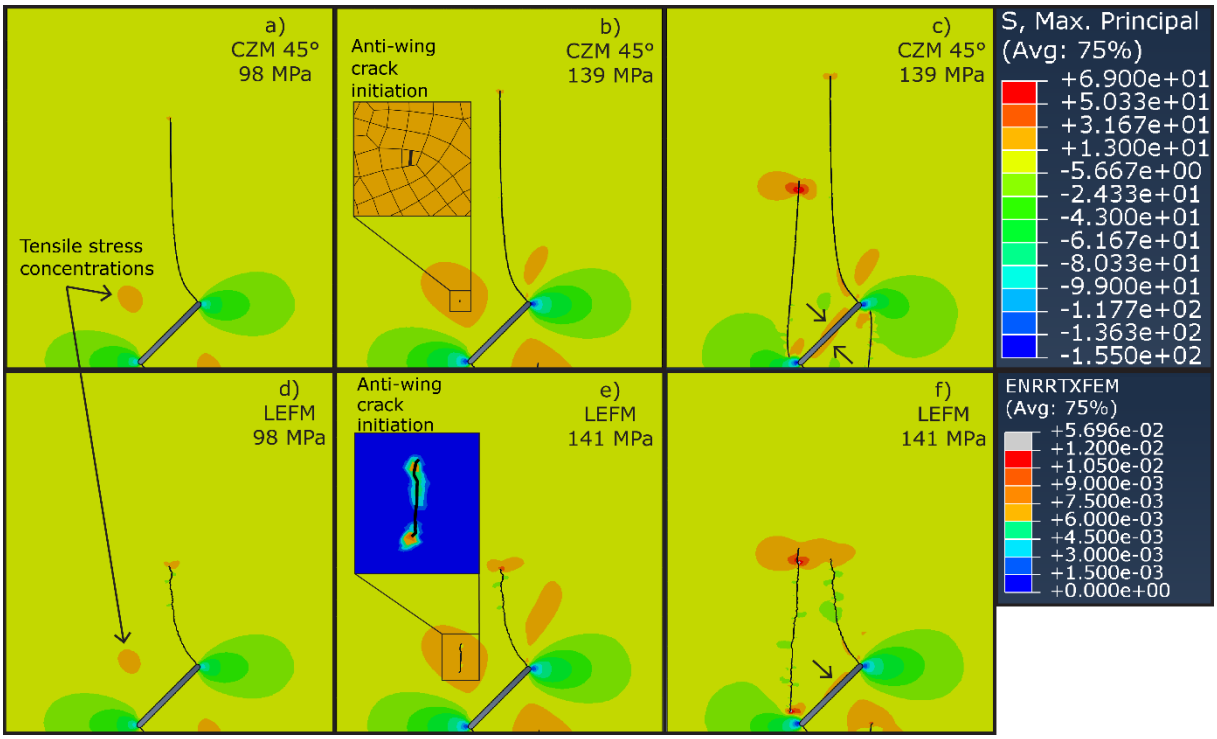

*Figure 28 Development of the anti-wing cracks. **a)**, **b)** and **c)** development of the anti-wing crack in the CZM model. **d)**, **e)** and **f)** development of the anti-wing crack in the LEFM model. "S, Max. Principal" displays the maximum principal stress [MPa], and "ENRRTXFEM" displays the energy release rate [N/mm].*

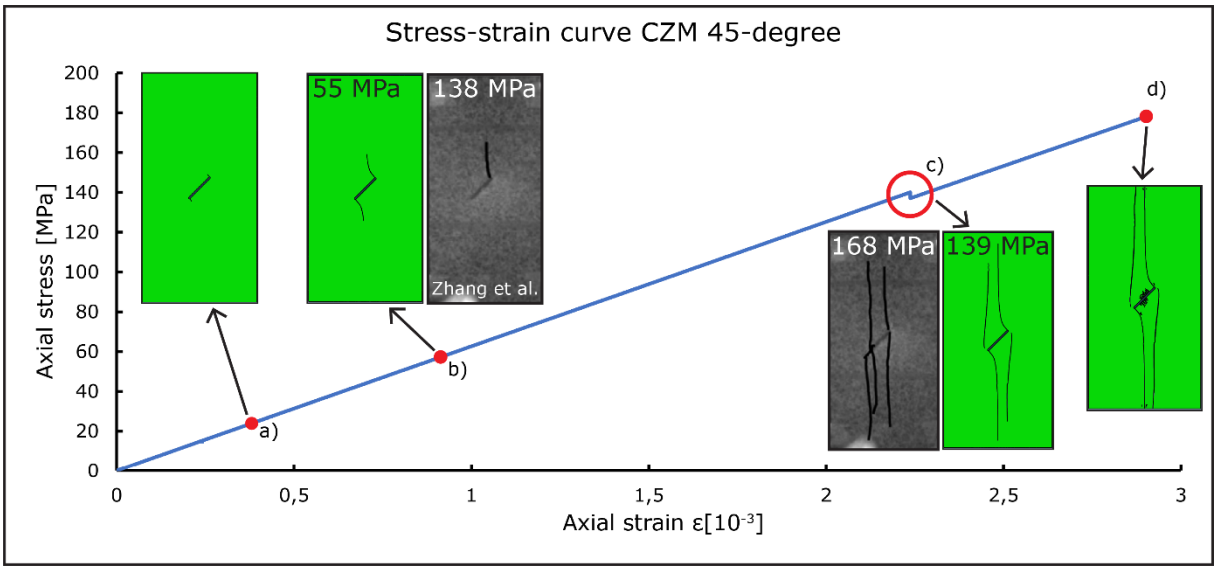

*Figure 29 Stress-strain curve for the 45-degree CZM model, with crack development and comparison to experimental results by Zhang et al. (2021). Stable wing crack growth from **a),** through **b),** and to **c),** then unstable/rapid wing and anti-wing crack growth in **c),** and lastly full development in **d)**. The figure is also presented in the Appendix.*

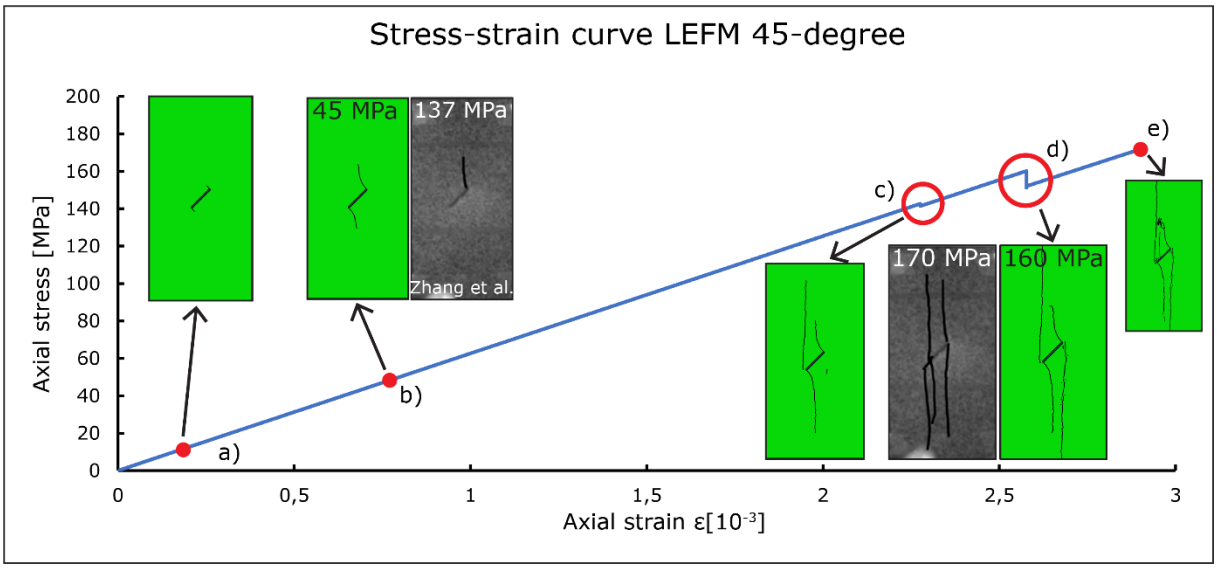

*Figure 30 Stress-strain curve for the 45-degree LEFM model, with crack development and comparison to experimental results by Zhang et al. (2021). Stable wing crack growth from **a),** through **b),** and to **c),** then unstable/rapid wing and anti-wing crack growth in **c)** and **d),** and lastly full development in **e)**. The figure is also presented in the Appendix.*

Stress concentrations do also occur on the right side of the top wing crack as can be seen in Figure 28b), c) and e). This is also the case for the bottom wing crack in both models (on their left side). In the same manner as the tensile stress concentrations described above, these tensile stress concentrations are also initially a part of the wing crack tip stress fields before they become individual stress concentration areas. As the anti-wing and wing cracks propagate through the specimen, the tensile stress in these areas reaches above 20 MPa in the LEFM model, but no cracks initiate since the crack domain is occupied by the wing cracks. These stress concentration areas shrink somewhat in the LEFM model as the top anti-wing crack propagates, see Figure 28f), but they expand again shortly after (at the same applied load). In the CZM model, these stress concentrations also reach above 20 MPa as the anti-wing and wing cracks propagates through the specimen, but no new cracks initiate since the crack domain is occupied. However, a small crack is observed to initiate on the right side of the top wing crack in the CZM model when the top wing crack has propagated fully through the specimen, and this small crack is visible in Figure 24a).

After the initiation of the anti-wing cracks, stress concentrations are also observed around the long sides of the pre-existing flaw in both the models, see Figure 28c) and f). These types of stress concentrations are also observed to a small degree as the wing cracks initiate, but they decrease after some propagation. It is not before the initiation and propagation of the anti-wing cracks that they increase largely and very rapidly. Just as the anti-wing cracks initiates in Figure 28b) and e), the tensile stresses around the long sides of the pre-existing flaw are negligible, whereas when the anti-wing cracks have propagated some centimeters, the same area reaches tensile stresses of 25 to 35 MPa in both the models. These are relatively high stresses, which theoretically can initiate new cracks according to the Maxps-criterion. However, no cracks are initiated at this point since only one crack can be active in a crack domain at the same time. When the anti-wing cracks have reached the ends, the stress concentrations have reached values between 50 and 70 MPa, and consequently cracks initiate in the described areas in both the models, as can be seen Figure 24a) and b). It is important to note that at the equilibrium increment where the original wing and/or anti-wing cracks reach the ends of their respective domains, i.e., the end of the specimen, many elements in the described area fulfill the Maxps-criterion, and therefore multiple new cracks initiate in the same equilibrium increment. In Figure 28f) only the top side of the pre-existing flaw experience high stress concentrations, and this is because the bottom anti-wing crack has not propagated far enough at this applied load. When the applied load reaches 160 MPa, stress concentrations also occur on the bottom side of the pre-existing flaw in the LEFM model, since the bottom anti-wing crack has propagated further. The full development of these stress concentrations for the CZM model are presented in more detail in section 4.1.2 and in Figure 39b).

4.1.2 Single 30-, 45- and 60-degree open flaw analysis

When the pre-existing flaw inclination angle is varied, some differences appear in the initiation and propagation of the wing and anti-wing cracks. These differences are mainly the crack initiation stresses and wing crack initiation angles. The results achieved from all the models after complete loading are shown in Figure 31.

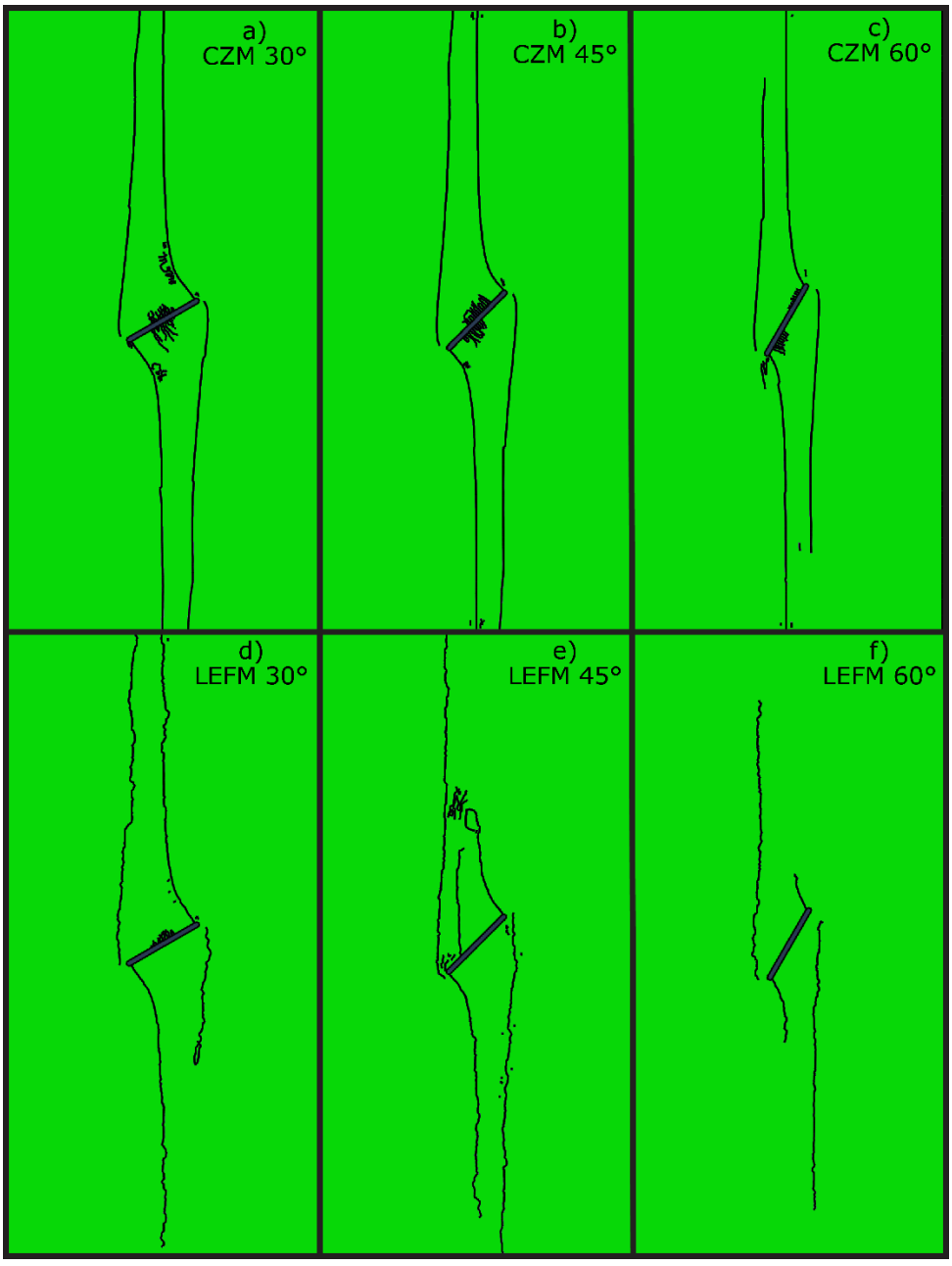

Figure 31 Full development of the cracks in the CZM and LEFM models. ***a)****,* ***b)*** *and* ***c)*** *30-, 45- and 60-degree CZM models after 175, 178 and 170 MPa axial load, respectively.* ***d)****,* ***e)*** *and* ***f)*** *30-, 45- and 60-degree LEFM models after 177, 172 and 183 MPa axial load, respectively.*

The stress field around the pre-existing flaw tip is observed to vary as the flaw inclination angle varies. For the 30-degree model tensile stress concentrations larger than 12.5 MPa (light orange contour) are observed to affect about 75% of the long sides of the pre-existing flaw, see Figure 32a) and d). For the 45-degree model about 50% of the length of the flaw is affected by the same stress concentrations, and less than 25% is affected in the 60-degree model, respectively, see Figure 32b), c), e) and f). Qualitatively, the stress field gets more concentrated around the pre-existing flaw tip as the inclination angle increases. The stress concentrations around the pre-existing flaw in Figure 32 increase faster in the 30-degree model, resulting in wing crack initiation at an applied load of 12.5 MPa in the CZM model, and 12.4 MPa in the LEFM model. For the 45-degree model the wing cracks initiate at an applied stress of 13.2 and 12.9 MPa, while for the 60-degree model the wing cracks do not initiate until the applied load reaches 15.5 and 15.6 MPa for the CZM and LEFM model, respectively, see Figure 32. It is also observed that the wing cracks initiate further from the crack tips in the 30-degree models, compared to the 45- and 60-degree models. The wing crack initiation stress for the different flaw inclination angles are also shown in Figure 40.

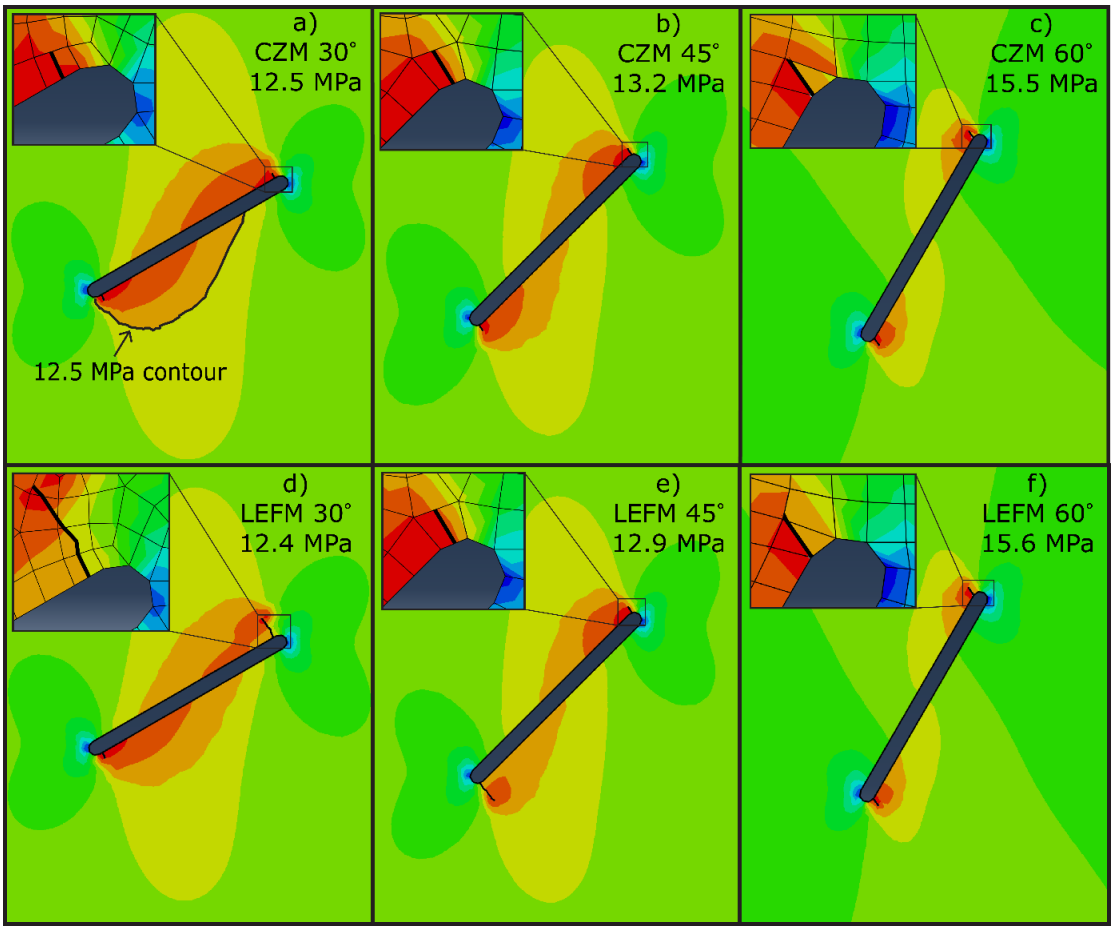

Figure 32 Wing crack initiation for the different inclination angles. Same legend as Figure 26. ***a)****,* ***b)*** *and* ***c)*** *30-, 45- and 60-degree CZM models, respectively.* ***d)****,* ***e)*** *and* ***f)*** *30-, 45- and 60-degree LEFM models, respectively.*

For all three inclination angles the wing cracks are observed to propagate stably and progressively as the applied load increases. In the 30-degree models the wing cracks propagate stably through about 75% of the specimen until the anti-wing cracks initiate. By measuring the angle between the pre-existing flaw and the propagation direction of the wing cracks, the wing crack initiation angle, θ_0, is found to be 95° for the 30-degree flaw, in both the CZM and LEFM models, see Figure 33a) and d) and Figure 41. The applied load at this stage is 130.5 and 131.6 MPa in the CZM and LEFM models, respectively. Both anti-wing cracks in the 30-degree models initiate in the tensile stress concentration areas at these loading stages, even though only the first anti-wing crack initiation is shown in Figure 33a) and d). Tensile stress concentration areas are also observed on the right side of the top wing crack and left side of the bottom wing crack. The stress in these areas is about 15-16 MPa in both the models when the anti-wing cracks initiate, and they increase to above 20 MPa as the anti-wing and wing cracks propagate fully through the specimen. In both the CZM and LEFM model a small crack is observed to initiate close to the top pre-existing flaw tip after the top wing crack have propagated fully through the specimen, this small crack is visible in Figure 31a) and d).

In the 45-degree CZM model the wing cracks are also observed to propagate stably through about 75% of the specimen before the anti-wing cracks initiate, see Figure 33b). Both the anti-wing cracks initiate at the applied load of 139 MPa in the 45-degree CZM model, in the stress concentration areas when the tensile stress reaches 20 MPa. In the 45-degree LEFM model the wing cracks are observed to propagate stably through about 40% of the specimen before the anti-wing cracks initiate, see Figure 33e). Both the anti-wing cracks initiate at the applied load of 141 MPa, in the stress concentration areas when the tensile stress reaches 20 MPa. The tensile stress concentration area on the right side of the top wing crack (and left side of the bottom wing crack) are about 15-16 MPa in both the models when the anti-wing cracks initiate, and they increase to above 20 MPa as the anti-wing and wing cracks propagate fully through the specimen. As mentioned in section 4.1.1, a small crack is initiated at the right side of the top wing crack in the CZM model, while no cracks are initiated in these areas in the LEFM model. The wing crack initiation angle, θ_0, is measured to be 86° in both the CZM and LEFM model for the 45-degree flaw, see Figure 33b) and e) and Figure 41.

In the 60-degree models, the wing cracks propagate stably through about 40% and 15% of the specimen in the CZM and LEFM models, respectively, before the anti-wing cracks initiate. The applied load is 139 MPa when both the anti-wing cracks initiate in the CZM model, even though only the top anti-wing crack has initiated in Figure 33c). In the LEFM model, the top anti-wing crack initiates when the applied load reaches 158.5 MPa, as is shown in Figure 33f), while the bottom anti-wing crack does not initiate until the applied stress has reached 160.3 MPa. The anti-wing cracks initiate in the stress concentration area to the left of the top wing crack and to the right of the bottom wing crack, in both the CZM and LEFM model. In both the CZM and LEFM model a continuous stress concentration area is observed to move from the top wing crack tip down to the right pre-existing flaw tip. The same is observed from the bottom wing crack in both the models. The stress concentrations in the areas closest to the pre-existing flaw tips reaches above 20 MPa just as the loading is complete, but no new cracks are initiated, as the top and bottom wing cracks still occupy the crack domains in the models. The wing crack initiation angle, θ_0, is 65° in the CZM model, while it is 61° in the LEFM model, see Figure 33c) and f) and Figure 41.

Figure 33 Wing crack propagation, anti-wing crack initiation and the wing crack initiation angle, θ_0, for the different pre-existing flaw inclination angles. Same legend as Figure 28. Top of the Figure is the top of the specimen. ***a)****,* ***b)*** *and* ***c)*** *30-, 45- and 60-degree CZM models, respectively.* ***d)****,* ***e)*** *and* ***f)*** *30-, 45- and 60-degree LEFM models, respectively.*

The anti-wing cracks initiate and propagate in a sub-vertical direction in all models, normal to the tensile stress direction in their respective initiation areas. In all models the anti-wing cracks are also observed to propagate more vertically, i.e., in the direction of the applied load, as they reach the end of the specimen, see Figures 31 and 34. In the CZM models, the part of the anti-wing crack propagating towards the pre-existing flaw is observed to curve slightly towards the pre-existing flaw tip (see Figure 34a), b) and c)), but to never coalesce with the flaw tip. Both the anti-wing cracks are also observed to propagate fully through the specimen for the CZM models. In the 30-degree LEFM model, the bottom crack tip of the top anti-wing crack propagates in a vertical direction straight past the pre-existing flaw tip, until it reaches the end (bottom) of its crack domain, see Figure 34d). The same is observed for the bottom anti-wing crack. For the 45-degree LEFM model, the anti-wing cracks propagate vertically straight past the pre-existing flaw tips, see Figure 34e), but the left anti-wing crack curves just as it surpasses the pre-existing flaw tip. For the 60-degree LEFM model, only the top anti-wing crack propagates past the pre-existing flaw tip, while the bottom anti-wing crack stops propagating a small distance ahead of the pre-existing flaw tip, see Figure 34f). The full crack development in all the models at the final loading stage is shown in Figure 31, while the progressive crack development is shown in the stress-strain curves in Figures 35-38 (the figures are also presented in the Appendix).

Stress does also build up on the right side of the top wing crack, and on the left side of the bottom wing crack in all models, see Figures 33 and 34. As mentioned, these areas are generally a part of the stress field around the wing crack tip, like in Figure 33c) and f), and become individual stress concentration areas as the wing crack propagates. In the 30-degree models, the tensile stress concentrations in these areas increase to about 17 MPa before the anti-wing cracks initiate, and after this they increase up to values of about 60 MPa. The 45-degree models also reach 17 MPa tensile stress in these areas before the anti-wing cracks initiate, after this the stress concentrations increase up to about 40 and 30 MPa in the CZM and LEFM model, respectively. Both the CZM and LEFM models for the 60-degree specimen reach a stress concentration of 20 MPa just as the anti-wing cracks initiate, which progressively increases to a maximum of 25 MPa as load is further applied. Initially, no new cracks are initiated in these areas in the models since the crack domains in which these stress concentration areas belong are still occupied by the wing cracks. In the models where the wing cracks propagate fully through the specimen, and thereby fully through their respective crack domains, small cracks are nucleated, see Figure 31a)-d).

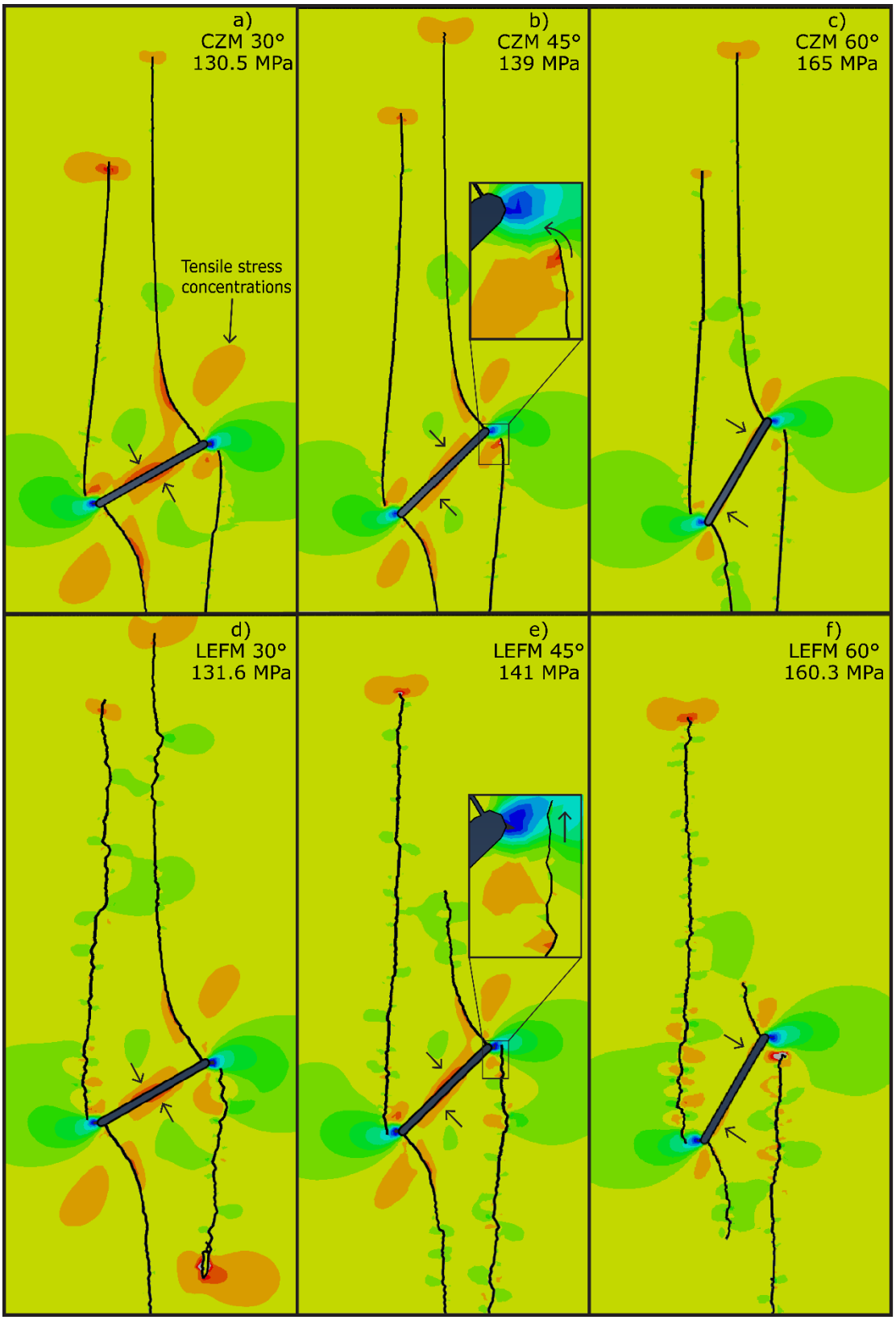

Figure 34 Wing and anti-wing crack propagation for all the models, with arrows at some of the most distinct stress concentration areas. Same legend as Figure 28. Top of the figure is the top of the specimen. ***a)****,* ***b)*** *and* ***c)*** *30-, 45- and 60-degree CZM models, respectively.* ***d)****,* ***e)*** *and* ***f)*** *30-, 45- and 60-degree LEFM models, respectively.*

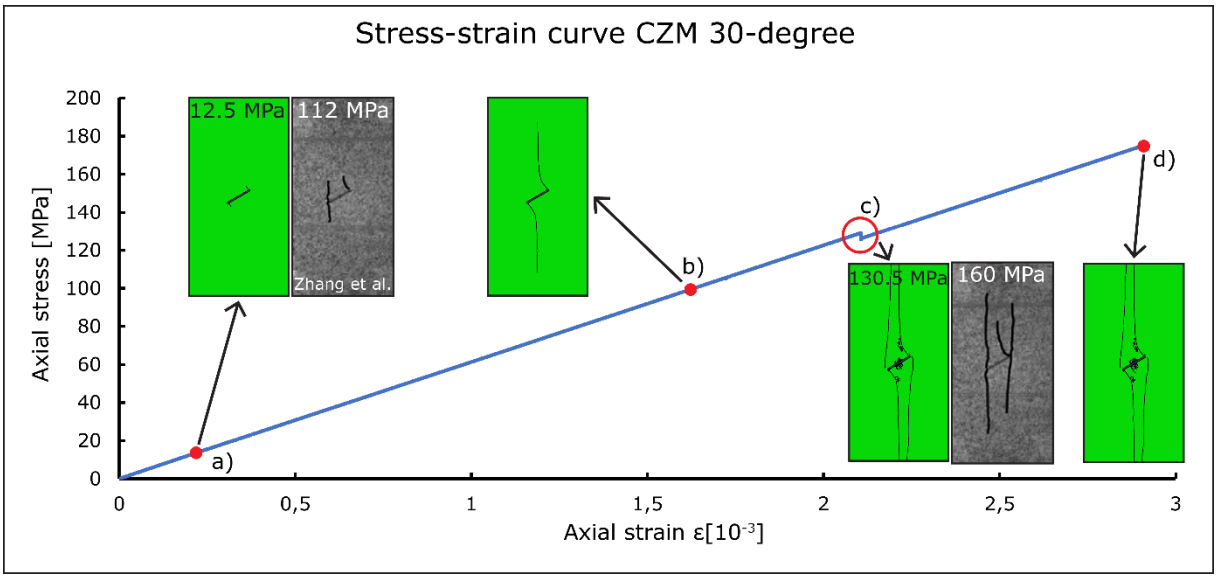

*Figure 35 Stress-strain curve for the 30-degree CZM model, with crack development and comparison to results by Zhang et al. (2021). Stable wing crack growth from **a)** through **b)** and to **c)**, then unstable/rapid wing and anti-wing crack growth in **c)**, and lastly full development in **d)**. The figure is also presented in the Appendix.*

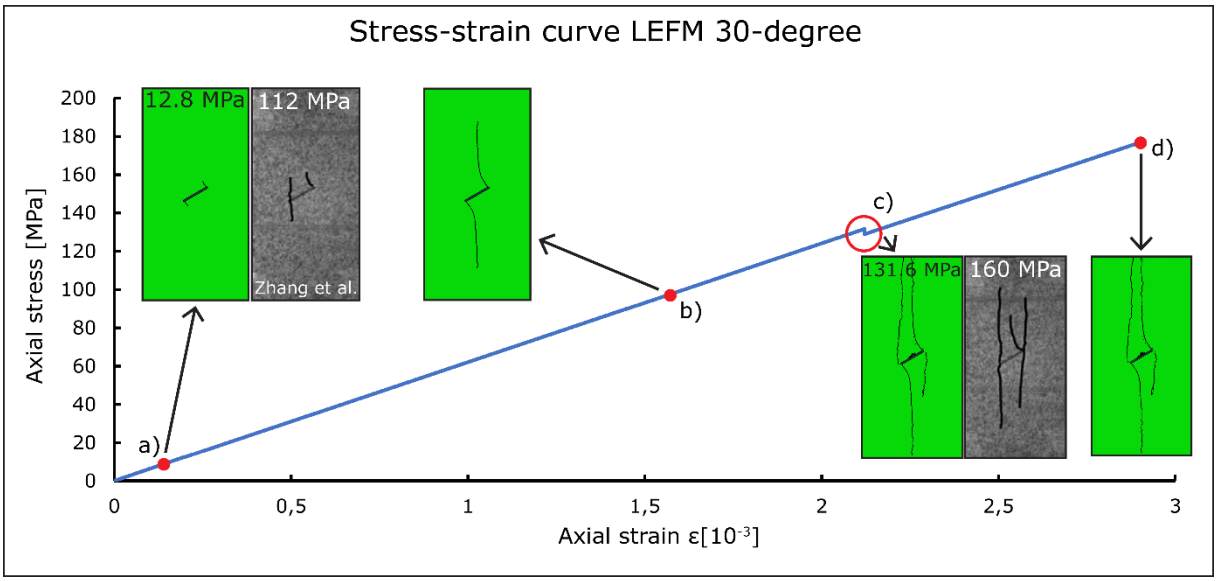

*Figure 36 Stress-strain curve for the 30-degree LEFM model, with crack development and comparison to results by Zhang et al. (2021). Stable wing crack growth from **a)** through **b)** and to **c)**, then unstable/rapid wing and anti-wing crack growth in **c)**, and lastly full development in **d)**. The figure is also presented in the Appendix.*

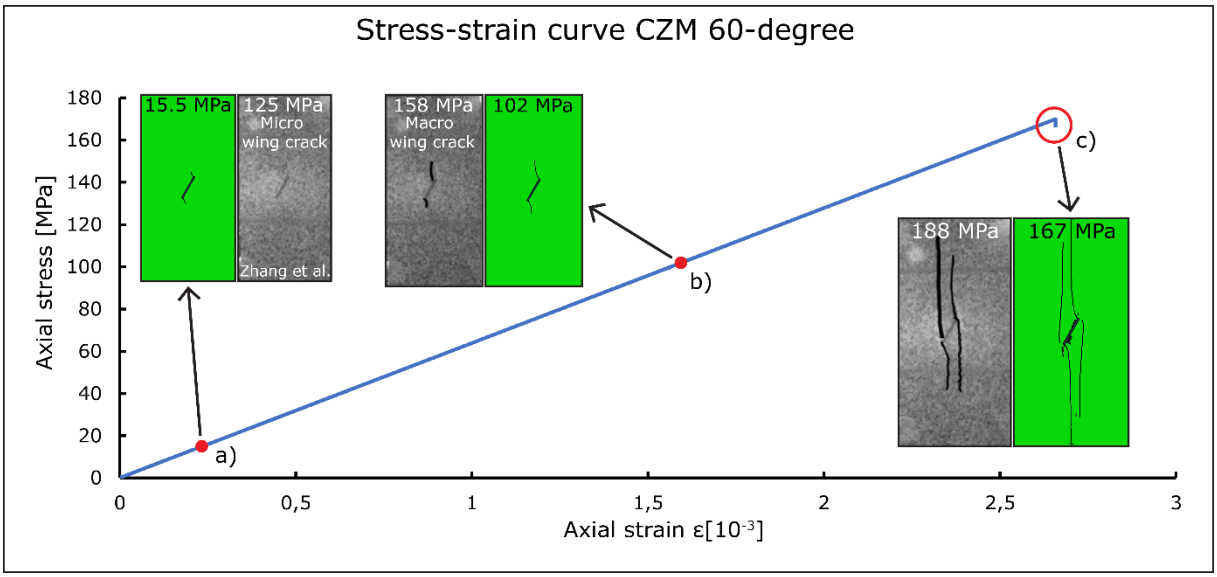

*Figure 37 Stress-strain curve for the 60-degree CZM model, with crack development and comparison to results by Zhang et al. (2021). Stable wing crack growth from **a)** through **b)** and to **c)**, then unstable/rapid wing and anti-wing crack growth in **c)**. The 60-degree LEFM model did not converge past point **c)**, i.e., it only converged for 1100/1200 steps. The figure is also presented in the Appendix.*

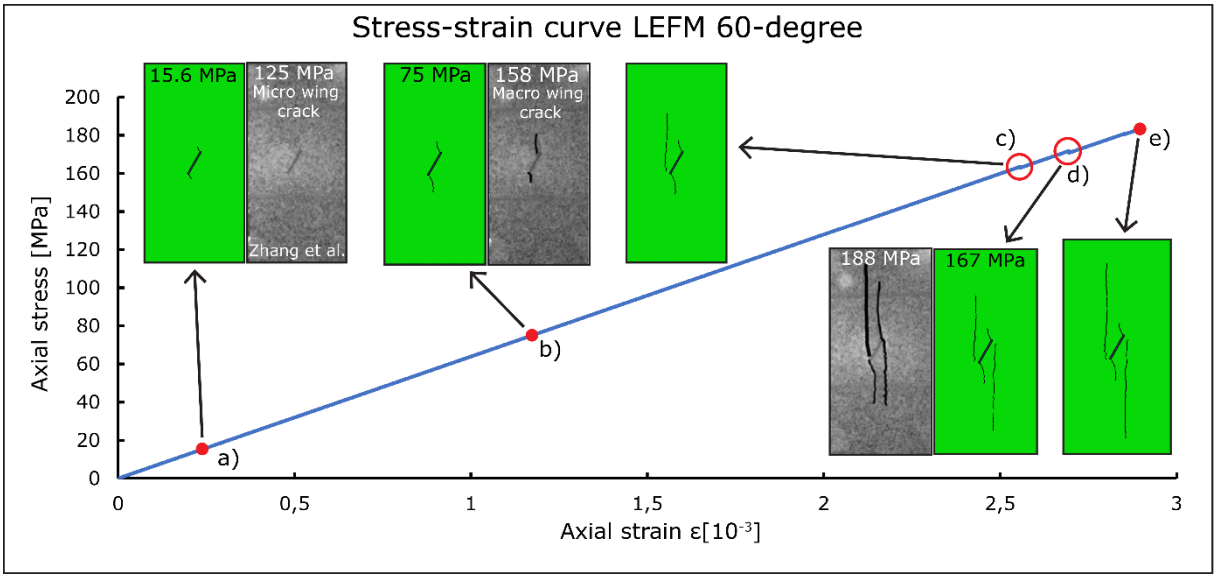

*Figure 38 Stress-strain curve for the 60-degree LEFM model, with crack development and comparison to results by Zhang et al. (2021). Stable wing crack growth from **a)** through **b)** and to **c)**, then unstable/rapid wing and anti-wing crack growth in **c)** and **d)**, and lastly full development in **e)**. The figure is also presented in the Appendix.*

As the anti-wing cracks initiate and propagate, high stress concentrations are observed to form along the long sides of the pre-existing flaw, in all the models, see Figure 34. These stress concentrations increase very rapidly after the initiation of the anti-wing cracks, which is clearly captured by monitoring the stress in selected elements at the vicinity of the pre-existing flaw, see Figure 39. In the 30-degree models, the stress concentrations arise approximately in the middle of the pre-existing flaw, and they are somewhat shifted towards their respective anti-wing crack, i.e., the stress concentrations at the top side of the pre-existing flaw are shifted somewhat towards the left, and the stress concentrations at the bottom side is shifted somewhat to the right. For the 45- and 60-degree models the stress concentrations are observed to shift even further towards the pre-existing flaw tips, in a direction away from their respective anti-wing crack, i.e., further to the right for the top side concentrations, and further to the left for the bottom side concentrations, see Figure 39a)-c). The values and extent of these stress concentrations vary based on the inclination angle, but as mentioned they all appear at the same relative time, i.e., when the anti-wing cracks initiate and propagate. In Figure 39 it is shown how the stress concentration values differ, and how the location of the stress concentration area varies based on the inclination angle.

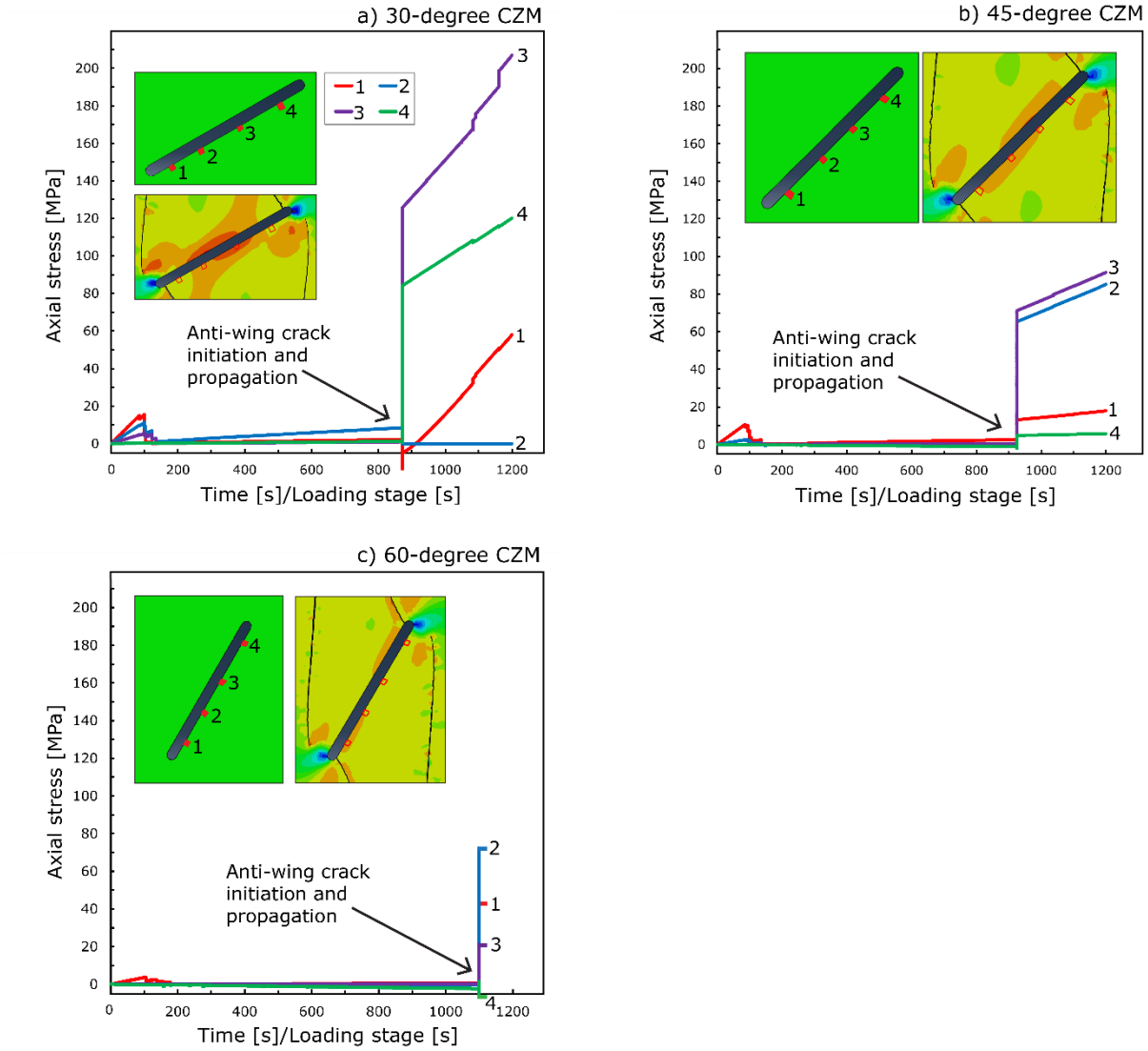

Figure 39 Stress concentrations on the long sides of the pre-existing flaw. ***a)*** *30-degree CZM model with elements 3 and 4 experiencing the highest stress values.* ***b)*** *45-degree CZM model with elements 2 and 3 experiencing the highest stress values.* ***c)*** *60-degree CZM model with elements 1 and 2 experiencing the highest stress values.*

4.1.3 Comparisons to experimental results

Since the geometry of the specimen and the material properties used in the CZM and LEFM models are similar to the granite specimen used by Zhang et al. (2021), some comparisons are made between the crack developments. Liu et al. (2021) also conducted experiments on granite specimens, but this granite had different material properties and the rock specimen had a slightly different geometry compared to the specimen in the CZM and LEFM models. Comparisons to Zhang et al. (2021) are therefore more reasonable than comparisons to Liu et al. (2021). However, some comparisons to Liu et al. (2021) are still made.

In laboratory work carried out by Zhang et al. (2021) and Liu et al. (2021) wing crack initiation stress were measured to be 3-11 times greater than the wing crack initiation stress observed in the CZM and LEFM models, see Table 3. Zhang et al. (2021) differentiated between micro- and macrocrack initiation in their experiments, with the microcrack initiation stresses being consequently lower than the macrocrack initiation stresses. The wing crack initiation stresses in the CZM and LEFM models are 90% smaller than the macrocrack initiation stresses by Zhang et al. (2021). Mostly type II wing cracks were observed by Zhang et al. (2021), while type I wing cracks were observed by Liu et al. (2021) and in the CZM and LEFM models. As for both the CZM and LEFM models, the wing cracks are observed to initiate from the pre-existing flaw tips in Zhang et al. (2021) and Liu et al. (2021), and this is also the case in experimental and numerical studies done by Wang et al. (2020). The type II wing cracks observed in Zhang et al. (2021) may be interpreted to initiate and propagate in conjunction with the stress concentration areas shown in Figure 34. All the wing crack initiation stresses for the different pre-existing flaw inclination angles are compared in Figure 40. The initiation of type IV cracks are observed in Zhang et al. (2021) for the 0-degree granite specimen and for several inclination angles in the gypsum specimens, this type of cracks may agree with the stress concentrations described in Figure 39.

The anti-wing crack initiation stress were also measured by Zhang et al. (2021) and Liu et al. (2021), and these values do not deviate as much as for the wing crack initiation stress values. On average the anti-wing crack initiation stress in the CZM and LEFM models are 19% lower than the stresses from Zhang et al. (2021) and 29% higher than the stresses from Liu et al. (2021). Again, it is important to note that the elastic modulus and Poisson's ratio used in the CZM and LEFM models are the same as the intact elastic modulus for the granite specimens used by Zhang et al. (2021) (62 Gpa and 0.22, respectively), as well as the geometry is the same, while the values of the intact elastic modulus and Poisson's ratio for the granite specimens are not described by Liu et al. (2021). All the anti-wing crack initiation stresses for the different pre-existing flaw inclination angles are shown in Table 3 and Figure 40, and it is evident that the increase in inclination angle also increases both the anti-wing and wing crack initiation stresses.

In the CZM and LEFM models, it is observed that all the anti-wing cracks initiate in stress concentration areas some distance from the pre-existing flaw tip, see Figure 33. This is also indicated in Wang et al. (2020), in the form of white patches (microcracks) nucleating in about the same area as in the CZM and LEFM models, and later turning into macrocracks that coalesce with the pre-existing flaw tip. In Zhang et al. (2021) and Liu et al. (2021), it is not clear where the anti-wing cracks initiate, but they do coalesce with the pre-existing flaw tips. In the CZM and LEFM models, however, this coalescence between the anti-wing crack and the pre-existing flaw is not observed, which can be seen in Figure 31. The anti-wing cracks in Zhang et al. (2021) are also observed to both curve and not to curve towards the pre-existing flaw tips. The stress-strain curves for the CZM and LEFM models showing the development of the anti-wing and wing cracks are shown in Figures 29, 30 and 35-38, together with the crack development observed by Zhang et al. (2021).

The wing crack initiation angles are measured in experimental specimens by Lin et al. (2019) and Wang et al. (2020), and they are observed to decrease with increasing pre-existing flaw inclination angle. The same is observed in the CZM and LEFM models, and in numerical simulation done by Sharafisafa and Nazem (2014). All these results are shown in Table 3 and Figure 41, together with the analytical solution for wing crack inclination angle from Eq. 31. The values from Sharafisafa and Nazem (2014) are measured from

their numerical simulations of a pre-existing open flaw with a tapered tip (the tip gets smaller towards the ends of the flaw). The wing crack initiation angles are not measured in Zhang et al. (2021), but with several of the wing cracks being classified as type II, the wing cracks seem to propagate in an almost vertical direction after they initiate.

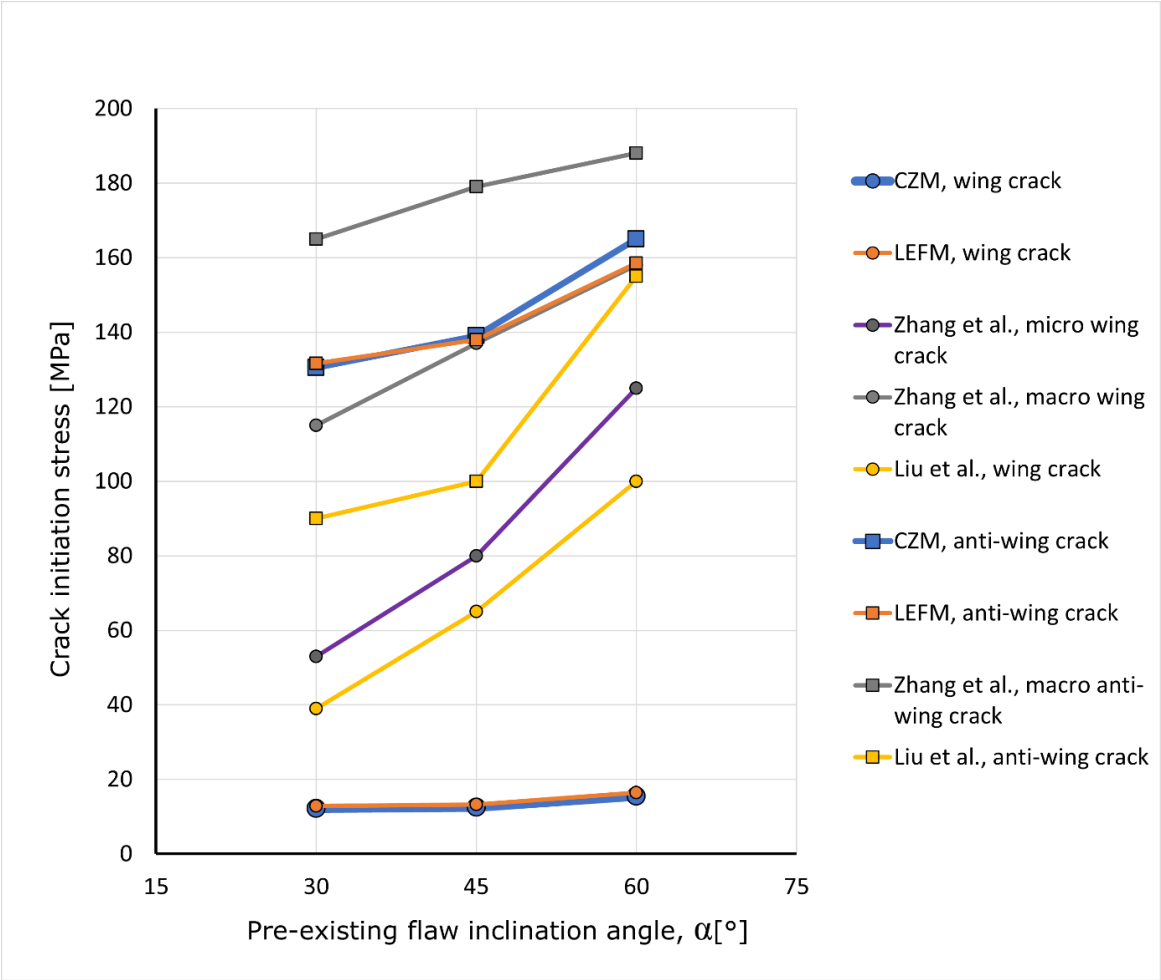

Figure 40 Comparisons between the CZM and LEFM models to experimental results obtained by Zhang et al. (2021) and Liu et al. (2021). The specimens used in Zhang et al. (2021) have the same geometry and elastic material properties as the CZM and LEFM models, while the specimens used in Liu et al. (2021) only somewhat resemble the CZM and LEFM models.

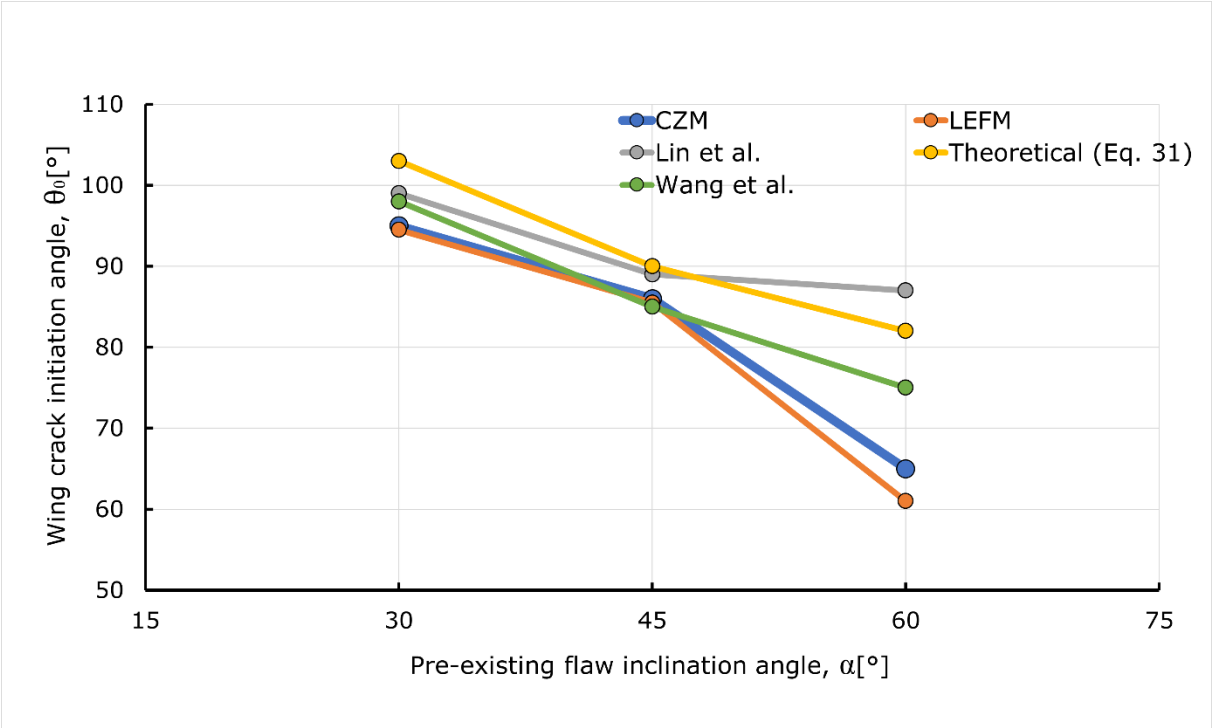

Figure 41 Wing crack initiation angle, θ_0, for different inclination angles from the CZM and LEFM models, as well as from the analytical solution and results obtained in experiments by Lin et al. (2019) and Wang et al. (2020).

Table 3 Initiation stress for both the wing and anti-wing cracks and initiation angles for the wing cracks from the CZM and LEFM models, the analytical solution and from experimental results obtained by Sharafisafa and Nazem (2014), Lin et al. (2019), Wang et al. (2020), Liu et al. (2021) and Zhang et al. (2021).

	CZM	**LEFM**	**Theo-retical Eq. 31**	**Zhang et al. (micro-/ macro-crack)**	**Liu et al.**	**Lin et al.**	**Wang et al.**	**Sharafisafa and Nazem (XFEM/DEM)**
Initiation stress, wing crack [MPa]								
30	12.2	12.4	-	53 / 114	39	-	-	-
45	12.5	12.9	-	80 / 137	65	-	-	-
60	15.5	15.6	-	125 / 158	100	-	-	-
Initiation stress, anti-wing crack [MPa]								
30	130.5	131.6	-	- / 165	90	-	-	-
45	139	138	-	- / 170	100	-	-	-
60	165	158.5	-	- / 188	155		-	-
Wing crack initiation angle, θ_0 [°]								
30	95	95	103	-	-	99	98	~62/~ 57
45	86	86	90	-	-	89	85	~62/~ 52
60	65	61	82	-	-	87	75	~44 /~ 47

4.2 Relative displacements across the wing and anti-wing cracks

The relative normal and shear displacements across the top wing and anti-wing crack are in this section monitored. These displacements are interesting as they describe how the cracks open/close and shear as they initiate and as they propagate. How the cracks affect each other as they grow may also be captured by monitoring the relative displacements.

4.2.1 Wing crack

The relative displacement between two nodes on opposite sides of a crack can be used to determine the crack initiation mechanism, i.e., tensile, shear or a mix of the two. In the following results, the coordinate system used to define normal and shear displacement is defined as in Figure 42. It is important to note that the line between P and P' is the approximate normal to the crack, and the relative displacement results may therefore not be the exact normal and shear displacement values, but they are assumed to give reasonable indications of what happens across the wing crack close to the pre-existing open flaw tip.

The distances between P and P' in the 30-, 45- and 60-degree CZM models are 1, 0.5 and 0.6 mm, and they are located 2, 1.5 and 2 mm radially from the pre-existing flaw tip, respectively. The distances between P and P' in the 30-, 45- and 60-degree LEFM models are 1, 0.6 and 1 mm, and they are located 2 mm radially from the pre-existing flaw tip, respectively.

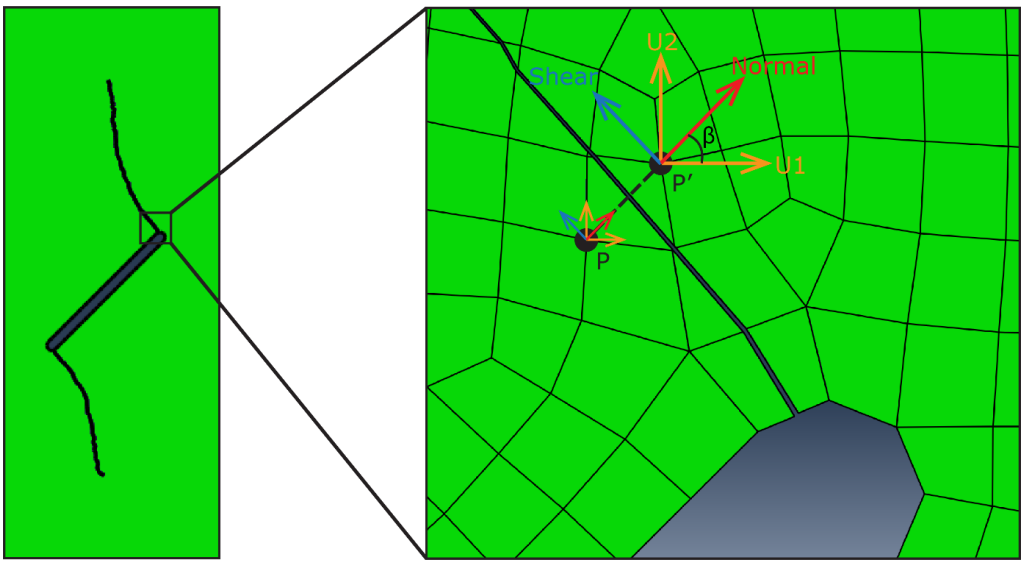

Figure 42 The nodes P and P' from the 45-degree CZM model used to calculate the relative normal and shear displacements across the top wing crack. Similar node locations are used for the 30- and 60-degree models.

30-degree top wing crack

In the 30-degree CZM model, the relative normal displacement increases abruptly just as the top wing crack initiates and propagates between P and P', this happens after 110 s and the displacement reaches a value of 0.002 mm. After this, it starts to increase approximately linearly. In the almost linear part between the wing crack and anti-wing crack initiations, the relative normal displacement occasionally increases with small distinct displacement jumps, e.g., after 270, 360 and 590 s. These small displacement jumps are at loading stages where the top wing crack propagates short distances, but very rapidly. The linear parts of the graph indicate stable wing crack growth. The relative normal displacement decreases miniscule just as the top anti-wing crack initiates, due to a small closing of the crack, before it increases again when the top wing crack have propagated though the whole specimen, this happens after about 872 s. After both the wing and anti-wing cracks have propagated through the whole specimen, the relative normal displacement increases linearly again, see Figure 43a). The relative shear displacement increases linearly from the loading begins and until the top wing crack initiates. The relative shear displacement fluctuates somewhat as the top wing crack initiates, and has an overall increase (sinistral shear), before it starts to decrease (dextral shear) almost linearly after about 125 s. After 872 s, the relative shear displacement first decreases due to some propagation of the bottom anti-wing crack (dextral shear), then increases due to the propagation of the top anti-wing crack (sinistral shear) and lastly decreases again (dextral shear) as the top wing and anti-wing crack reaches the top of the specimen, see Figure 43a). The relative shear displacement is held almost constant as the rest of the load is applied. The relative normal and shear displacement across the top wing crack in the 30-degree CZM model is shown in Figure 44a)-d).

As for the CZM model, the relative normal and shear displacement in the LEFM model increases slightly in a linear fashion from the loading is applied to the top wing crack initiates, the shear is positive (sinistral). As the top wing crack initiates after 83 s and propagates between node P and P', the relative normal displacement increases almost instantly to the value of about 0.005 mm. The relative normal displacement then increases linearly until the top anti-wing crack initiates, with small distinct displacement jumps after 230 and 600 s, indicating small abrupt openings of the top wing crack. The relative shear displacement decreases abruptly as the top wing crack initiates, with a negative (dextral) shear sense. It then continues to decrease with small distinct negative (dextral) shear displacement at the same times as the small distinct relative normal displacements, indicating that negative shearing occurs together with the small crack openings, see Figure 43b). When the top anti-wing crack initiates after 878 s, the relative normal displacement decreases slightly together with an increase in the relative shear displacement (sinistral shear), indicating a closing of the crack together with positive (sinistral) shearing before the crack opens again together with a small negative (dextral) shearing. After both the top wing and anti-wing crack have propagated fully through the specimen, the relative normal displacement increases linearly, while the relative shear displacement is held constant. The relative normal and shear displacement across the top wing crack in the 30-degree LEFM model is shown in Figure 44e)-h).

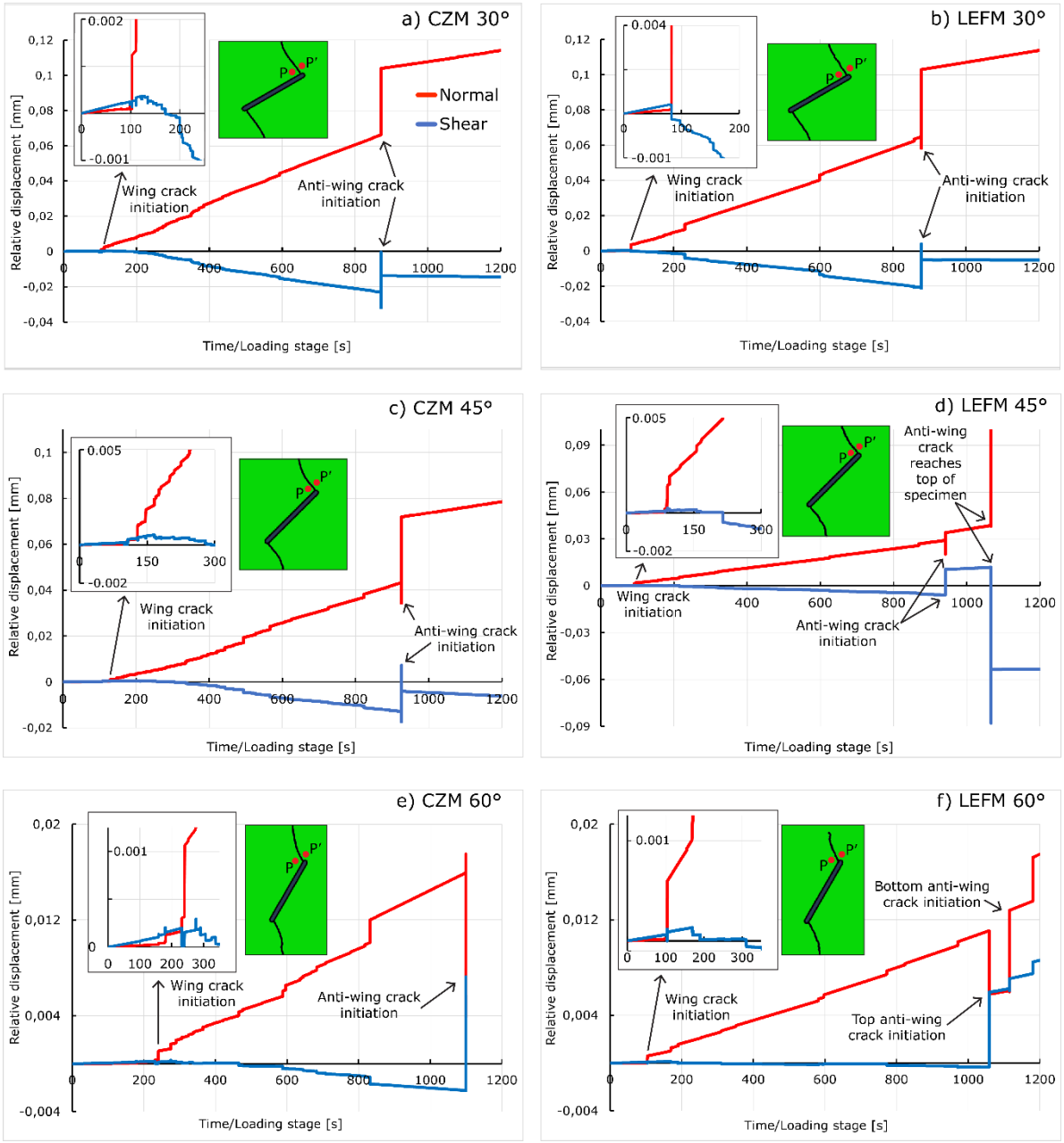

Figure 43 Relative normal and shear displacement between the two nodes P and P' in the top wing cracks. Positive normal and shear slopes indicate opening and positive (sinistral) shear, while negative normal and shear slopes indicate closing and negative (dextral) shear, respectively. ***a)*** *30-degree CZM model.* ***b)*** *30-degree LEFM model.* ***c)*** *45-degree CZM model.* ***d)*** *45-dergee LEFM model. The relative normal displacement reaches a value of 0.45 mm after 1067 s, before it decreases down to 0.25 mm.* ***e)*** *60-dergee CZM model. This model did not converge after 1100 s.* ***f)*** *60-degree LEFM model.*

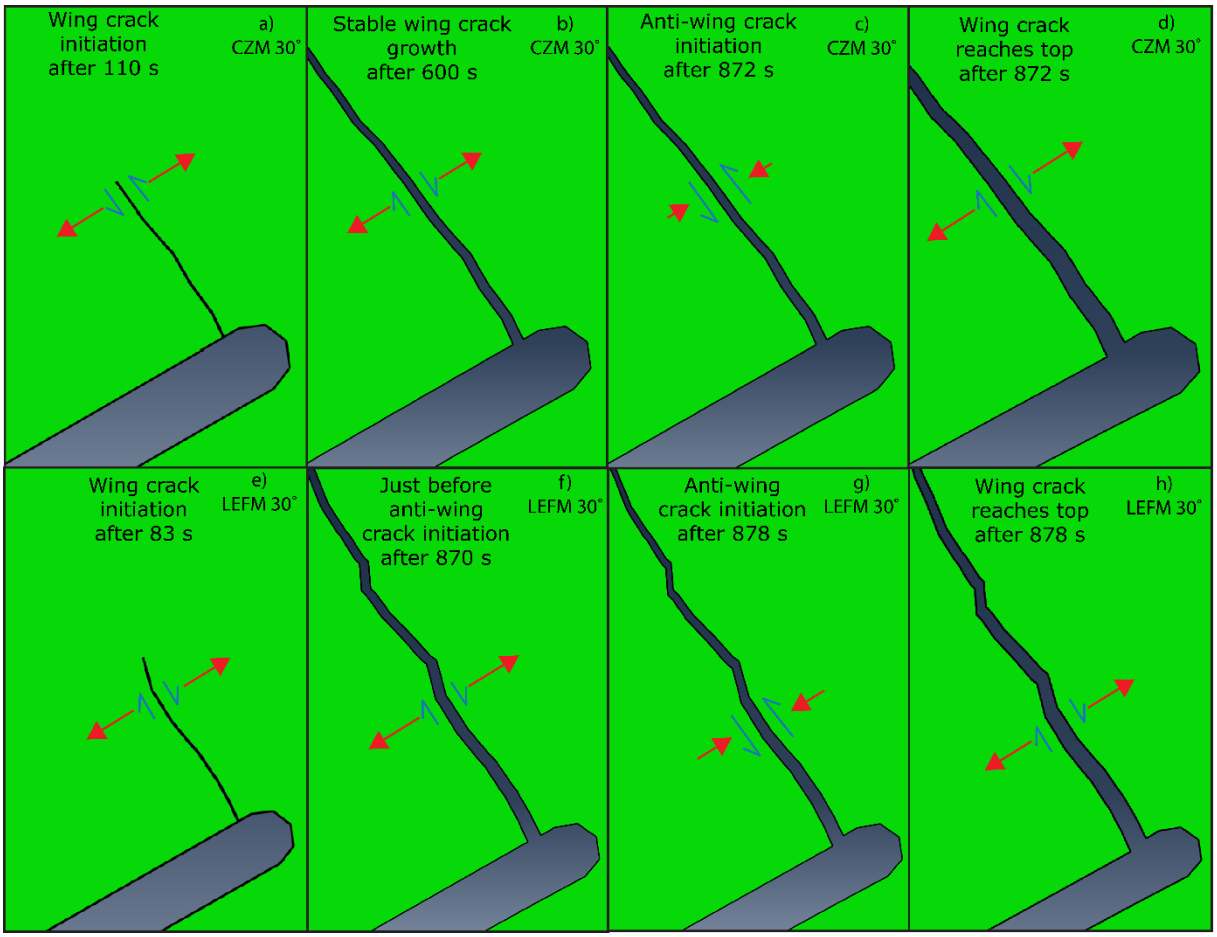

Figure 44 Normal and shear displacement across the top wing crack for the 30-degree CZM and LEFM models. The arrows are not to scale. Scale factor = 3. ***a)*** *Normal and shear displacements as the top wing crack initiates and propagates between P and P' after 110 s in the CZM model (17 MPa applied load).* ***b)*** *Increasing relative normal displacement due to stable and occasionally rapid wing crack growth after 600 s in the CZM model (90 MPa applied load).* ***c)*** *Miniscule closing of the top wing crack combined with positive shearing as the top anti-wing crack initiates after 872 s (130.5 MPa applied load).* ***d)*** *Opening of the wing crack as the wing crack propagates through the whole specimen after 872 s (130.5 MPa applied load).* ***e)*** *Normal and shear displacements as the top wing crack initiates and propagates between node P and P' after 83 s in the LEFM model (12.4 MPa applied load).* ***f)*** *Development of the top wing crack due to stable and occasionally rapid wing crack growth after 870 s (130 MPa applied load).* ***g)*** *Closing of the top wing crack combined with positive shearing as the top anti-wing crack initiates after 878 s (131.6 MPa applied load).* ***h)*** *Opening of the wing crack as the wing crack propagates through the whole specimen after 878 s (131.6 MPa applied load).*

45-degree flaw wing crack

In the CZM model both the relative normal and shear displacements are almost negligible until the top wing crack initiates. As the top wing crack initiates, the relative normal displacement increases abruptly, see Figure 43c). The relative normal displacement continues to increase almost linearly as more load is applied, with small distinct jumps in displacements as the top wing crack propagates rapidly short distances, indicating small abrupt openings of the crack. The most distinct of these small displacement jumps happen

after 493, 567, 725 and 823 s. The relative shear displacement as the top wing crack initiates increases slightly and has a positive (sinistral) shear sense. The relative shear displacement starts to decrease, negative (dextral) shear motion, after the top wing crack initiation, and reaches negative values after about 300 s. It continues to decrease almost linearly with small distinct negative shear displacement jumps at the same times as for the small relative normal displacement jumps. After the initiation of the top anti-wing crack, the relative normal displacement decreases instantly, which indicates a small closing of the top wing crack, before it increases abruptly and opens, as it together with the anti-wing crack propagates through the whole specimen. The relative shear displacement decreases abruptly with a negative (dextral) shear motion when the bottom anti-wing crack initiates and propagates, before it increases abruptly with a positive (sinistral) shear motion as the top anti-wing crack initiates, before it again decreases in a negative (dextral) shear motion and continues to decrease linearly as the rest of the load is applied. The relative normal and shear displacement across the top wing crack in the 45-degree CZM model is shown in Figure 45a)-d).

The relative normal and shear displacements in the LEFM model are also negligible before the top wing crack initiates and propagates. When the top wing crack initiates and propagates between node P and P' after 86 s, the relative normal displacement increases almost instantly, reaching a value of about 0.002 mm, before it continues to increase in a linear fashion. The relative shear displacement increases minuscule as the top wing crack initiates, reaching a value of 0.0003 mm, with the shear motion being positive (sinistral), see Figure 43d). The relative normal displacement increases linearly up until 942 s, with very small distinct displacement jumps after 215, 320, 626 and 869 s, indicating small openings of the crack as it propagates shortly and rapidly. The relative shear displacement starts to decrease after the top wing crack initiation, with the shear motion being negative (dextral), reaching negative shear displacement values after about 220 s. The relative shear displacement decreases almost linearly with small distinct negative (dextral) shear motions at the same times as the distinct small relative normal displacement jumps. When the loading reaches 942 s, the top anti-wing crack initiates, and the relative normal and shear displacements respectively decreases and increases almost instantly. The relative shear motion at this time is positive (sinistral), while the decrease in relative normal displacement indicates a closing of the crack. The top wing crack opens again after some propagation of the top anti-wing crack. Further, both the relative normal and shear displacement increases slightly and linearly until the top anti-wing crack reaches the top of the specimen. When the top-anti wing crack reaches the top of the specimen the relative normal displacement increases almost instantly to a value of 0.45 mm before it quickly decreases to 0.25 mm due to the initiation and propagation of the crack in the middle of the pre-existing flaw (this crack is seen in Figure 31e). The relative shear displacement decreases abruptly as the top anti-wing crack reaches the top of the specimen, with a negative (dextral) shear sense before it increases abruptly in a positive (sinistral) shear sense when the crack in the middle of the pre-existing flaw initiates and propagates. The relative normal and shear displacement across the top wing crack in the 45-degree LEFM model is shown in Figure 43e)-h). The top wing crack does not reach the top of the specimen in this model.

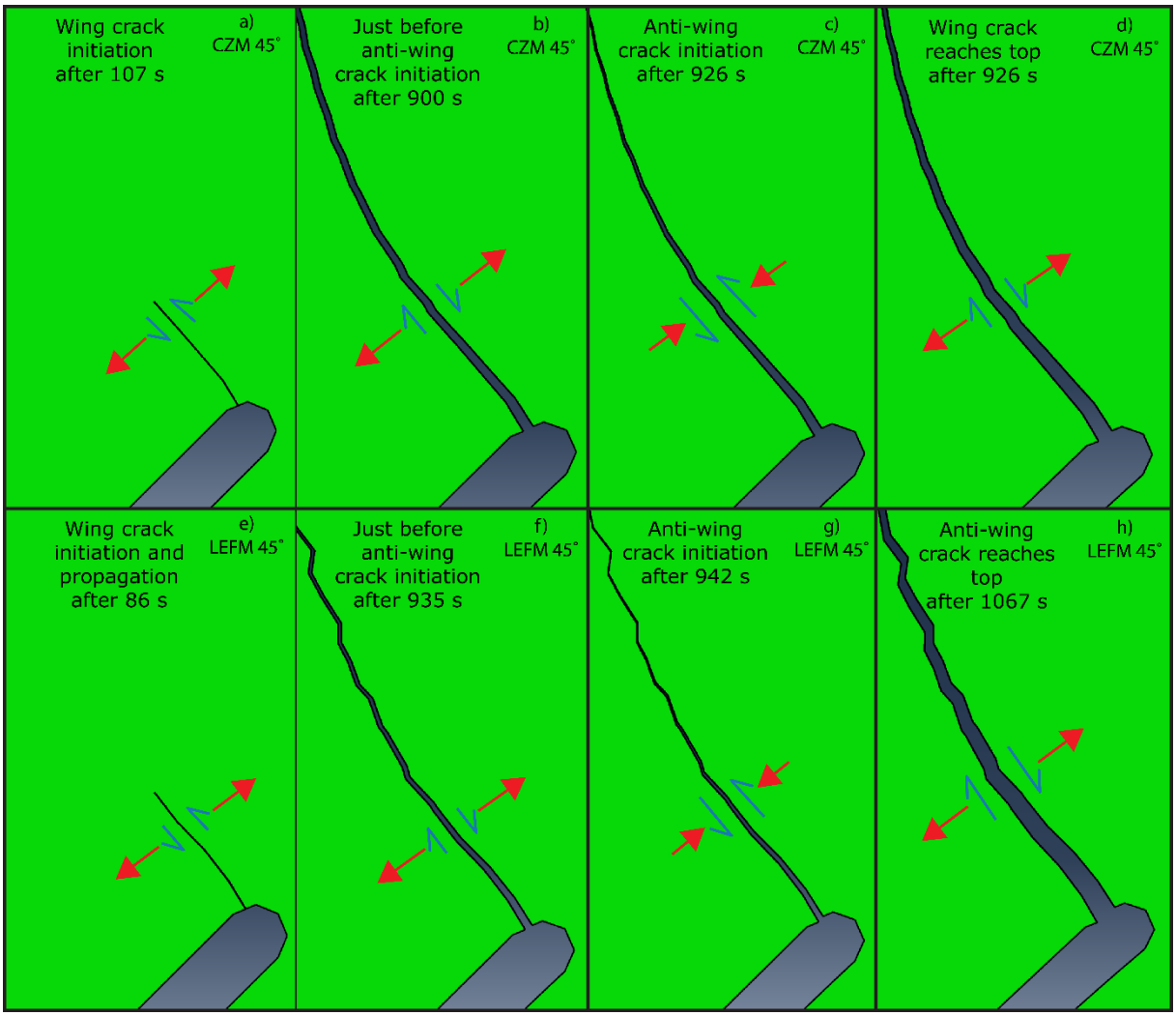

Figure 45 Normal and shear displacement across the top wing crack for the 45-degree CZM and LEFM models. The arrows are not to scale. Scale factor = 3. ***a)*** *Normal and shear displacements as the top wing crack initiates and propagates after 107 s in the CZM model (16 MPa applied load).* ***b)*** *Increasing normal displacement and negative shearing due to stable and occasionally rapid wing crack growth after 900 s in the CZM model (135 MPa applied load).* ***c)*** *Closing of the top wing crack and positive shearing as the top anti-wing crack initiates and propagates after 926 s in the CZM model (139 MPa applied load).* ***d)*** *Increasing normal displacement and negative shearing due to new opening of the wing crack as the anti-wing crack propagates through the whole specimen.* ***e)*** *Normal and shear displacements as the top wing crack initiates after 86 s in the LEFM model (13 MPa applied load).* ***f)*** *Development of the top wing crack due to stable and occasionally rapid wing crack growth after 935 s (140 MPa applied load).* ***g)*** *Closing of the top wing crack and positive shearing as the top anti-wing crack initiates after 942 s (141 MPa applied load). This is followed by a new opening again shortly after.* ***h)*** *Opening of the top wing crack as the top anti-wing crack propagates through the whole specimen after 1067 s (160 MPa applied load). Further, the bottom anti-wing crack reaches the bottom of the specimen, and the relative normal displacement increases even more combined with a positive shear motion, followed by a closing of the crack due to initiation and propagation of the crack in the middle of the pre-existing flaw.*

60-degree flaw wing crack

The initiation of the top wing crack after 232 s leads to an almost instant increase in the relative normal displacement, while the relative shear displacement first decreases abruptly with a negative (dextral) shear sense, before it increases abruptly with a positive (sinistral) shear motion, see Figure 43e). The relative normal displacement continues to increase as more load is applied, in a linear fashion, with small distinct displacement jumps at after 470, 590 and 840 s, as the top wing crack propagates shortly but rapidly, leading to distinct openings of the crack. The relative shear displacement shows small distinct negative (dextral) shear displacements at these same times while generally developing in a negative linear fashion. As the top anti-wing crack initiates, the relative normal displacement decreases due to a closing of the top wing crack, this happens together with a positive (sinistral) shear displacement. When the top wing crack reaches the top of the specimen, the relative normal displacement increases again. The relative normal and shear displacements across the top wing crack in the 60-degree CZM model are shown in Figure 46a)-d). The 60-degree CZM model does not converge fully, and no displacement data are available after 1100 s.

In the 60-degree LEFM model, the relative shear displacement increases slightly from the loading starts till the top wing crack initiates. When the top wing crack initiates and propagates between node P and P', the relative shear displacement first decreases abruptly with a negative (dextral) shear motion, before it increases abruptly with a positive (sinistral) shear motion. The relative normal displacement is almost negligible before the initiation of the top wing crack, and after its initiation it increases abruptly, indicating an opening of the top wing crack, see Figure 43f). Small normal displacement jumps are observed after the initiation of the top wing crack and before the initiation of the top anti-wing crack, which represents small openings as the wing crack sometimes propagate shortly and rapidly, e.g., after 170, 590, 770 and 975 s. The relative shear displacement shows small negative (dextral) shear motions at these same times, and is generally held almost constant at 0 mm between 200 and 800 s. After 800 s, the relative shear displacement decreases slightly linearly, in a negative (dextral) shear motion, until the top anti-wing crack initiates. When the top anti-wing crack initiates, the relative normal displacement decreases abruptly, indicating a closing of the crack, while the relative shear displacement increases abruptly in a positive (sinistral) shear sense. Further, as the bottom anti-wing crack initiates and propagates after 1115 s, the relative normal displacement increases abruptly together with the relative shear displacement, the shear motion is positive (sinistral). The increase in the relative normal and shear displacements after 1181 s are due to a new short and rapid propagation of both the top and bottom anti-wing cracks. The shear motion at this point is still positive (sinistral). The relative normal and shear displacements across the top wing crack in the 60-degree LEFM model are shown in Figure 46e)-h).

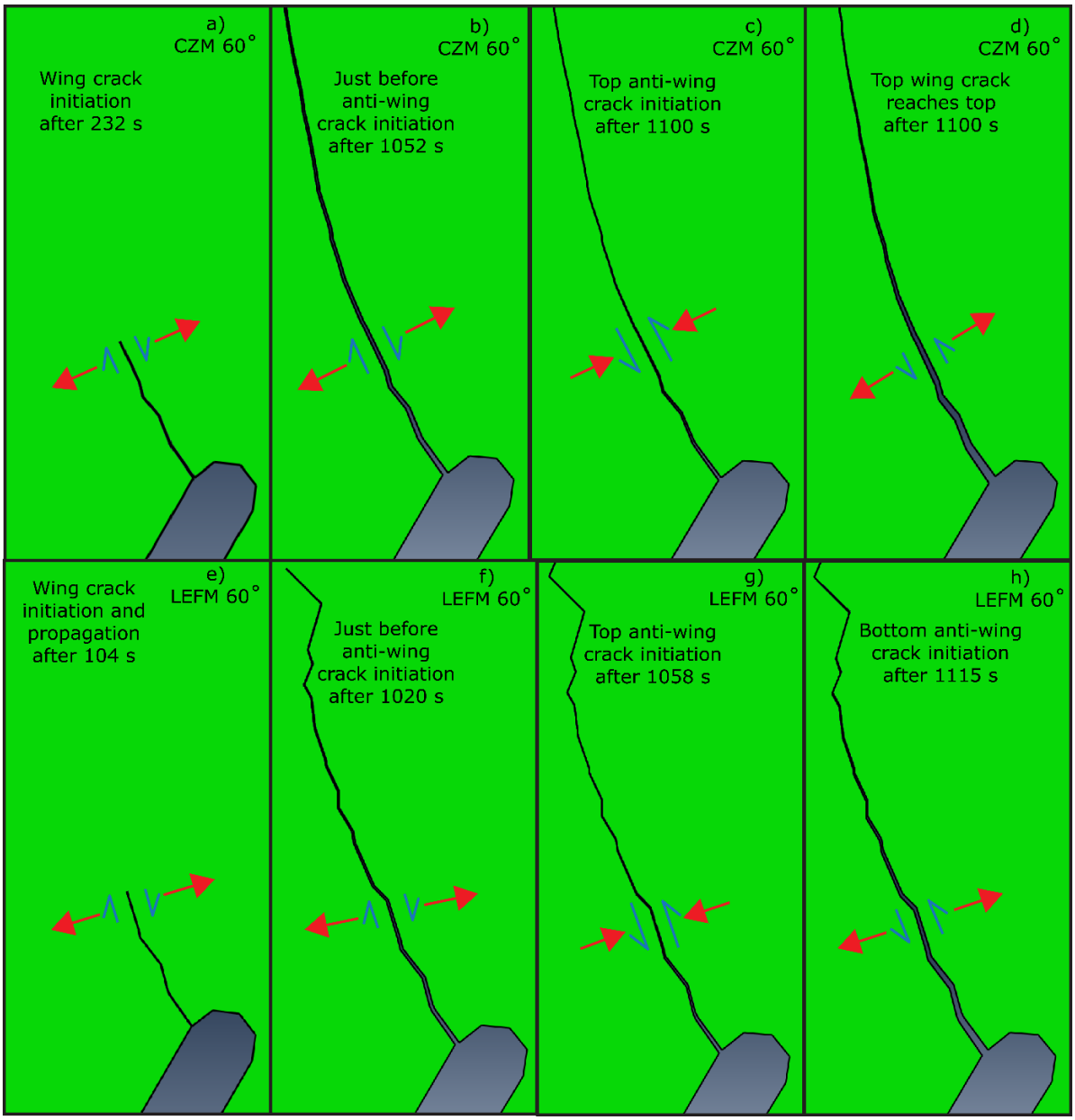

Figure 46 Normal and shear displacement across the top wing crack for the 60-degree CZM and LEFM models. The arrows are not to scale. Scale factor = 3. ***a)*** *Normal and shear displacements as the top wing crack propagates between node P and P' after 232 s in the CZM model (35 MPa applied load). The shear sense is first negative (like in the figure), then positive* ***b)*** *Increasing normal displacement due to stable and occasionally rapid wing crack growth after 1052 s in the CZM model (158 MPa applied load).* ***c)*** *Closing of the top wing crack and positive shearing as the top anti-wing crack initiates and propagates after 1100 s in the CZM model (165 MPa applied load).* ***d)*** *Increasing normal displacement due to new opening of the wing crack as it propagates through the whole specimen.* ***e)*** *Normal and shear displacements as the top wing crack propagates between node P and P' after 104 s in the LEFM model (16 MPa applied load). The shear sense is first negative (like in the figure), then positive.* ***f)*** *Development of the top wing crack due to stable and occasionally rapid wing crack growth causing progressive opening after 1020 s (153 MPa applied load).* ***g)*** *Closing of the top wing crack combined with positive shearing as the top anti-wing crack initiates and propagates after 1058 s (158.5 MPa applied load).* ***h)*** *Opening of the top wing crack and positive shearing as the bottom anti-wing crack initiates and propagates through the whole specimen after 1115 s (167 MPa applied load).*

4.2.2 Anti-wing crack

As for the wing crack, two nodes on the opposite sides of the anti-wing crack are chosen to measure the relative normal and shear displacements across the anti-wing crack, see Figure 47. The two nodes are chosen to be at the location where the anti-wing crack initiates, to capture the relative displacements from initiation to full propagation.

The distances between P and P' in the 30-, 45- and 60-degree CZM models are 0.5, 0.4 and 0.5 mm, and they are located 9, 9 and 7 mm radially from the pre-existing flaw, respectively. The distances between P and P' in the 30-, 45- and 60-degree LEFM models are 0.6, 0.4 and 1 mm, and they are located 10, 9 and 7.6 mm radially from the pre-existing flaw, respectively.

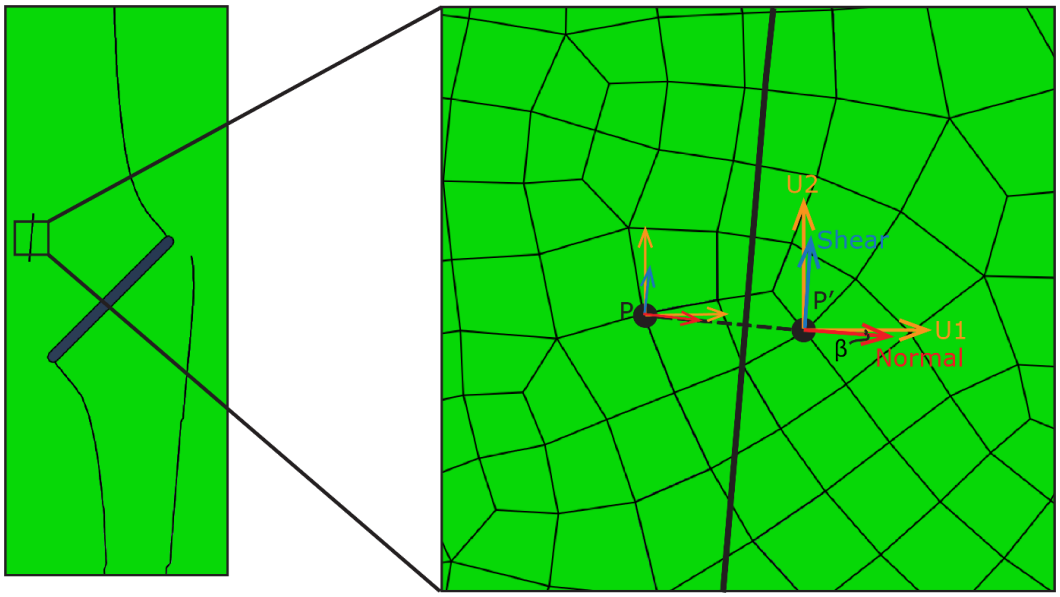

Figure 47 The nodes P and P' from the 45-degree CZM model used to calculate the relative normal and shear displacement across the top anti-wing crack. Similar node locations are used for the other models.

30-degree flaw anti-wing crack (both CZM and LEFM)

As load is applied in the 30-degree CZM model, no momentaneous change in the relative normal or shear displacements are observed, see Figure 48a). From 0 s up until 872 s both the displacements develop linearly due to the load applied, with the shear displacement being negative (dextral), and the normal displacement being positive. When the top anti-wing crack initiates after 872 s, the relative shear displacement first increases slightly, then decreases, before it lastly increases abruptly in a positive shear sense, changing the shear displacement from -0.001 to 0.01 mm. Further, the relative shear displacement stabilizes and is almost constant as the rest of the load is applied. The relative normal displacement increases abruptly as the anti-wing crack initiates, from 0.001 to almost 0.9 mm. The anti-wing crack initiates and propagates fully at 872 s, and the relative normal

displacement continues to increase linearly after this loading point. The relative normal and shear displacements as the wing and anti-wing cracks initiate are shown in Figure 49a) and b).

In the 30-degree LEFM model, the relative normal and shear displacements increase slightly between the first load is applied until the anti-wing crack nucleate after about 878 s, with the shear sense being negative (dextral). Ater the initiation of the top anti-wing crack, the relative normal displacement increases abruptly from 0.001 to almost 0.1 mm, and then starts to increase linearly after the top anti-wing crack reaches the top of the specimen. The relative shear displacement as the top anti-wing crack initiates first increases slightly in a positive (sinistral) shear sense, then decreases slightly in a negative (dextral) shear sense, before it lastly increases in a positive (sinistral) shear sense from -0.0015 to about 0.01 mm. The relative shear displacement is further held almost constant as the rest of the load is applied, see Figure 48b). The relative normal and shear displacements as the wing and anti-wing cracks initiate are shown in Figure 49c) and d).

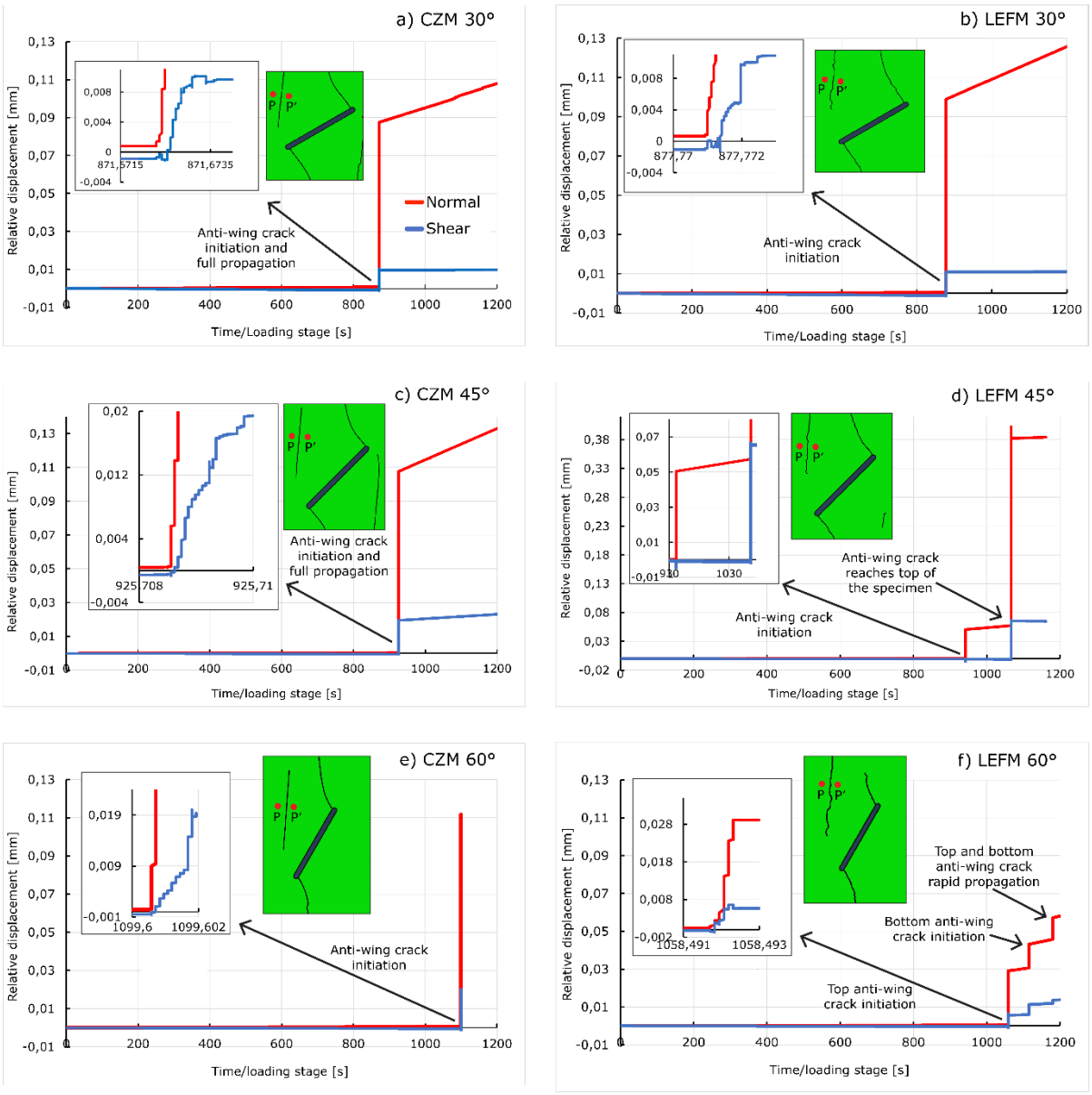

Figure 48 Relative normal and shear displacement between the two nodes P and P' in the top anti-wing cracks. Positive normal and shear slopes indicate opening and positive (sinistral) shear, while negative normal and shear slopes indicate closing and negative (dextral) shear, respectively. ***a)*** *30-degree CZM model.* ***b)*** *30-degree LEFM model.* ***c)*** *45-degree CZM model.* ***d)*** *45-dergee LEFM model.* ***e)*** *60-dergee CZM model. This model did not converge after 1100 s.* ***f)*** *60-degree LEFM model.*

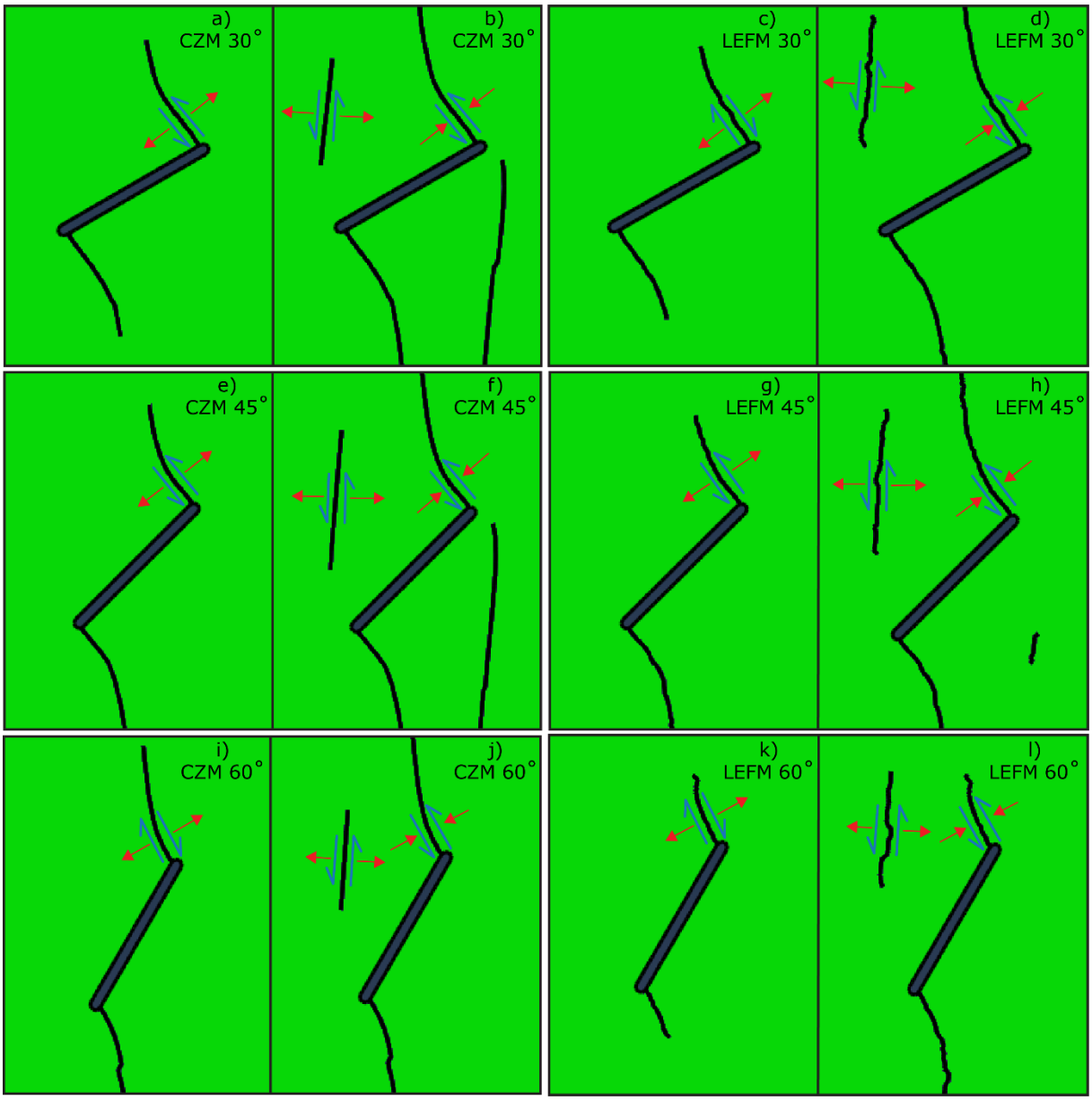

Figure 49 Relative normal and shear displacements at wing and anti-wing crack initiations for all models. The arrows are not to scale. ***a)*** *and* ***b)*** *30-degree CZM model.* ***c)*** *and* ***d)*** *30-degree LEFM model.* ***e)*** *and* ***f)*** *45-degree CZM model.* ***g)*** *and* ***h)*** *45-degree LEFM model.* ***i)*** *and* ***j)*** *60-degree CZM model.* ***k)*** *and* ***l)*** *60-degree LEFM model.*

45-degree flaw anti-wing crack

Little to no relative normal and shear displacements are observed before the initiation of the top anti-wing crack in the CZM model. After the initiation of the top anti-wing crack the relative normal displacement increases almost instantly from 0.0005 to almost 0.11 mm before it continues to increase linearly as the rest of the load is applied. The relative shear displacement has reached a slight negative value before the initiation of the top anti-wing crack and it increases abruptly in a positive shear sense as the anti-wing crack initiates, from 0.0008 to almost 0.02 mm. The relative shear displacement continues to

increase with a positive shear sense after the top anti-wing crack has propagated through the entire specimen, see Figure 48c). The relative normal and shear displacements as the wing and anti-wing cracks initiate are shown in Figure 49e) and f).

As for the CZM model, little to no relative normal and shear displacements are observed before the initiation of the anti-wing crack. After the initiation of the top anti-wing crack the relative normal displacement increases almost instantly and reaches a value of 0.06 mm. After the initiation and some rapid propagation of the top anti-wing, it continues to propagate stably between 942 s and 1067 s. The relative shear displacement decreases abruptly before it increases abruptly again as the top anti-wing crack initiates, seen as a small dent in Figure 48d), and is held almost constant at 0 mm as the crack propagates stably between 942 s and 1067 s. After 1067 s the bottom anti-wing crack initiates and propagates fully through the specimen together with the rest of the top anti-wing crack, and this leads to an increase in both the relative normal and shear displacement, with a positive (sinistral) shear motion, see Figure 48d). The crack in the middle of the pre-existing flaw also initiates at this loading stage, causing a small closing of the top anti-wing crack. The relative normal and shear displacements are held approximately constant as the rest of the load is applied. The relative normal and shear displacements as the wing and anti-wing cracks initiate are shown in Figure 49g) and h).

60-degree flaw anti-wing crack

The relative normal and shear displacements are negligible before the initiation of the top anti-wing crack in the CZM model. When the top anti-wing crack initiates an abrupt and almost immediate increase is observed in both the relative normal and shear displacements, see Figure 48e). Due to non-convergence in the last loading stages in the model, the displacement data after 1100 s were not captured, and it is therefore difficult to interpret the maximum values of the displacements. The relative normal and shear displacements as the wing and anti-wing cracks initiate are shown in Figure 49i) and j).

There is also a negligible amount of relative normal and shear displacement before the anti-wing crack initiation in the LEFM model. As the top anti-wing crack initiates after about 1058 s the relative normal displacement increases abruptly to about 0.03 mm while the relative shear displacement increases to about 0.006 mm with a positive (sinistral) shear sense, see Figure 48f). A period of stable anti-wing crack growth occurs until the bottom anti-wing crack initiates after 1115 s leading to a new abrupt increase in the relative normal displacement from 0.03 mm to 0.45 mm and an increase in the relative shear displacement from 0.006 mm to 0.012 mm. After 1181s both the anti-wing cracks propagate rapidly causing a new abrupt increase in the relative normal displacement from 0.045 mm to 0.058 mm and an increase from 0.012 to 0.014 mm in the relative shear displacement. The relative normal and shear displacements as the wing and anti-wing cracks initiate are shown in Figure 49k) and l).

5 Discussion

5.1 35-, 45- and 60-degree CZM and LEFM models

Wing crack initiation stress, angle, and location

In all the CZM and LEFM models, the wing cracks initiate at the pre-existing flaw tip. However, for the 30-degree models, the wing cracks initiate further from the flaw tip compared to the 45- and 60-degree models. This is only by one element, see Figure 32, but it is also suggested by the stress field around the pre-existing flaw tip that the high tensile stress concentrations get shifted further from the flaw tip for lower inclination angles, and get a greater extent. In other words, stress concentrations are more compact around the flaw tips for high inclination angles, which is evident when comparing the 30-, 45- and 60-degree flaw tip stress fields. This may again indicate that wing crack initiation happens closer to the flaw tip for high inclination angles. A finer mesh size around the flaw tips may help to describe these crack initiation locations to a greater detail, and it may also increase the precision of the wing crack initiation angles.

Compared to the results from experiments and the analytical solution shown in Figure 41 and Table 3, the wing crack initiation angles in the CZM and LEFM models follow the same trend in which the initiation angle decreases as the flaw inclination angle increases. However, the analytical wing crack initiation angle is 7% higher than the 30- and 45-degree models, whereas it is on average 30% higher than the 60-degree models. In Lin et al. (2019) and Wang et al. (2020) the 30- and 45-degree models have wing crack inclination angles that are on average 4% and 1% higher than the CZM and LEFM models, respectively, whereas the 60-degree wing crack initiation angles are 38% and 19% higher, respectively. The measured wing crack initiation angles from Sharafisafa and Nazem (2014) are on average 50% smaller than the angles from the CZM and LEFM models, which may be because a tapered flaw tip is used in the models, i.e., the flaw width gets smaller towards the ends. For both the CZM and the LEFM models it is the Maxps-criterion that initiates the first element splitting, thus the initial propagation direction is the same. Further, the crack propagation directions in both the CZM and LEFM models are governed by the tensile stress field, making the two models produce similar wing crack initiation angles.

The wing crack initiation stress for the CZM and LEFM models are low compared to the initiation stress observed by both Zhang et al. (2021) and Liu et al. (2021). The wing crack initiation stresses in the CZM and LEFM models are on average 77, 84 and 88% lower than the microcrack values found by Zhang et al. (2021) for the 30-, 45- and 60-degree models, respectively. In the same manner the macrocrack initiation stresses are 89, 91 and 90% lower than the macrocrack values found by Zhang et al. (2021) for the 30-, 45- and 60-degree models, respectively. This indicates that the Maxps-criterion in the CZM and LEFM models have difficulties with capturing realistic wing crack initiation stresses. Since some plastic deformation occur at the pre-existing flaw tips and reduce the stress concentrations in these areas, higher loads may be necessary to build up enough stress to initiate the wing cracks, which is not captured in the fully elastic CZM and LEFM models. However, since the CZM model can simulate such an FPZ, adjusting the damage evolution parameters may give better results. The wing crack initiation stresses captured by Liu et al. (2021) are assumed to be microcracks, and they also occur at high loads compared to the CZM and LEFM models. The CZM and LEFM values are on average 68%, 80% and 84% lower than the values found by Liu et al. (2021) for the 30-, 45- and 60-degree models, respectively. In the mentioned experimental results, the wing crack initiation stresses increase with

increasing inclination angle, which is also the case in the CZM and LEFM models, but in a lower degree.

Anti-wing crack initiation stress and location

In both the CZM and the LEFM models, the anti-wing crack initiation stresses increase with increasing inclination angle, see Figure 32. Like the wing crack initiation stresses, the difference between the two models are small, but some difference is observed in the 60-degree models, with anti-wing crack initiation stress of 165 MPa in the CZM model, and 158.5 MPa in the LEFM model. This relatively large difference may be because the wing crack in the CZM model propagates further before the anti-wing crack initiates, in this way the wing crack may create some stress release in the anti-wing crack initiation area, requiring a higher applied load to reach the Maxps-criterion. Compared to experimental results by Zhang et al. (2021) and Liu et al. (2021), the anti-wing crack initiation stress in the CZM and LEFM models have a smaller deviation compared to the wing crack initiation stresses. The anti-wing crack initiation stresses for the 30-, 45- and 60-degree CZM and LEFM models are on average 21, 19 and 16% smaller compared to Zhang et al. (2021), and 46, 39 and 4% higher compared to Liu et al. (2021), respectively. The values from Zhang et al. (2021) are the macrocrack initiation stresses, whereas the values from Liu et al. (2021) are the microcrack initiation stresses.

For both the CZM and LEFM models the anti-wing cracks initiate some distance away from the pre-existing flaw, above the bottom pre-existing flaw tip for the top anti-wing cracks, and below the top pre-existing flaw tip for the bottom anti-wing crack. This happens consequently for all inclination angles, and there are also some observations of this in Wang et al. (2020), where "white patches" are reported in the same initiation areas as for the CZM and LEFM models. These "white patches" are assumed to be a collection of microcracks and the coalescence of these, which upon further loading develops into macrocracks that initiates from the pre-existing flaw tips. From these observations it may seem that for other similar rock specimens under uniaxial loading, the micro anti-wing cracks nucleate some distance from the pre-existing flaw tips, before they develop to macrocracks which either initiate from the flaw tips, or from the stress concentration areas seen in the CZM and LEFM models. However, the initiation and propagation of the macrocracks happen very rapidly and the initiation location may be difficult to capture accurately in experiments.

Zhang et al. (2021) also observes far field Type VIII tensile cracks, seemingly initiating and propagating independently of the pre-existing flaw. However, these cracks were rarely observed in the granite specimens, and were more common in the gypsum specimens. These crack types nucleate from within the specimen, and not from any pre-existing flaw tip, which makes them similar to the anti-wing cracks observed in the CZM and LEFM models. The introduction of more crack domains in the CZM and LEFM models may make it possible to capture the initiation of the same type of far field tensile cracks using the Maxps-criterion.

Crack propagation and crack propagation length

The wing cracks propagate fully through the specimen for the 30- and 45-degree CZM models, but not for the 60-degree model, which is most likely because the model did not

converge for the last loading steps. Further, all the anti-wing cracks propagated fully through the specimen for all the CZM models. For the LEFM models, only the wing cracks in the 30-degree model propagated fully though the specimen, together with the top anti-wing crack. For the 45-degree LEFM model only the anti-wing cracks propagated fully, and none of the cracks propagated fully through the specimen in the 60-degree LEFM model. This indicates that the cracks propagate more easily in the CZM model with the input values that are used. To obtain more equivalent results in the two model types, different input values may be necessary.

In both the CZM and LEFM models the wing cracks propagate stably after they initiate, propagating progressively as load is applied. In the CZM models, the anti-wing cracks propagate rapidly after initiation for all inclination angles. The same is observed in the LEFM models, however, not all of these propagate fully through the specimen, and those to which this applies precede to propagate more stably after the rapid propagation has come to a holt. After initiation of the anti-wing cracks, the wing cracks also propagate rapidly in all the CZM models, and this is also true for the 30-degree LEFM model. In the 45- and 60-degree LEFM models it is observed that after the initiation of the anti-wing cracks, the wing cracks either stop to propagate or the propagation speed decreases somewhat before it stops completely. This may be explained by the "stress shadow" phenomena, where stress release due to initiation of new cracks suppress the propagation of existing cracks (Wong et al., 2013), and in this case the anti-wing cracks suppress the propagation of the wing cracks. As mentioned, this is not observed in any of the CZM models, which may be because of a relatively low G_{Ic}-value, leading to further propagation of the wing cracks even after they experience some suppression.

The crack propagation paths in the CZM models are observed to be smoother than the crack propagation paths in the LEFM models. In the LEFM models the crack paths are irregular compared to the CZM models, this is evident in Figure 34. Even though the same mesh is used for each inclination angle in the models, this difference in crack path is clear. Since both methods calculate propagation directions based on a stress criterion (the direction of maximum tensile stress) it is not clear why such a big difference is observed in the smoothness of the paths. However, in the CZM method it is the direction of the maximum tensile stress in the center of the element which decides the propagation direction, while in the LEFM method it is not specified where in the element the tensile stress is considered (either at the crack tip, in the center, or a combination of the two). The differences observed may indicate that the two methods do not calculate the stress in the same location, and that most likely the LEFM method calculates the tensile stress at the crack tip since it also uses VCCT which already uses displacements at the crack tip to calculate the energy release rates. It is also observed in the 30- and 45-degree LEFM models that the bottom and the top wing crack, respectively, propagates in a loop at the end of their paths, see Figure 31d) and e). This is not observed in any of the CZM models, suggesting that the propagation directions in the LEFM models are more uncertain and may more easily be affected by small stress and strain field variations. The anti-wing crack tips that are closest to the pre-existing flaw are observed to curve towards the flaw tip in the CZM models, but not in the LEFM models, and this may also be because of the possible difference in the propagation direction calculations done in CZM and LEFM.

Cracks do not always propagate fully through the specimens in Zhang et al. (2021). They often stop to grow a small distance from the top/bottom of the specimen, before complete failure occurs. In the CZM models all cracks propagate fully through the specimens (except the 60-degree model which did not completely converge). Again, a small G_{Ic}-value may be

the reason cracks propagate so "easily" in the CZM models. In the LEFM models, many of the crack stops propagating after some distance. Compared to the failed specimens in Zhang et al. (2021) the results from the LEFM models may seem more realistic than the ones achieved in the CZM models. As mentioned, in the LEFM models the propagation of the wing cracks gets suppressed after the initiation of the anti-wing cracks, which again may be explained by the "stress shadow" phenomena. Other choices of the input parameters that governs crack initiation and element degradation in the CZM models may give more realistic results regarding crack propagation lengths.

Stress concentration areas

The type IV wing cracks are common in the gypsum samples in Zhang et al. (2021), with the initiation location being shifted further towards the flaw tips as the inclination angle increases. However, for the 45-degree granite specimen in Zhang et al. (2021), one type IV wing crack is observed to initiate towards the end of the loading. This crack initiates before the anti-wing cracks have initiated and contradicts somewhat with what is observed in the CZM and LEFM models, since in these models the stress concentrations along the long sides of the pre-existing flaw do not reach any critical values before the anti-wing cracks initiate. However, it is only this type IV crack that is observed in the experiments, and unfavorable oriented microcracks or other microflaws may be the reason such a crack is able to initiate and propagate. Zhang et al. (2021) also concluded that the type IV cracks got less abundant as the inclination angle increased, which coincides with the stress concentration areas that get shifted closer and closer towards the pre-existing flaw tip as the inclination angle increases. It is important to note that the tensile stress values observed in this area after the initiation of the anti-wing cracks, get unrealistically high, see Figure 39.

The type II wing cracks that are observed in the granite specimens in Zhang et al. (2021) may be supported by the stress concentration areas that are observed to the right side of the top, and left side of the bottom wing crack. However, in the CZM and LEFM models, the stress field in this area does not reach any critical values before a significant amount of load is applied, and therefore it is the type I wing cracks that initiate in the models.

5.2 Relative displacements across the wing and anti-wing cracks

In all the models the shear displacements across the wing cracks are relatively low compared to the normal displacements at the initiation, showing how dominant the Mode I fracture mechanism is. Since the crack initiation and propagation criterions in both the CZM and LEFM models are based on maximum tensile stress (the crack initiates and propagates in the direction of the maximum tensile stress) it is expected that the relative shear displacement across the wing crack is small or negligible. However, some shearing is observed in some of the models at the time of initiation. In the 30-degree LEFM model an instant negative (dextral) shear motion happens as the wing crack initiates, while the 30- and 45-degree CZM models show slight positive (sinistral) shear motion, although these are not as instant as for the 30-degree LEFM model. The 60-degree CZM and LEFM models also show some small shear displacements just as the wing crack initiates, first negative (dextral) then positive (sinistral) almost immediately after, but the displacement values are small compared to the 30- and 45-degree models. The 45-degree LEFM model

also show very small relative shear displacements at the wing crack initiation. The small relative shear displacements at the wing crack initiation may be explained by inaccuracies in the choice of the P and P' nodes.

After the wing crack initiation, and as more load is applied to the specimen, negative (dextral) relative shear displacements are observed in all the models. The relative normal displacement for all the models increases as more load is applied, at a higher rate than the relative shear displacement. The distinct displacement jumps occur simultaneously in the normal and shear displacements as the wing crack propagates rapidly at some load increments. Generally, less relative shear displacement is observed as the flaw inclination angle increases. Since the initiation angle decreases as the inclination angle increases, the wing cracks reach the propagation direction of the applied load earlier and further opening of the wing crack may therefore not induce as much relative shear displacement. The relative shear displacement values in the CZM models are also generally larger than the values from the LEFM models.

The relative displacements as the wing cracks initiates occur seemingly in a more instant fashion in the LEFM models, and this is especially evident in the 30-degree models where the change in the relative normal displacement in the LEFM model in Figure 43b) is more instant than the change in the relative normal displacement in the CZM model in Figure 43a) as the wing crack initiates. In the 45- and 60-degree models (Figure 43c), d), e) and f)) the same tendency is observed, and it may be explained by the damage evolution used in the CZM models. Since the LEFM models do not simulate a FPZ, an element is either intact or completely split, while an element in the CZM models still have some tractions holding it together after it has been "split" (the element starts to degrade after the initial split, governed by the traction separation law). The differences in the developments of the graphs in Figure 43 may therefore show one of the differences between the two XFEM methods.

As the top anti-wing crack initiates, a closing of the top wing crack is observed in all the models, even though this closing is miniscule in the 30-degree CZM model. The higher the inclination angle, the more the top wing crack closes as the top anti-wing crack propagates. This may be because the wing cracks gets a smaller initiation angle as the inclination angle increases, i.e., they propagate more vertically when they initiate. The anti-wing crack initiates and propagates sub-vertically, making it easier to push back/close the sub-vertical wing crack. However, a closing of the top wing crack due to the propagation of the top anti-wing crack is evident in all the models, which also contributes to the positive (sinistral) relative shear displacement. In the 30- and 45-degree CZM models it is also observed that the bottom anti-wing crack initiates and propagates some distance before the top anti-wing crack initiates, causing the initial small decrease in relative shear displacement (negative shear). This is not the case in the LEFM models, as the top anti-wing crack initiates and propagates first. The opening of the wing (and anti-wing crack) as they reach the top of the specimen is also followed by a negative (dextral) shear motion.

The top anti-wing crack initiation consists of a clear increase in the relative normal displacement, and a noticeable increase in the relative shear displacement, with a positive (sinistral) shear sense in all the models, except the 45-degree LEFM model. The relative shear displacement in the 45-degree LEFM model decreases abruptly before it increases abruptly again and is held constant until the anti-wing crack reaches the top of the specimen. The bottom anti-wing crack does not propagate as much in the same time increment as the top anti-wing crack and may be a factor for the miniscule shear

displacement observed. In addition, the top wing crack stops to propagate shortly after the initiation of the top anti-wing crack in the 45-degree LEFM model.

Since multiple cracks initiate and propagate at the same times, the influence they have on each other becomes somewhat complicated to keep track of. However, XFEM in Abaqus facilitate for these types of analyses, and may make it easier compared to methods used in experiments to study displacements across cracks. Again, it’s important to note that the relative normal and shear displacement values presented in this study are approximations, and that a more exact method to measure the relative displacements across a crack in Abaqus may give different and better results.

6 Conclusion

Both the CZM and LEFM based XFEM methods in Abaqus can produce wing and anti-wing cracks successfully. After crack initiation by the Maxps-criterion, the Maxps-criterion in combination with element degradation based on fracture energy, simulate both stable and rapid crack growth in the CZM models, while the energy release rate simulates both stable and rapid crack growth in the LEFM models. The stable propagation of wing cracks in the first loading stages (non-vertical propagation direction), often followed by rapid propagation as the wing crack reaches a more vertical direction in the later loading stages, and the rapid propagation of anti-wing cracks (sub-vertical propagation direction), are in this manner successfully simulated.

The wing crack initiation stress is lower in the CZM and LEFM models compared to experimental results by Zhang et al. (2021), on an average by 90%, indicating that the Maxps-criterion initiates wing cracks prematurely on pre-existing open flaws in this elastic analysis. The anti-wing crack initiation stress in the CZM and LEFM models are closer to the initiation stresses in experiments by Zhang et al. (2021), as they are on average 19% lower. This shows that the Maxps-criterion realistically can recreate anti-wing crack initiation stresses. The increasing wing and anti-wing crack initiation stress with increasing pre-existing flaw inclination angle is also captured in both the CZM and LEFM models. Initiation of the anti-wing cracks also trigger high tensile stress concentrations to build up along the long sides of the pre-existing flaw, and these stress concentrations are oriented parallel with the flaw, and may suggest that Type IV tensile cracks can initiate. However, these cracks do not initiate because their respective crack domains are occupied by other cracks. The mentioned stress concentrations shift further towards the flaw tips as the flaw inclination angle increases.

The wing crack initiation angles are also successfully captured in the CZM and LEFM models, showing how increasing the pre-existing flaw inclination angle leads to a decrease in the wing crack initiation angle. This coincides with both the analytical solution for wing crack initiation angles and with experimental results. The initiation location of the wing cracks shifts further from the flaw tip in the 30-degree models, which is also observed in experiments. The stress concentrations around the flaw tip have a greater extent in the 30-degree models compared to the 45- and 60-degre models which are more compacted around the flaw tip itself. The anti-wing cracks initiate some distance above/below the pre-existing flaw tips in the CZM and LEFM models, which is also observed in some experiments. The initiation and propagation of the anti-wing cracks happens very rapidly, and it is also therefore difficult to observe accurately where they initiate in experiments, making it interesting to see the initiation locations simulated in the CZM and LEFM models.

In the CZM models it is the Maxps-criterion that also calculates the propagation direction correctly based on the stress and strain field in the center of the element ahead of the crack tip, while it for the LEFM models are the maximum tangential stress in the element ahead of the crack tip, but it is not clear if the stress calculations are based on the center of the element, or in the vicinity of the crack tip. The two methods of calculating the propagation direction are regardless observed to simulate overall similar propagation paths, but the propagation paths in the CZM models are smoother compared to the irregular paths simulated in the LEFM models.

Monitoring of the relative normal and shear displacements across the top wing-crack show that these are dominantly Mode I cracks, but that small shear motions occur, which is reasonable in regards to the Maxps- and MS-criteria. A clear opening of the wing cracks is observed as they initiate, typically combined with a positive (sinistral) shear motion for the

30- and 45-degree models, and with a negative (dextral) shear motion for the 60-degree models. Based on these observations it is likely that the pre-existing open flaw in some degree affects the initial shear motion across the wing cracks, and that high flaw inclination angles are less affected of the open space inside the flaw. Due to symmetry across the pre-existing flaw, it is reasonable that the same results hold for the bottom wing cracks. Since the displacement values used are approximated, it may be necessary to use a more accurate monitoring method in Abaqus to get better results, as the shear displacements are relatively small, and errors may build up easily.

The top anti-wing cracks are also observed to be dominantly Mode I cracks, but with some shear motions occurring, which also is reasonable regarding the Maxps- and MS-criteria. They typically open in a combination with a small positive (sinistral) shear motion as they initiate. The top anti-wing crack in the 45-degree LEFM model opens in combination with a small negative (dextral) shear motion, which may be explained by affects from the bottom anti-wing crack. Further, the anti-wing crack propagation causes a small closing and a positive (sinistral) shear motion in the wing cracks. The higher the inclination angle, the more the anti-wing crack propagation closes its associated wing crack.

7 Further work

7.1 General further work

Some general notions for further work:

- Comprehensive mesh size analysis with both CZM and LEFM, to capture mesh sensitivity.
- Comprehensive parameter study for G_c-values, and how different combinations of the G_c-values and the Maxps-value affect the results.
- Crack simulations in combination with Mohr-Coulomb plasticity.
- Crack simulations in specimens containing filled open flaws, e.g., filled with grout material.
- Simulations of problems regarding hydraulic jacking during injection in construction of tunnels.
- 3D simulations of crack initiation and propagation in Abaqus, using both CZM and LEFM.

7.2 Relative displacement along the 30-degree wing crack tip

It may be interesting to monitor the relative normal and shear displacements continuously along the crack tip. In this manner the displacements at the crack tip may be compared to investigate different initiation mechanisms along the crack. Some results are maintained by monitoring the relative displacements across the top 30-degree wing crack at four different locations, see Figures 50 and 51.

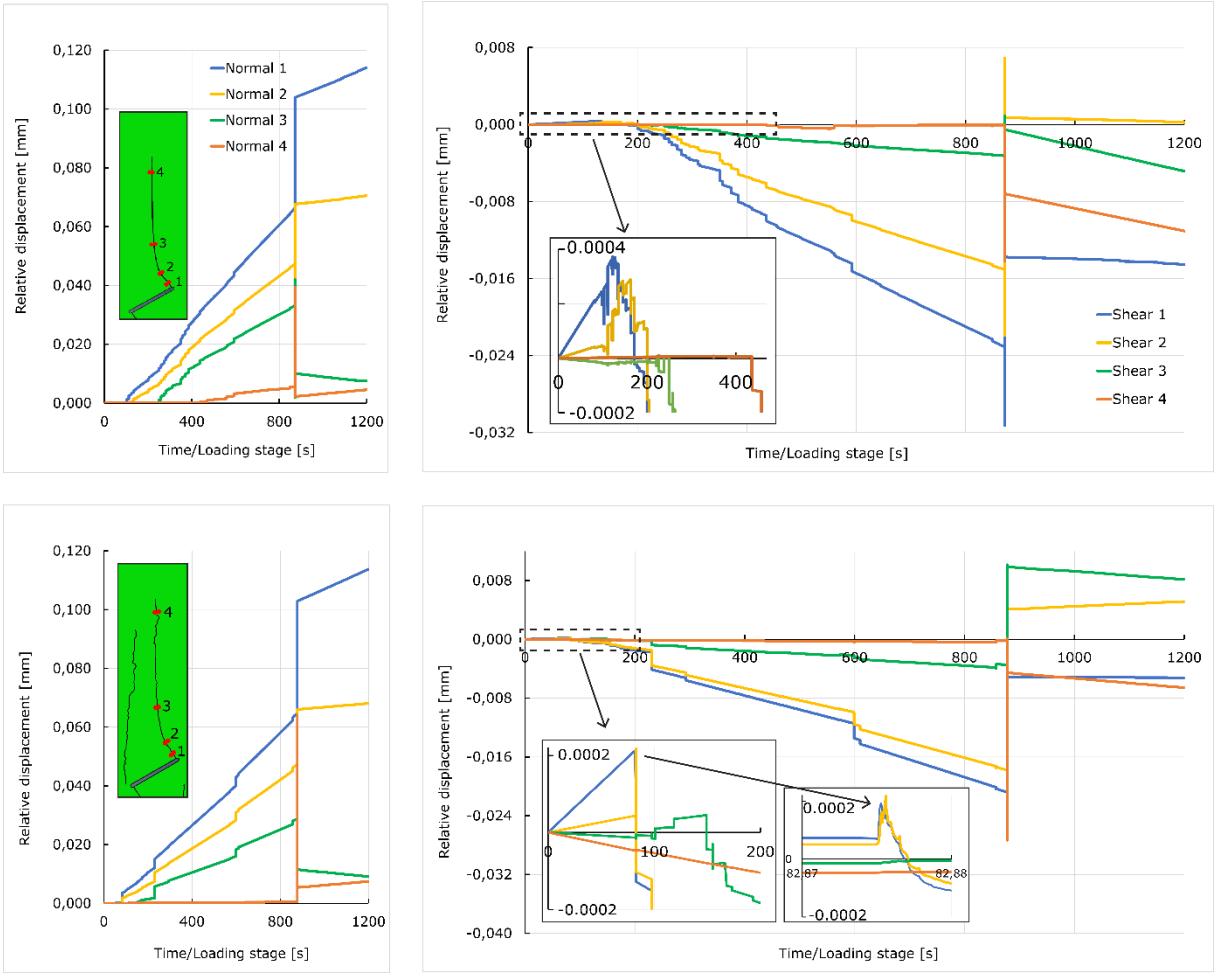

Figure 50 Relative normal and shear displacements across the top 30-degree wing crack at four different locations. Top figures are the 30-degree CZM model, bottom figures are the 30-degree LEFM model.

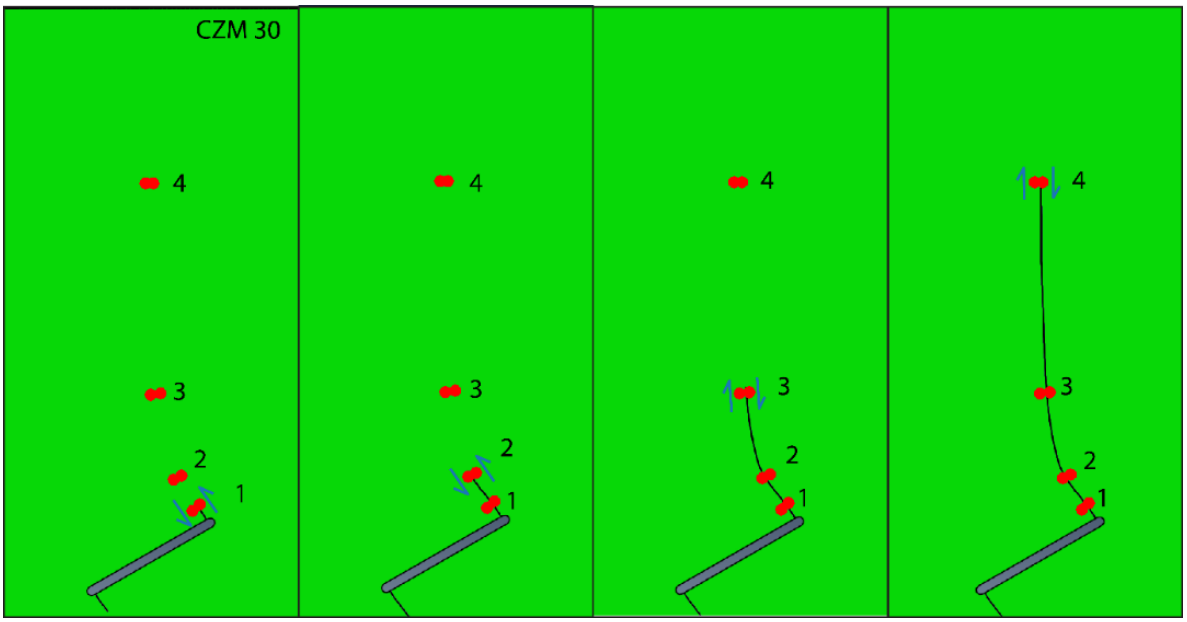

Figure 51 Relative normal and shear displacements for the 30-degree CZM model, as the top wing crack propagates through the four different node pairs.

7.3 Multiple flaws (Tripple flaw)

Simulations on specimens containing multiple flaws would be interesting. The coalescence between different cracks could in this manner solve more complicated problems than the ones analyzed in this study. In Figure 52, a specimen containing three 45-degree open flaws is used as an example and to show the possibility of simulating multiple flaws in Abaqus.

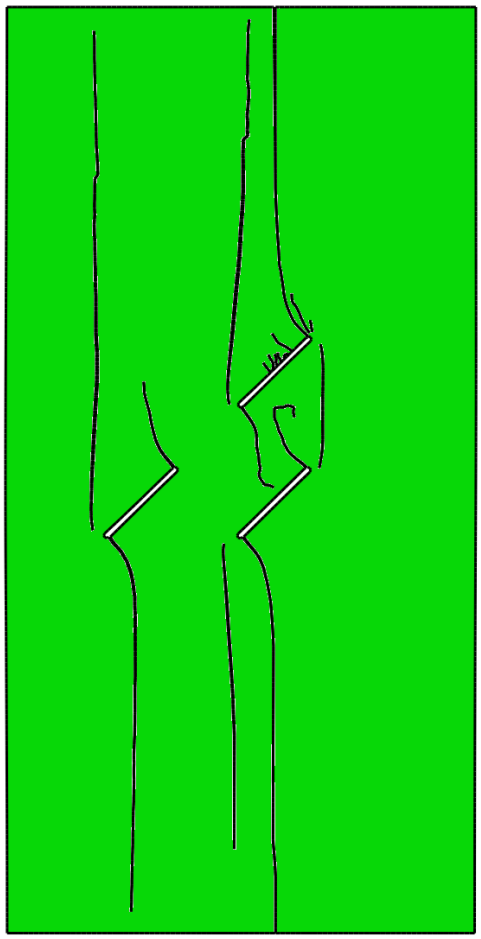

Figure 52 Specimen containing three 45-degree open flaws after uniaxial compression (vertical loading).

Bibliography

Belytschko, T. & Black, T. 1999. Elastic crack growth in finite elements with minimal remeshing. *International Journal for Numerical Methods in Engineering,* 45**,** 601-620.

Belytschko, T., Lu, Y. Y. & Gu, L. 1994. Element-free Galerkin methods. *International Journal for Numerical Methods in Engineering,* 37**,** 229-256.

Bobet, A. & Einstein, H. H. 1998. Fracture coalescence in rock-type materials under uniaxial and biaxial compression. *International Journal of Rock Mechanics and Mining Sciences,* 35**,** 863-888.

Du, Z.-Z. 2016. *eXtended Finite Element Method (XFEM) in Abaqus* [Online]. Simulia. Available: https://studylib.net/doc/13488839/extended-finite-element-method--xfem--in-abaqus-zhen-zhon... [Accessed].

Dugdale, D. S. 1960. Yielding of steel sheets containing slits. *Journal of the Mechanics and Physics of Solids,* 8**,** 100-104.

Eberhardt, E., Stead, D. & Stimpson, B. 1999. Quantifying progressive pre-peak brittle fracture damage in rock during uniaxial compression. *International Journal of Rock Mechanics and Mining Sciences,* 36**,** 361-380.

Erdogan, F. & Sih, G. C. 1963. Closure to "Discussion of 'On the Crack Extension in Plates Under Plane Loading and Transverse Shear'" (1963, ASME J. Basic Eng., 85, pp. 525–527). *Journal of Basic Engineering,* 85**,** 527-527.

Gairola, S. & Ren, J. 2021. XFEM Simulation of Tensile and Fracture Behavior of Ultrafine-Grained Al 6061 Alloy. *Metals,* 11**,** 1761.

Gjernes, J. Ø. & Klokk, E. R. 2012. *Simulering av brudd og sprekkevekst med XFEM.* Master, NTNU.

Griffith, A. A. 1920. The Phenomena of Rupture and Flow in Solids. *Philosophical Transactions,* 221**,** 163-198.

Haeri, H., Sarfarazi, V., Ebneabbasi, P., Nazari Maram, A., Shahbazian, A., Fatehi Marji, M. & Mohamadi, A. R. 2020. XFEM and experimental simulation of failure mechanism of non-persistent joints in mortar under compression. *Construction and Building Materials,* 236**,** 117500.

Hoek, E. & Martin, C. D. 2014. Fracture initiation and propagation in intact rock – A review. *Journal of Rock Mechanics and Geotechnical Engineering,* 6**,** 287-300.

Inglis, C. E. 1913. Stresses in Plates Due to the Presence of Cracks and Sharp Corners. *Transactions of the Institute of Naval Architects,* 55**,** 219-241.

Irwin, G. R. 1948. Fracture Dynamics. *American Society for Metals***,** 147-166.

Irwin, G. R. 1957. Analysis of Stresses and Strains near the End of a Crack Traversing a Plate. *Journal of Applied Mechanics,* 24**,** 361-364.

Kranz, R. L. 1979. Crack-crack and crack-pore interactions in stressed granite. *International Journal of Rock Mechanics and Mining Sciences & Geomechanics Abstracts,* 16**,** 37-47.

Krueger, R. 2002. Virtual crack closure technique: History, approach, and applications. *NASA/CR-2002-211628, ICASE Report No. 2002-10,* 57.

Kumar, S., Singh, I. V. & Mishra, B. K. 2013. Numerical Investigation of Stable Crack Growth in Ductile Materials Using XFEM. *Procedia Engineering,* 64**,** 652-660.

Lee, H. & Jeon, S. 2011. An experimental and numerical study of fracture coalescence in pre-cracked specimens under uniaxial compression. *International Journal of Solids and Structures,* 48**,** 979-999.

Lei, Q., Latham, J.-P., Xiang, J. & Tsang, C.-F. 2017. Role of natural fractures in damage evolution around tunnel excavation in fractured rocks. *Engineering Geology,* 231.

Lin, H., Yang, H., Wang, Y., Zhao, Y. & Cao, R. 2019. Determination of the stress field and crack initiation angle of an open flaw tip under uniaxial compression. *Theoretical and Applied Fracture Mechanics,* 104**,** 102358.

Lisjak, A., Figi, D. & Grasselli, G. 2014. Fracture development around deep underground excavations: Insights from FDEM modelling. *Journal of Rock Mechanics and Geotechnical Engineering,* 6**,** 493-505.

Liu, L., Li, H., Li, X., Wu, D. & Zhang, G. 2021. Underlying Mechanisms of Crack Initiation for Granitic Rocks Containing a Single Pre-existing Flaw: Insights From Digital Image Correlation (DIC) Analysis. *Rock Mechanics and Rock Engineering,* 54**,** 857-873.

Mahabadi, O. K., Lisjak, A., Munjiza, A. & Grasselli, G. 2012. Y-Geo: New Combined Finite-Discrete Element Numerical Code for Geomechanical Applications. *International Journal of Geomechanics,* 12**,** 676-688.

Melenk, J. M. & Babuška, I. 1996. The partition of unity finite element method: Basic theory and applications. *Computer Methods in Applied Mechanics and Engineering,* 139**,** 289-314.

Moës, N., Dolbow, J. & Belytschko, T. 1999. A finite element method for crack growth without remeshing. *International Journal for Numerical Methods in Engineering,* 46**,** 131-150.

Orowan, E. 1948. Fracture and Strength of Solids. *Reports on Progress in Physics,* 12**,** 185.

Osher, S. & Sethian, J. A. 1988. Fronts propagating with curvature-dependent speed: Algorithms based on Hamilton-Jacobi formulations. *Journal of Computational Physics,* 79**,** 12-49.

Reyes, O. & Einstein, H. H. 1991. Failure mechanisms of fractured rock - A fracture coalescence model.

Sharafisafa, M. & Nazem, M. 2014. Application of the distinct element method and the extended finite element method in modelling cracks and coalescence in brittle materials. *Computational Materials Science,* 91**,** 102-121.

Sivakumar, G. & Maji, V. B. 2021. Crack Growth in Rocks with Preexisting Narrow Flaws under Uniaxial Compression. *International Journal of Geomechanics,* 21**,** 04021032.

Stolarska, M., Chopp, D., Moes, N. & Belytschko, T. 2001. Modelling crack growth by level sets in extended finite element method. *International Journal for Numerical Methods in Engineering,* 51**,** 943-960.

Sun, C. T. & Jin, Z. H. 2012a. Chapter 1 - Introduction. *In:* SUN, C. T. & JIN, Z. H. (eds.) *Fracture Mechanics.* Boston: Academic Press.

Sun, C. T. & Jin, Z. H. 2012b. Chapter 2 - Griffith Theory of Fracture. *In:* SUN, C. T. & JIN, Z. H. (eds.) *Fracture Mechanics.* Boston: Academic Press.

Sun, C. T. & Jin, Z. H. 2012c. Chapter 3 - The Elastic Stress Field around a Crack Tip. *In:* SUN, C. T. & JIN, Z. H. (eds.) *Fracture Mechanics.* Boston: Academic Press.

Sun, C. T. & Jin, Z. H. 2012d. Chapter 4 - Energy Release Rate. *In:* SUN, C. T. & JIN, Z. H. (eds.) *Fracture Mechanics.* Boston: Academic Press.

Sun, C. T. & Jin, Z. H. 2012e. Chapter 5 - Mixed Mode Fracture. *In:* SUN, C. T. & JIN, Z. H. (eds.) *Fracture Mechanics.* Boston: Academic Press.

Systèmes, D. 2009. *Abaqus: Modeling discontinuities as an enriched feature using the extended finite element method* [Online]. Available: https://abaqus-docs.mit.edu/2017/English/SIMACAEANLRefMap/simaanl-c-enrichment.htm#simaanl-c-enrichment-lefm [Accessed].

Vásárhelyi, B. & Bobet, A. 2000. Modeling of Crack Initiation, Propagation and Coalescence in Uniaxial Compression. *Rock Mechanics and Rock Engineering,* 33**,** 119-139.

Wang, H. 2015. Numerical modeling of non-planar hydraulic fracture propagation in brittle and ductile rocks using XFEM with cohesive zone method. *Journal of Petroleum Science and Engineering,* 135**,** 127-140.

Wang, Y., Zhang, H., Lin, H., Zhao, Y. & Liu, Y. 2020. Fracture behaviour of central-flawed rock plate under uniaxial compression. *Theoretical and Applied Fracture Mechanics,* 106**,** 102503.

Westergaard, H. M. 1939. Bearing Pressures and Cracks. *Journal of Applied Mechanics,* 6**,** A49-53.

Wong, L. N. Y. & Einstein, H. H. 2009. Systematic evaluation of cracking behavior in specimens containing single flaws under uniaxial compression. *International Journal of Rock Mechanics and Mining Sciences,* 46**,** 239-249.

Wong, S.-W., Geilikman, M. & Xu, G. Interaction of Multiple Hydraulic Fractures in Horizontal Wells. SPE Unconventional Gas Conference and Exhibition, 2013/01/28/ 2013. OnePetro.

Wu, Z. & Wong, L. N. Y. 2012. Frictional crack initiation and propagation analysis using the numerical manifold method. *Computers and Geotechnics,* 39**,** 38-53.

Xie, Y., Cao, P., Liu, J. & Dong, L. 2016. Influence of crack surface friction on crack initiation and propagation: A numerical investigation based on extended finite element method. *Computers and Geotechnics,* 74**,** 1-14.

Xu, Y. & Yuan, H. 2011. Applications of normal stress dominated cohesive zone models for mixed-mode crack simulation based on extended finite element methods. *Engineering Fracture Mechanics,* 78**,** 544-558.

Yang, S.-Q., Liu, X.-R. & Jing, H.-W. 2013. Experimental investigation on fracture coalescence behavior of red sandstone containing two unparallel fissures under uniaxial compression. *International Journal of Rock Mechanics and Mining Sciences,* 63**,** 82-92.

Zhang, G., Wang, M., Li, X., Yue, S., Wen, Z. & Han, S. 2021. Micro- and macrocracking behaviors in granite and molded gypsum containing a single flaw. *Construction and Building Materials,* 292**,** 123452.

Zhou, X.-P., Zhang, J.-Z., Qian, Q.-H. & Niu, Y. 2019. Experimental investigation of progressive cracking processes in granite under uniaxial loading using digital imaging and AE techniques. *Journal of Structural Geology,* 126**,** 129-145.

Appendix

The stress-strain curves for the CZM and LEFM models are presented here, i.e., Figures 30, 35, 36, 37 and 38.

The following CAE-files and INP/ODB-files are used in this study, and they are available in the Zip-folder:

- GRANITE SINGLE FLAW 30: *CZM20and001and01* and *LEFM20and001and01*

- Granite single flaw 45 maxps 10: *CZM20and001and1-finemeshcorner* and *LEFM20and001and1-finecornerunstab*

- GRANITE SINGLE FLAW 60: *CZM20and001and01* and *LEFM20and001and1*

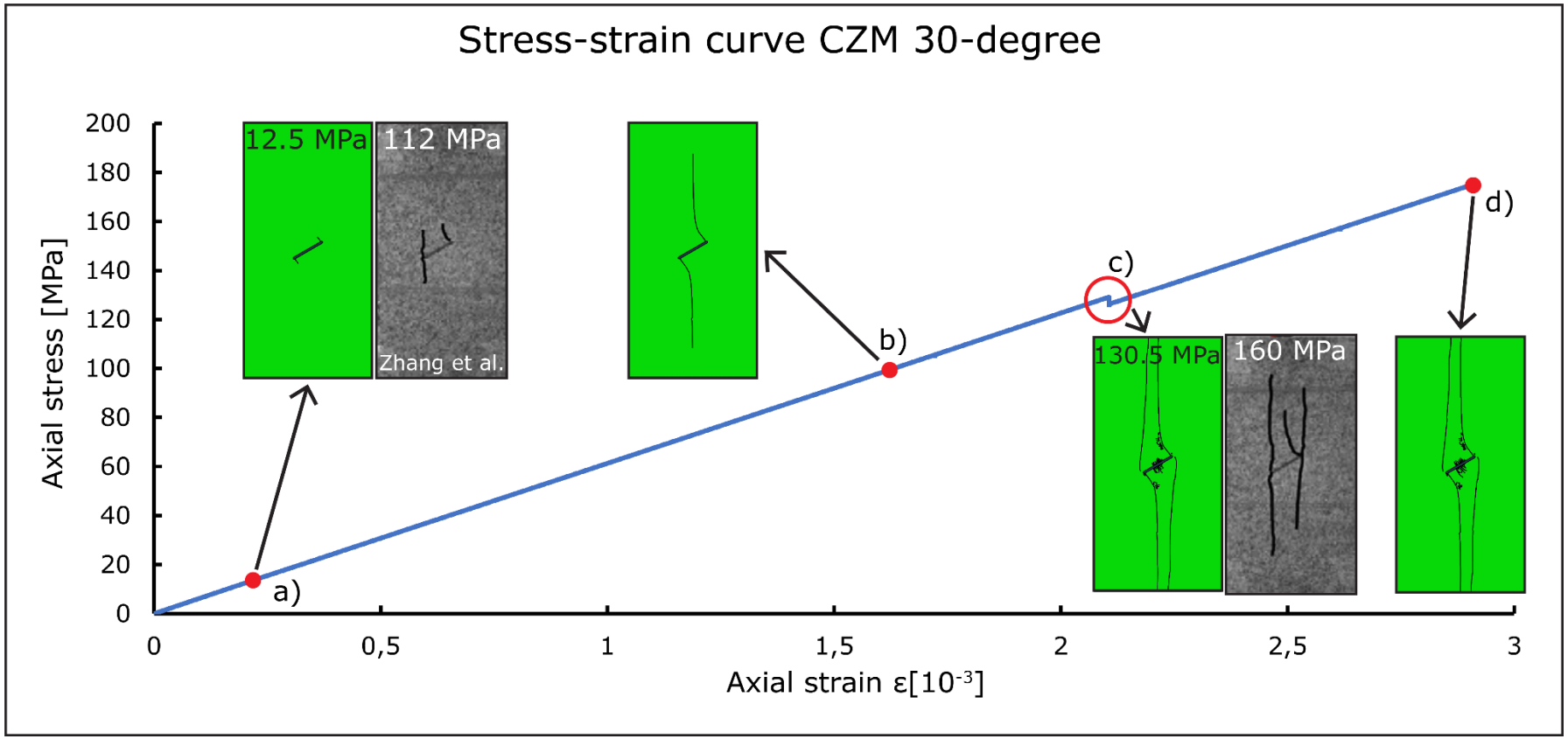
Stress-strain curve CZM 30-degree
Axial stress [MPa]
200
180
160
140
120
100
80
60
40
20
0
0
0,5
1
1,5
2
2,5
3
Axial strain ε[10-3]
12.5 MPa
112 MPa
Zhang et al.
130.5 MPa
160 MPa
a)
b)
c)
d)

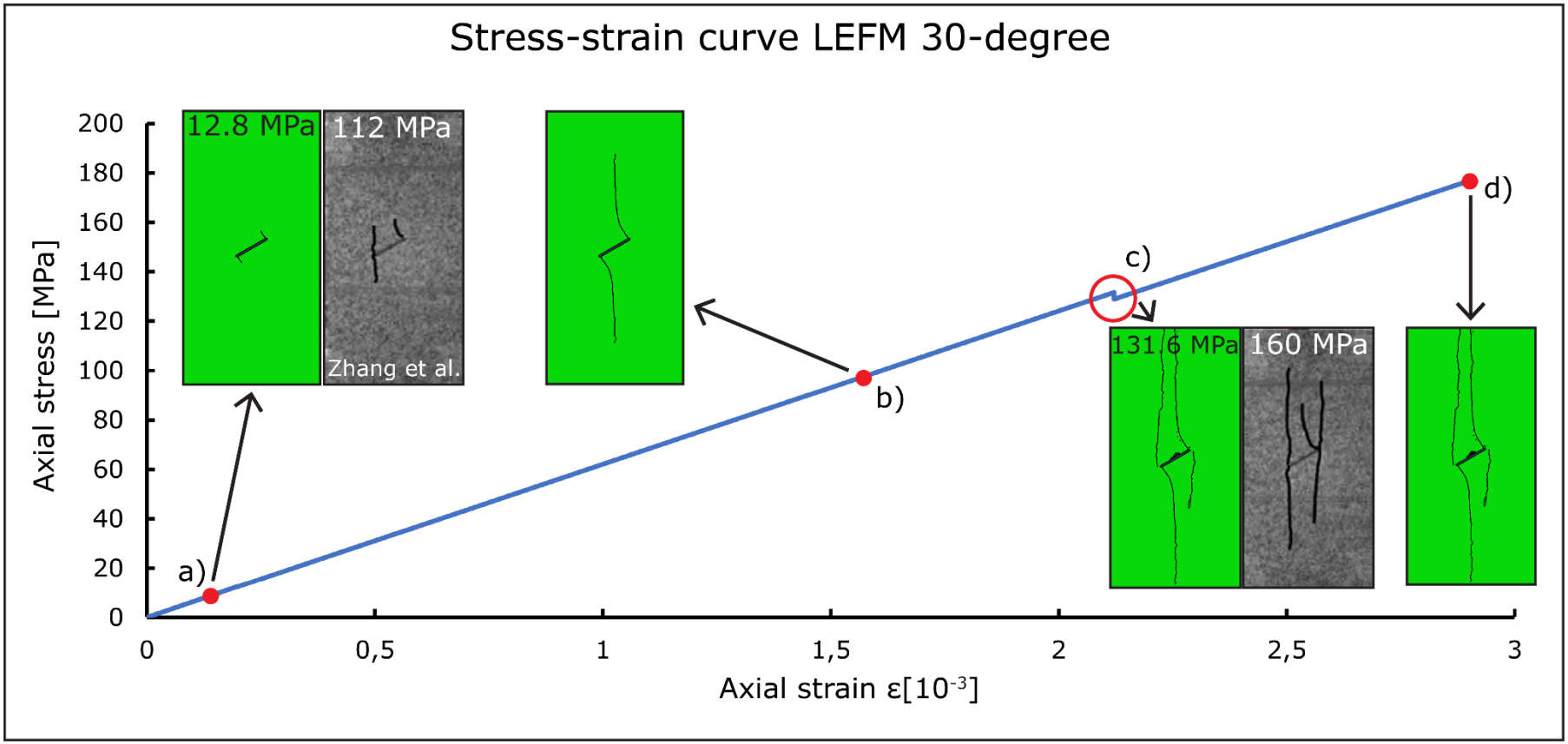
Stress-strain curve LEFM 30-degree
Axial stress [MPa]
200
180
160
140
120
100
80
60
40
20
0
0
0,5
1
1,5
2
2,5
3
Axial strain ε[10-3]
12.8 MPa
112 MPa
Zhang et al.
131.6 MPa
160 MPa
a)
b)
c)
d)

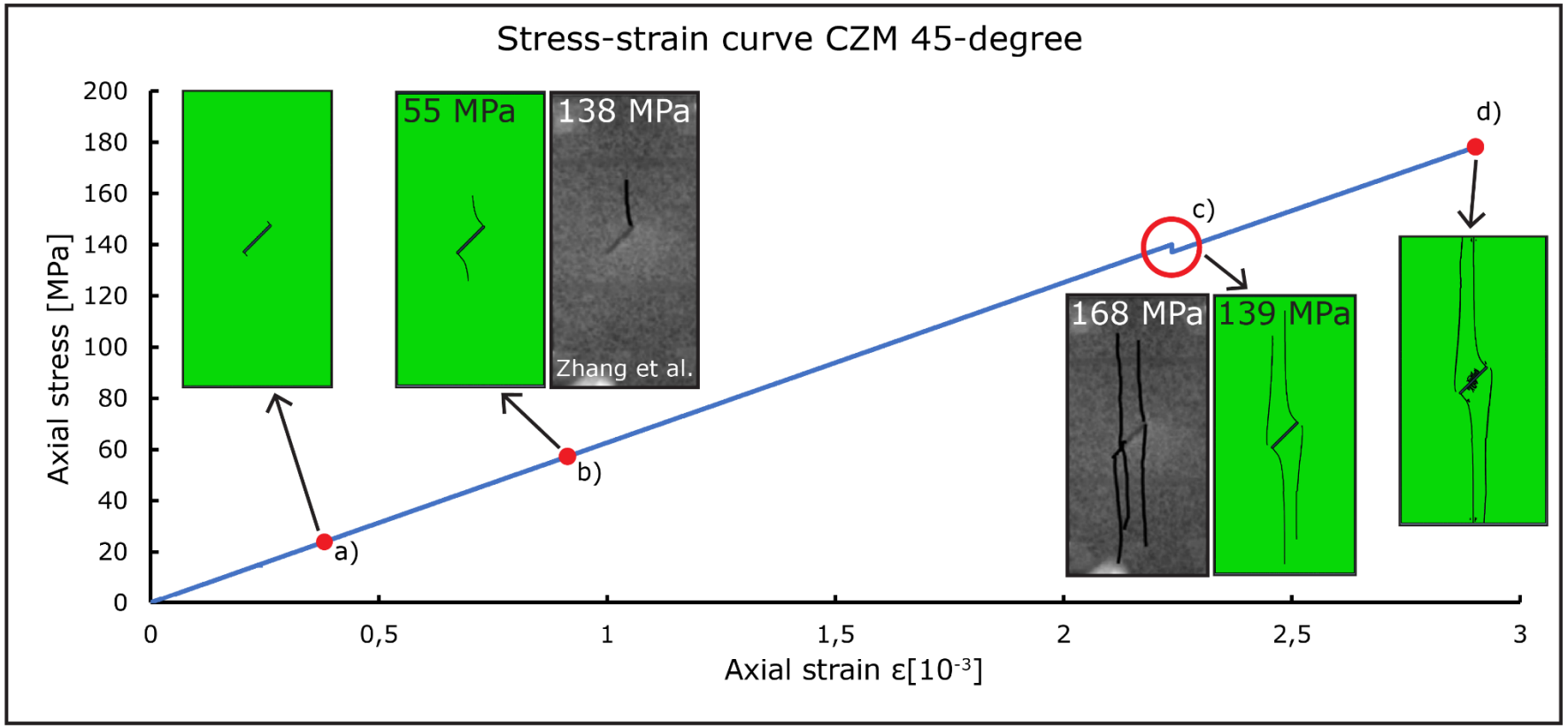
Stress-strain curve CZM 45-degree
Axial stress [MPa]
200
180
160
140
120
100
80
60
40
20
0
0
0,5
1
1,5
2
2,5
3
Axial strain ε[10-3]
55 MPa
138 MPa
Zhang et al.
168 MPa
139 MPa
a)
b)
c)
d)

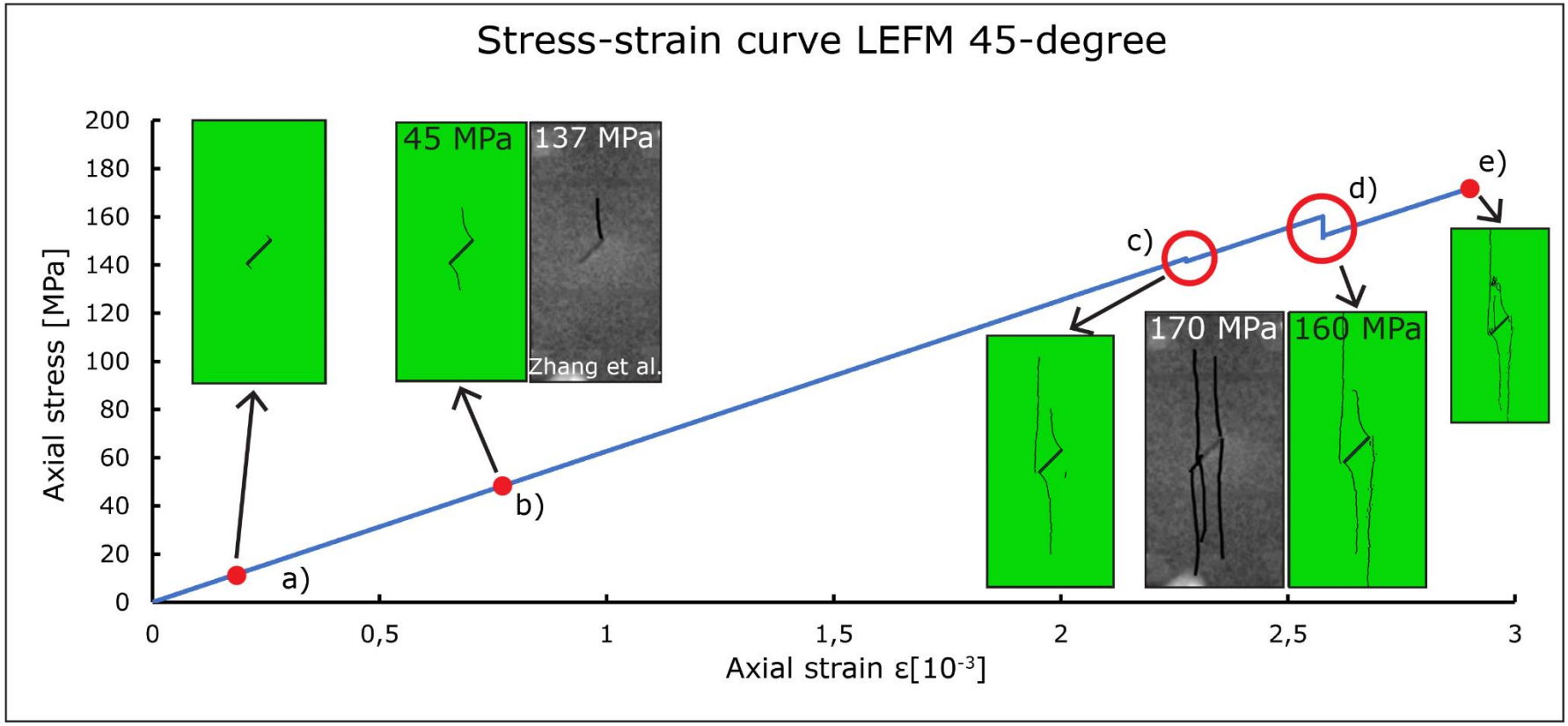
Stress-strain curve LEFM 45-degree
Axial stress [MPa]
200
180
160
140
120
100
80
60
40
20
0
0
0,5
1
1,5
2
2,5
3
Axial strain ε[10-3]
45 MPa
137 MPa
Zhang et al.
170 MPa
160 MPa
a)
b)
c)
d)
e)

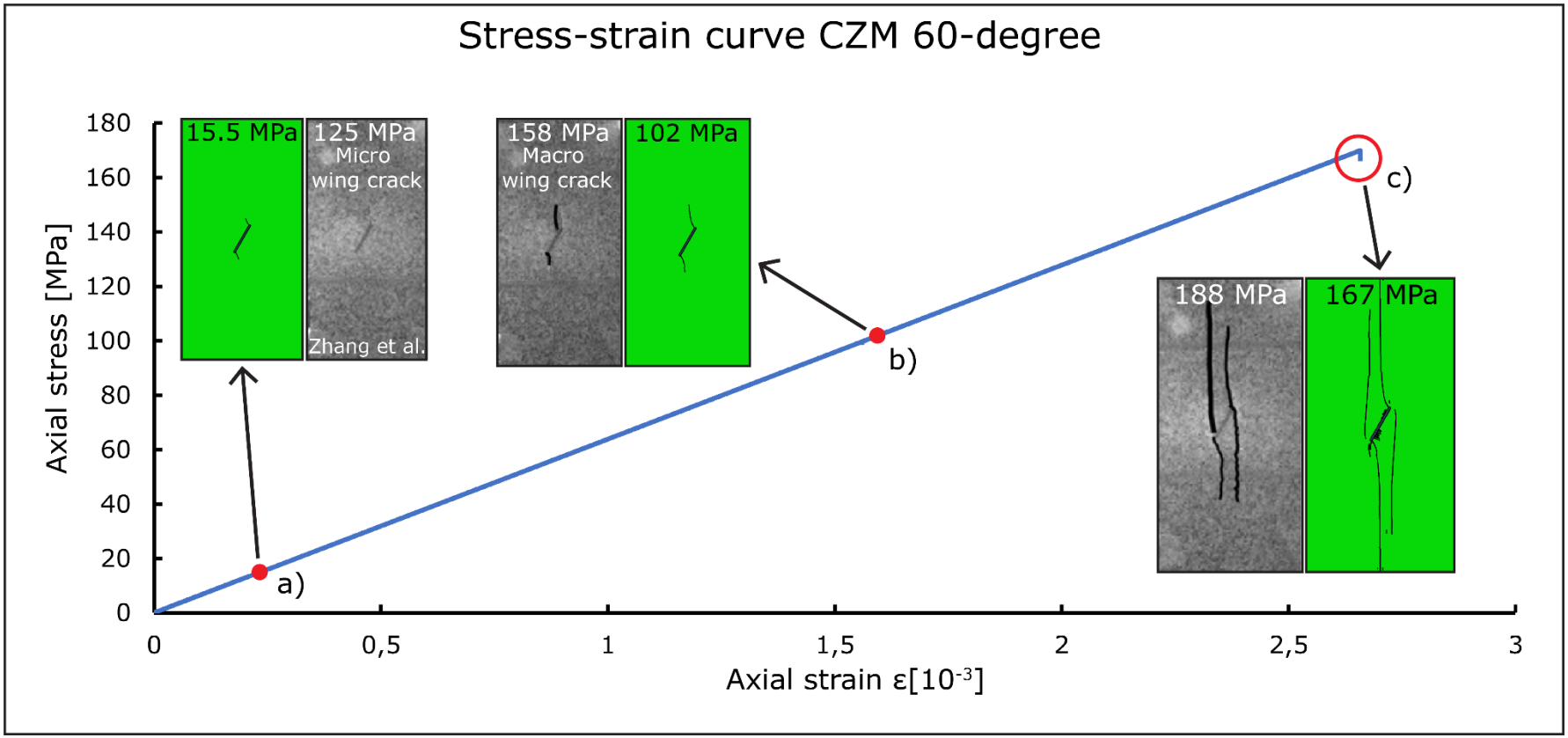
Stress-strain curve CZM 60-degree
Axial stress [MPa]
Axial strain ε[10-3]
0
20
40
60
80
100
120
140
160
180
0
0,5
1
1,5
2
2,5
3
15.5 MPa
125 MPa
Micro
wing crack
Zhang et al.
158 MPa
Macro
wing crack
102 MPa
188 MPa
167 MPa
a)
b)
c)

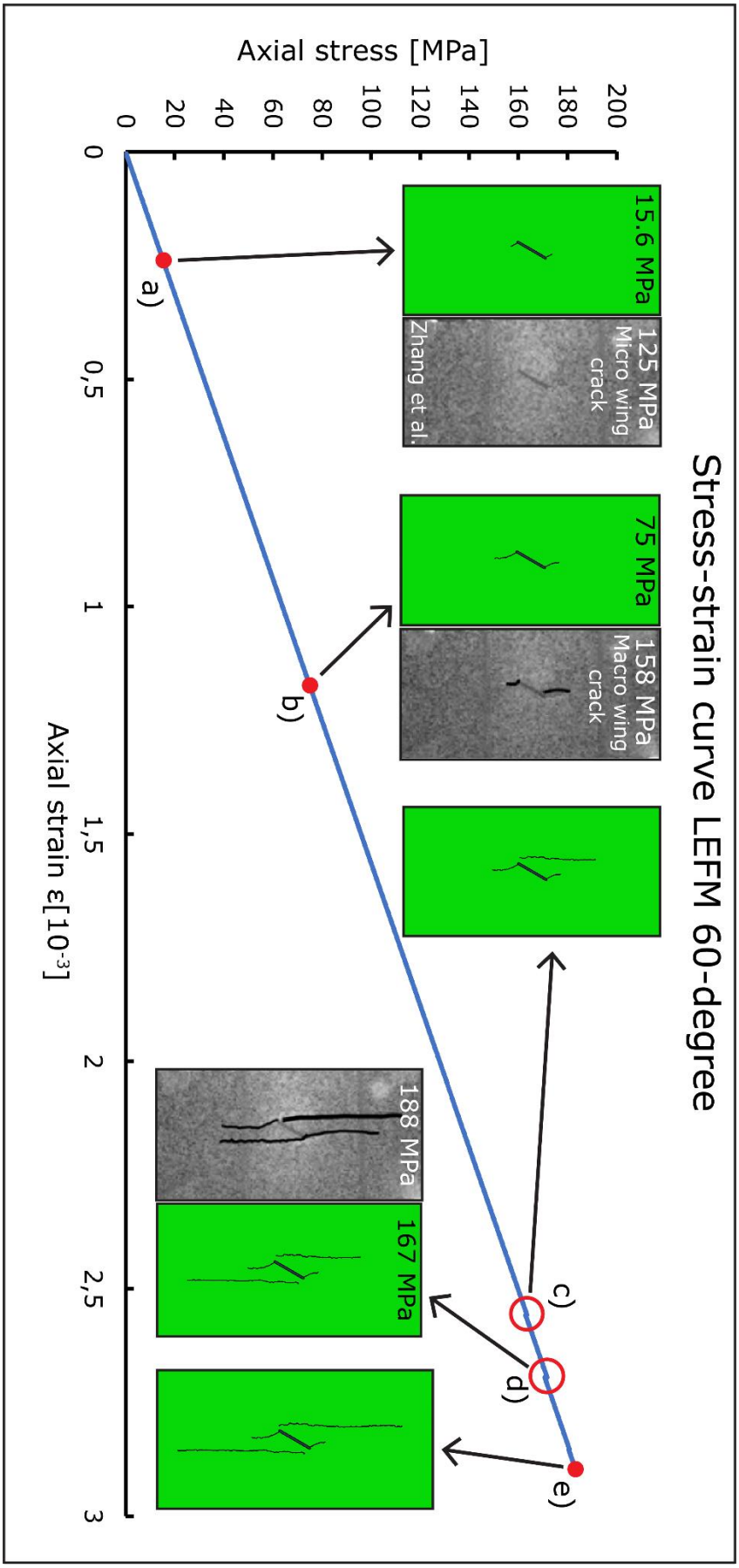
Stress-strain curve LEFM 60-degree
Axial stress [MPa]
0
20
40
60
80
100
120
140
160
180
200
Axial strain ε[10-3]
0
0,5
1
1,5
2
2,5
3
a)
b)
c)
d)
e)
15.6 MPa
125 MPa
Micro wing crack
Zhang et al.
75 MPa
158 MPa
Macro wing crack
188 MPa
167 MPa

Kristoffer Aurstad Dolvik

Numerical modelling of crack initiation and propagation in rocks using the XFEM

NTNU
Norwegian University of
Science and Technology